Summer 2010

Regional lung function and mechanics using image registration

Kai Ding
University of Iowa

REGIONAL LUNG FUNCTION AND MECHANICS

USING IMAGE REGISTRATION

by

Kai Ding

An Abstract

Of a thesis submitted in partial fulfillment of the
requirements for the Doctor of Philosophy
degree in Biomedical Engineering
in the Graduate College of
The University of Iowa

July 2010

Thesis Supervisor: Professor Joseph M. Reinhardt

ABSTRACT

The main function of the respiratory system is gas exchange. Since many disease or injury conditions can cause biomechanical or material property changes that can alter lung function, there is a great interest in measuring regional lung function and mechanics.

In this thesis, we present a technique that uses multiple respiratory-gated CT images of the lung acquired at different levels of inflation with both breath-hold static scans and retrospectively reconstructed 4D dynamic scans, along with non-rigid 3D image registration, to make local estimates of lung tissue function and mechanics. We validate our technique using anatomical landmarks and functional Xe-CT estimated specific ventilation.

The major contributions of this thesis include: 1) developing the registration derived regional expansion estimation approach in breath-hold static scans and dynamic 4DCT scans, 2) developing a method to quantify lobar sliding from image registration derived displacement field, 3) developing a method for measurement of radiation-induced pulmonary function change following a course of radiation therapy, 4) developing and validating different ventilation measures in 4DCT.

The ability of our technique to estimate regional lung mechanics and function as a surrogate of the Xe-CT ventilation imaging for the entire lung from quickly and easily obtained respiratory-gated images, is a significant contribution to functional lung imaging because of the potential increase in resolution, and large reductions in

imaging time, radiation, and contrast agent exposure. Our technique may be useful to detect and follow the progression of lung disease such as COPD, may be useful as a planning tool during RT planning, may be useful for tracking the progression of toxicity to nearby normal tissue during RT, and can be used to evaluate the effectiveness of a treatment post-therapy.

Abstract Approved: _____
Thesis Supervisor

_____
Title and Department

_____
Date

REGIONAL LUNG FUNCTION AND MECHANICS

USING IMAGE REGISTRATION

by

Kai Ding

A thesis submitted in partial fulfillment of the
requirements for the Doctor of Philosophy
degree in Biomedical Engineering
in the Graduate College of
The University of Iowa

July 2010

Thesis Supervisor: Professor Joseph M. Reinhardt

Graduate College
The University of Iowa
Iowa City, Iowa

CERTIFICATE OF APPROVAL

PH.D. THESIS

This is to certify that the Ph.D. thesis of

Kai Ding

has been approved by the Examining Committee for the thesis requirement for the Doctor of Philosophy degree in Biomedical Engineering at the July 2010 graduation.

Thesis Committee: _____
Joseph M. Reinhardt, Thesis Supervisor

_____
Gary E. Christensen

_____
Madhavan L. Raghavan

_____
Eric A. Hoffman

_____
John E. Bayouth

ACKNOWLEDGEMENTS

First of all, I would like to thank my advisor, Dr. Joseph Reinhardt for his patient guidance and support throughout my study. I am greatly indebted to him for his inspiring and encouraging words and his wealth of brilliant ideas during the research.

I appreciate Dr. John Bayouth, who inspired me to develop interest in the medical physics field, owing to his experience and expertise. I am grateful to Dr. Gary E. Christensen and his student Kunlin Cao and Joo Hyun Song for help on image registration. Without discussing and consulting with Kunlin Cao, the work could not have proceeded so efficiently. I would like to thank Dr. Eric Hoffman and his students Matthew Fuld and Youbing Yin for their support and advice in CT imaging and data analysis, and assistance in animal experiments. I have also enjoyed working with Dr. Madhavan Raghavan and his student Ryan Amelon and I would like to thank them for the valuable discussions. My special thanks go to Dr. Bram van Ginneken and Keelin Murphy for providing the software iX. Thanks to Shalmali Bodas, Matthew Moehlmann and Divya Maxwell for their assistance in landmark analysis. Thanks to my labmates Sangyeol Lee, Lijun Shi, Sudarshan Bommu, Panfang Hua, Xiayu Xu, Kaifang Du, Tarunashree Yavarna and Vinayak Joshi for being helpful and fun, and the medical physics residents for their advice with the clinical practice, including Xiaofei Yin, Yunfei Huang and Junyi Xia. I have been benefited from the interactions with many workmates in other departments including Qi Song, Xin Dou, Yunlong Liu,

Yin Yin, Mingqing Chen and Weichen Gao. In addition, I would like to thank Dr. Milan Sonka and Dr. Brett Simon for their valuable suggestions for my research.

This work was supported in part by grants HL079406, HL064368 and EB004126 from the National Institutes of Health.

Finally, last but not least, I would like to extend a special thanks to my parents, Zhihong Ding and Suping Wang, for their love and support throughout this process.

The contributions of all these people are greatly appreciated.

ABSTRACT

The main function of the respiratory system is gas exchange. Since many disease or injury conditions can cause biomechanical or material property changes that can alter lung function, there is a great interest in measuring regional lung function and mechanics.

In this thesis, we present a technique that uses multiple respiratory-gated CT images of the lung acquired at different levels of inflation with both breath-hold static scans and retrospectively reconstructed 4D dynamic scans, along with non-rigid 3D image registration, to make local estimates of lung tissue function and mechanics. We validate our technique using anatomical landmarks and functional Xe-CT estimated specific ventilation.

The major contributions of this thesis include: 1) developing the registration derived regional expansion estimation approach in breath-hold static scans and dynamic 4DCT scans, 2) developing a method to quantify lobar sliding from image registration derived displacement field, 3) developing a method for measurement of radiation-induced pulmonary function change following a course of radiation therapy, 4) developing and validating different ventilation measures in 4DCT.

The ability of our technique to estimate regional lung mechanics and function as a surrogate of the Xe-CT ventilation imaging for the entire lung from quickly and easily obtained respiratory-gated images, is a significant contribution to functional lung imaging because of the potential increase in resolution, and large reductions in

imaging time, radiation, and contrast agent exposure. Our technique may be useful to detect and follow the progression of lung disease such as COPD, may be useful as a planning tool during RT planning, may be useful for tracking the progression of toxicity to nearby normal tissue during RT, and can be used to evaluate the effectiveness of a treatment post-therapy.

TABLE OF CONTENTS

LIST OF TABLES

Table

LIST OF FIGURES

Figure

CHAPTER 1
INTRODUCTION

1.1 Respiratory Physiology and Mechanics

Air is alternately inspired and expired as lungs expand and contract during the respiratory cycle. There are two lungs in human, the right and left, each divided into lobes. The lungs, like the heart, are situated in the thorax, the closed compartment bounded at the neck by muscles and connective tissue and completely separated from the abdomen by a large, dome-shaped sheet of skeletal muscle, the diaphragm. Each lung is surrounded by a completely closed sac, the pleural sac. The two lungs are not symmetrical. The right lung has three lobes, and the slightly smaller left lung has only two. In the right lung, the upper lobe and the middle lobe are separated by the horizontal fissure. Inferiorly, an oblique fissure separates the middle lobe and the lower lobe. In the left lung, the fissure that separates the upper lobe and lower lobe is also called oblique fissure.

Figure 1.1 provides a overview of the respiratory system. As illustrated in Figure 1.1, the trachea branches into two bronchi, one of which enters each lung. Within the lungs, there are more than 20 generations of airway branching, each resulting in narrower, shorter, and more numerous tubes. Each lung is surrounded by a closed sac, the pleural sac, consisting of a thin sheet of cells called pleura. The relationship between a lung and its pleural sac can be visualized by imagining what happens when you push a fist into a fluid-filled balloon. The fist becomes coated by

one surface of the balloon. The opposite surfaces lie close together but are separated by a thin layer of fluid. Unlike the balloons and fist, however, the plural surface coating the lung (visceral pleural) is firmly attached to the lung by connective tissue. Similarly, the outer layer (the parietal pleura) is attached to and lines the interior thoracic wall and diaphragm. The two layers are separated by an extremely thin layer of intrapleural fluid. The pressure of of the intrapleural fluid is called intrapleural pressure (P_{ip}). The changes of the intrapleural pressure cause the lungs and thoracic wall to move in and out together during normal breathing. The intrapleural pressure is the pressure outside the lungs and the pressure inside the lungs is the alveolar pressure (P_{alv}). The difference in pressure between the inside and the outside of the lungs is termed the transpulmonary pressure (P_{tp}), where $P_{tp} = P_{alv} - P_{ip}$. The transpulmonary pressure is a determinant of lung size. The trans-respiratory system pressure, difference between the alveolar pressure and the atmospheric pressure ($P_{rs} = P_{alv} - P_{atm}$), is a determinant of air flow. The intrapleural pressure at rest is a balance between the tendency of the lung to collapse and the tendency of the chest wall to expand. As the diaphragm and the intercostal muscles contract, the thorax expands. The P_{ip} becomes more subatmospheric/negative (consider atmospheric pressure P_{atm} be the zero reference point), the transitionary pressure becomes more positive causing the lungs expand. The enlargement of the lungs causes an increase in the sizes of the alveoli through out the lungs. Therefore, by Boyle's law, the P_{alv} decreases to less than atmospheric. This produces the difference in pressure ($P_{alv} < P_{atm}$) that causes the a bulk flow of air from the atmosphere through the airways into the alveoli. As the

diaphragm and inspiratory intercostal muscles stop contracting. The chest wall recoils inward causing the P_{ip} moves back toward preinspiration value. The transpulmonary pressure also moves back toward preinspiration value. Therefore, the transpulmonary pressure acting to expand the lungs is now smaller and the lungs passively recoild to their original size. As the lungs become smaller, air in the alveoli becomes temporarily compressed so that, by Boyle's law, alveolar pressure exceeds atmospheric pressure. Therefore, air flows from the alveoli through the airways out into the atmosphere.

The lung tissue consists of bronchioles, bronchi, blood vessels, interstitium and alveoli. The lung tissue expands as air rich in oxygen flow into the lungs through conducting airways. The air then reaches the transitional zone consisting of respiratory bronchioles and the respiratory zone composed of alveoli. The pulmonary capillaries with venous blood form a fine mesh network around each alveolus. Oxygen in the air is exchanged for the carbon dioxide in the venous blood pumped from the pulmonary arteries. The blood rich in oxygen leaves the lungs via pulmonary veins. It is then distributed throughout the body to fulfill the needs of continuous supply of oxygen to trillions of cells in the body. On the other hand, the exchanged gas, rich in carbon dioxide, is then expelled as the contraction of the lung tissue during the expiration. Figure 1.2 provides resin casts of the airways and blood vessels. The Figure 1.2(a) shows the airway of the lungs on the left-hand side and the airways with the pulmonary arteries and veins on the right-hand side. Figure 1.2(b) shows a close-up version of the casts. The arteries follow the airway to the periphery and the veins are lying between the alveoli.

The thoracic cavity can be thought as an container. Enlarging the size of the container by the diaphragm and intercostal muscles increases its volume and thus decreases the pressure within it. This decrease in internal gas pressure in turn causes air to enter the container from the atmosphere through the nose and/or mouth. As the inspiratory muscles relax, the rib cage drops under the force of gravity and the relaxing diaphragm moves superiorly. The result is that the volumes of the thorax and lungs decrease simultaneously, which increases the pressure within the lungs and pushes the air out. Figure 1.3 provides a simplified physical model of the respiratory system, where the airtight glass dome sealed with a flexible membrane simulates the thorax and the two balloons simulates the lungs. The pressure between the balloons and the glass dome in Figure 1.3 causes the balloon inflate and deflate. Figure 1.3(a) shows as the membrane pulled down, the balloons inflate because of the increased thorax volume. Figure 1.3(b) shows as the membrane relaxes, the balloons deflate because of the decreased thorax volume.

Lung tissue function depends upon the material and mechanical properties of the lung parenchyma and the relationships between the lungs, diaphragm, and other parts of the respiratory system. Pulmonary diseases can change the tissue material and mechanical properties of lung parenchyma. Pulmonary emphysema, a chronic obstructive pulmonary disease (COPD), is characterized by loss of elasticity (increased compliance) of the lung tissue, from destruction of structures supporting the alveoli and destruction of capillaries feeding the alveoli [12], as shown in Figure 1.4. Idiopathic pulmonary fibrosis (IPF), a classic interstitial lung disease, causes

inflammation and fibrosis of tissue in the lungs. Over time, the disease makes the tissue thicker and stiffer (reduced compliance). As the change of the material properties and the disease process itself are associated with the mechanical changes, it would be desirable to have objective methods to determine the regional mechanics which reflect regional pulmonary function.

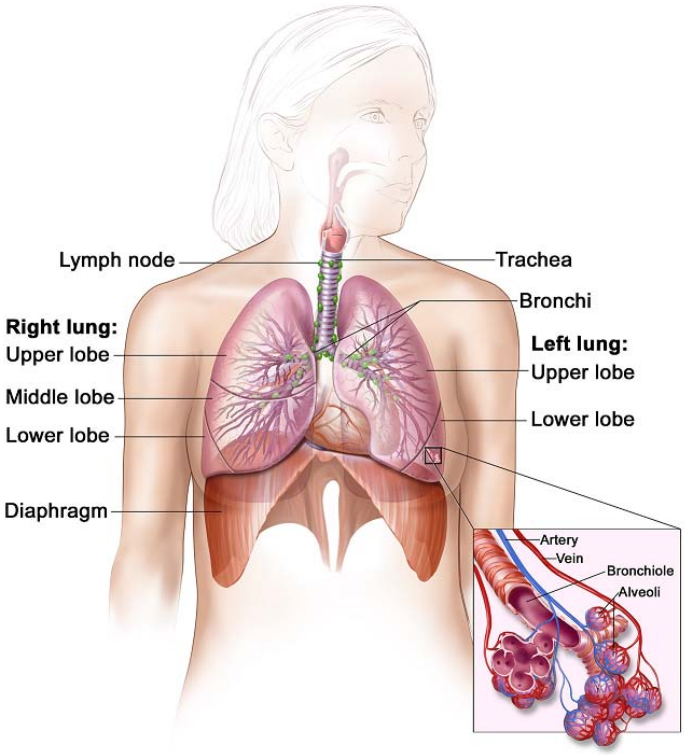

Figure 1.1: Organization of the respiratory system from [1].

1.2 Current Approaches for Measuring Lung Function

Various efforts have been made to assess lung function. Invasive methods, such as percutaneously or surgically implanted parenchymal markers or inhaled fluorescent

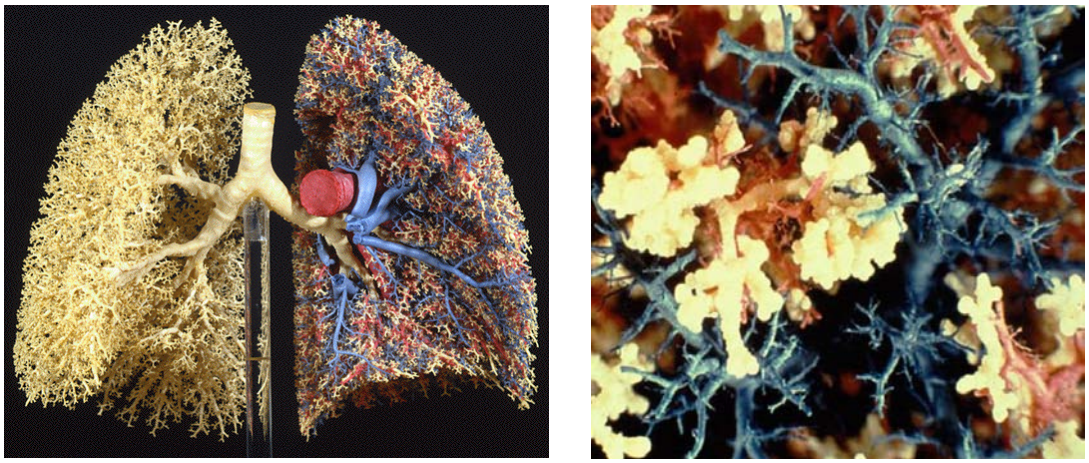

(a) (b)

Figure 1.2: Resin casts of the airways and blood vessels from [2]: (a) shows the airway of the lungs on the left-hand side and the airways with the pulmonary arteries and veins on the right-hand side. (b) shows a close-up version of the casts where the arteries follow the airway to the periphery and the veins are lying between the alveoli.

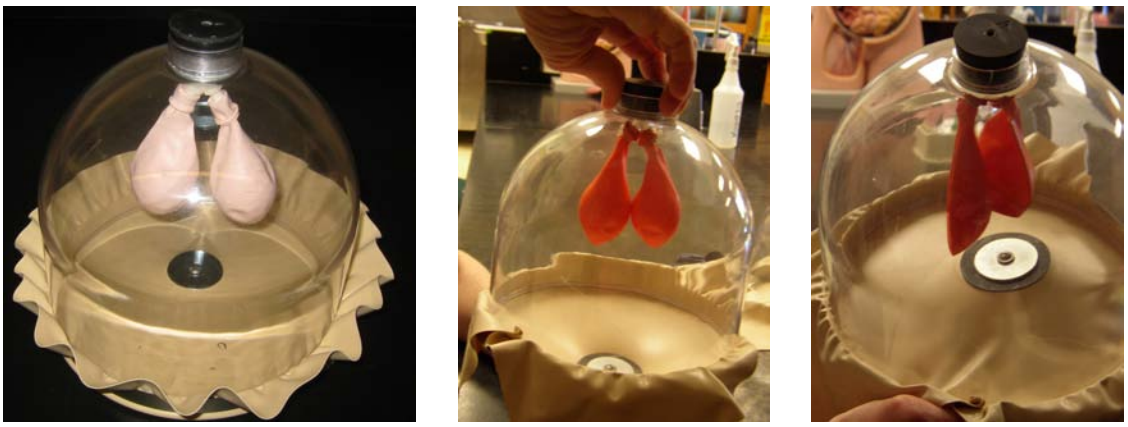

(a) (b) (c)

Figure 1.3: A simplified physical model of the respiratory system from [3]. (a) It is consisted of two balloons within an airtight glass dome sealed with a flexible membrane to simulate the thorax and the diaphragm. (b) The balloons inflate as the simulated diaphragm goes down. (c) The balloon deflate as the simulated diaphragm goes up.

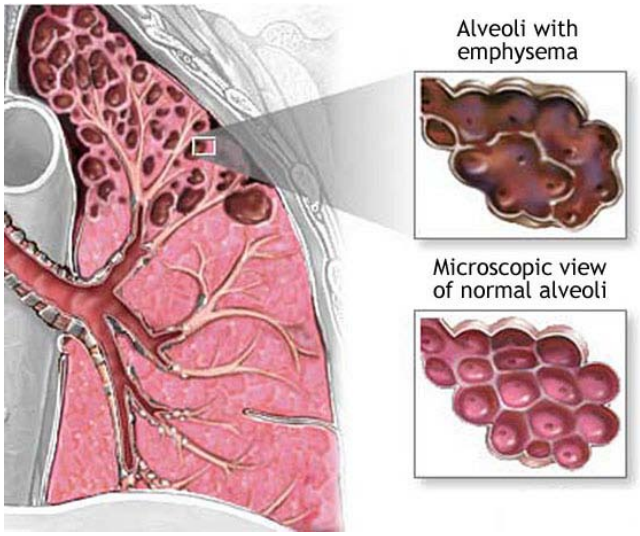

Figure 1.4: COPD involves damage to the air sacs (alveoli) and destruction of lung tissue around smaller airways (bronchioles), which changes the material properties of the lung tissue [4].

microspheres, are not possible for translation to humans [13, 14, 15]. Nuclear medicine imaging such as positron emission tomography (PET) and single photon emission CT (SPECT) can provide an assessment of lung function [16], but its application is constrained by low spatial resolution in pulmonary imaging when images are acquired across several respiratory cycles. Venegas et al. have used PET to study patchiness in asthma [17]. However the experiments were limited to 6.5 mm slice thickness and 10 cm axial coverage. Standard CT, on the other hand, has been the main diagnostic modality for evaluation of lung diseases and can provide high-resolution images but it is largely static and does not provide ventilation assessment. Hyperpolarized noble gas MR imaging has been developed for functional imaging of pulmonary ventilation [18, 19, 20]. The most common marker gases for lung studies are helium (He^3), xenon (Xe^{129}) and fluorene (F^{19}). Another method for the assessment of regional ventilation

by MRI is the use of oxygen for signal enhancement. The signal from paramagnetic O_2 is inferior to that from spin-polarized He^3, but the method is less complex and provides clinically useful information. Although MR imaging avoids the concern about ionizing radiation, there is insufficient signal from airway walls to visualize anything but the largest airways.

Finally, the other imaging modality to directly assess lung function is the xenon-enhanced CT (Xe-CT) which measures regional ventilation by observing the gas wash-in and wash-out rate on serial CT images. Marcucci et al. [21] used the Xe-CT ventilation method to investigate the distribution of regional lung ventilation and air content in healthy, anesthetized, mechanically ventilated dogs in the prone and supine postures. Vertical gradients in regional ventilation and air content were measured in in both prone and supine postures at different axial lung locations. Tajik et al. [22] implemented single-breath and/or dynamic multibreath wash-in and washout protocols with respiratory- and cardiac-gated image acquisition. In their study, the effects of varying tidal volume and inspiratory flow rate were evaluated independently. Chon et al. [23] compared the WI and WO rates by measuring WO-WI in different anatomic lung regions of anesthetized, supine sheep scanned using multi-detector-row computed tomography (MDCT). They also investigated the effect of tidal volume, image gating (end-expiratory EE versus end-inspiratory EI), local perfusion, and inspired Xe concentration on this phenomenon. Fuld et al. [24] studied the correlation between the CT-measured regional specific volume change and regional ventilation by Xe-CT in supine sheep. An overall correlation coefficient of $r^2 =$

0.66 was found between the two measurements. However, Xe-CT also has some shortcomings. Compared with standard CT, it involves inhalation of stable Xenon by the patient, with possible side effects, and necessitates expensive and complex equipment, available only in few medical centers. Xe-CT imaging protocols require high temporal resolution imaging, so axial coverage is usually limited. Z-axis coverage with modern multi-detector scanners currently ranges from about 2.5 to 12 cm, but the typical z-axis extent of the human lung is on the order of 25 cm.

While developing pulmonary imaging techniques to assess lung function is attracting great interests of research, recently, investigators from other groups have studied the lung function in the perspective of lung mechanics. Guerrero et al. have used optical-flow registration to compute lung ventilation from 4D CT [25, 26]. In their studies, they applied optical-flow deformable registration algorithm to map each corresponding tissue element across the 4DCT data set. The local change in fraction of air per voxel (local ventilation) was calculated from local average CT values. The 4D ventilation image set was then calculated using pairs formed with the maximum expiration image volume, the exhalation phases and then the inhalation phases representing a complete breath cycle. They compared the calculated total ventilation to the change in contoured lung volumes between the CT pairs to validate their result.

Gee et al. have used non-rigid registration to study pulmonary kinematics [27, 28] using magnetic resonance imaging. They obtained estimates of pulmonary motion by summing the normalized cross-correlation over serially acquired lung images to identify corresponding locations between the images. In their studies, the estimated

motions were modeled as deformations of an elastic body and thus reflect to a first order approximation the true physical behavior of lung parenchyma. The Lagrangian strain, derived from the calculated motion fields, were used to quantify the tissue deformation induced in the lung over the serial acquisition.

Christensen et al. used image registration to match images across cine-CT sequences and estimate rates of local tissue expansion and contraction [29] and their measurements matched well with spirometry data. In their studies, a relationship between tracking lung motion using spirometry data and image registration of consecutive CT image volumes collected from a multislice CT scanner over multiple breathing periods is described. In four out of five individuals, the average log-Jacobian value and the air flow rate correlated well ($r^2 = 0.858$ on average for the entire lung). The correlation for the fifth individual was not as good ($r^2 = 0.377$ on average for the entire lung) and can be explained by the small variation in tidal volume for this individual. The correlation of the average log-Jacobian value and the air flow rate for images near the diaphragm correlated well in all five individuals ($r^2 = 0.943$ on average).

Kabus et al. [30] compared the intensity based and the Jacobian based ventilation measure by applying two different image registration algorithms, the volume based and the surface based registrations. They showed that the Jacobian based ventilation has less error than the intensity based ventilation analysis using the segmented total lung volume as a global comparison. Later, they used the same validation methods as described in Chapter 2 and compared different image registration algo-

rithms [31]. They showed that even with the same registration accuracy evaluated by landmark error, there are large regional difference of the Jacobian maps.

Ehrhardt et al. [32] proposed a method to compute a 4D statistical model of respiratory lung motion which consists of a 3D shape atlas, a 4D mean motion model and a 4D motion variability model. They also adapted the generated statistical 4D motion model to a patient-specific lung geometry and the individual organ motion.

While they were able to show that their accumulated measurement matched well with the global measurement, they were not able to compare the registration-based measurements to local measures of regional tissue ventilation. In other words, they were not able to validate their methods at regional level to show the linkage between lung mechanics and lung function.

1.3 Pulmonary CT Imaging

Over the past decade, computed tomography (CT) theory, techniques and applications have undergone a rapid development. The advances in X-ray CT such as transitioning from fan-beam to cone-beam geometry, from single-row detector to multiple-row detector arrays and from conventional to spiral CT allow larger scanning range in shorter time with higher image resolution, and have more medical and other applications [33]. The principles of data acquisition and processing for CT can be appreciated by considering the development from the first-generation scanners to the fourth-generation scanners. A schematic of the basic operation of a first-generation scanner is shown in Figure 1.5. The source and the detector move in a series of linear steps, and then both are rotated and the process repeated. As shown in Figure 1.6,

in second-generation scanners, instead of the single beam, a thin fan beam of X-rays was produced. Third-generation scanners, use a much wider X-ray fan beam and a sharply increased number of detectors. In the fourth-generation scanner a complete ring of detectors surrounds the patient. There is no intrinsic decrease in scan time for fourth-generation with respect to third-generation scanners.

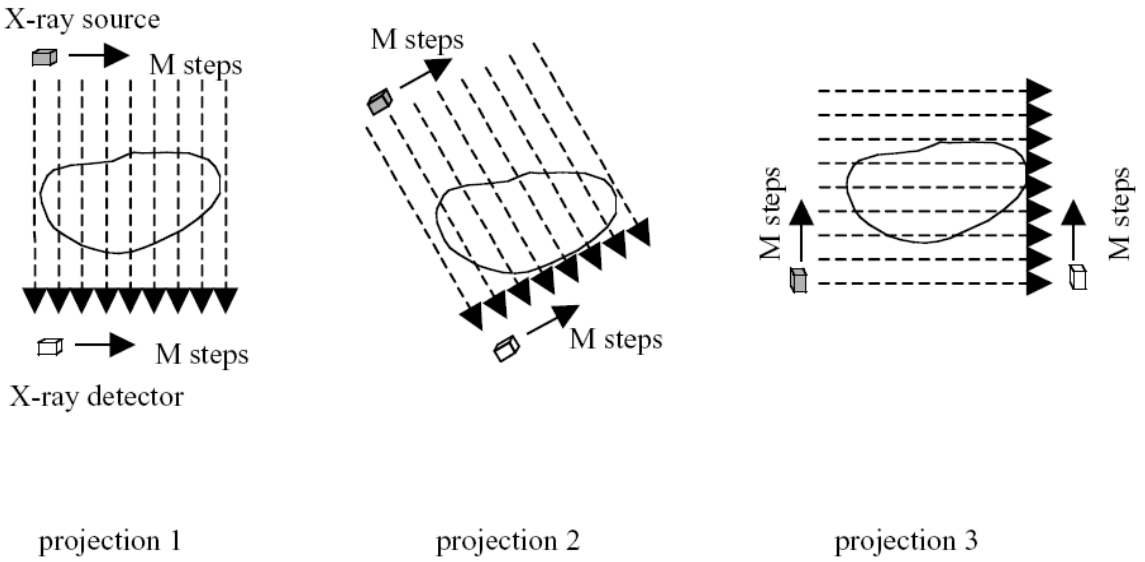

Figure 1.5: The mode of operation of a first-generation CT scanner. The source and the detector move in a series of linear steps, and then both are rotated and the process repeated. Figure from [5].

Image reconstruction takes place in parallel with data acquisition. It is preceded by a series of corrections to the acquired projections. The corrections are made for the effects of beam hardening, in which the effective energy of the X-ray beam increase as it passes through the patient due to greater attenuation of lower X-ray energies. The corrections are also made for imbalances in the sensitivities of individual

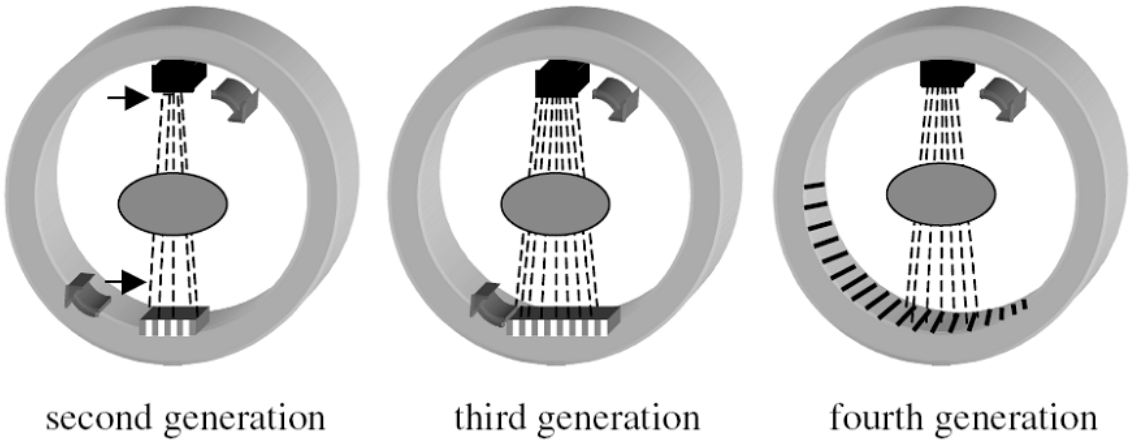

Figure 1.6: A schematic showing the development of second-, third-, and fourth-generation CT scanners. Figure from [5].

detectors and detector channels.

Radon transform is the mathematical basis for reconstruction of an image from a series of projections. For an arbitrary function $f(x, y)$, its Radon transform is defined as a integral of $f(x, y)$ a long a line L as shown in Figure 1.7,

$$\mathbb{R}\{f(x,y)\} = \int_L f(x,y)dl. \tag{1.1}$$

Each projection $p(r, \phi)$ can be expressed by

$$p(r,\phi) = \mathbb{R}\{f(x,y)\}, \tag{1.2}$$

where $p(r, \phi)$ represents the projection data acquired as a function of r, the distance along the projection and ϕ, the rotation angle of the X-ray source and detector. Reconstruction of the image requires computation of the inverse Radon transform of

the acquired projection data. The most common methods to compute the inverse Radon transform include backprojection and filter backprojection algorithms.

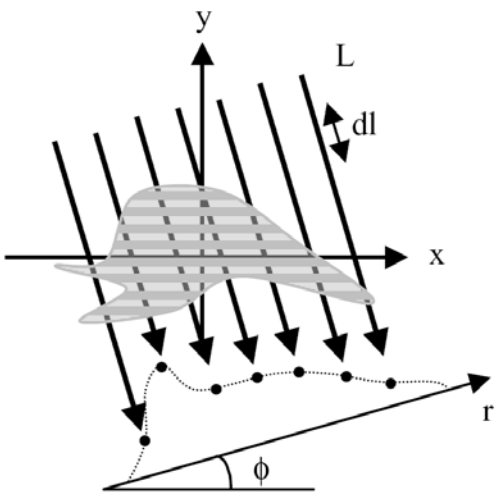

Figure 1.7: Line integrals defining the Radon transform of an object. Figure from [5].

Helical CT was developed to cover a larger volume of the body in a short time. The data are acquired as the table position is moved continuously in the scanner, as shown in Figure 1.8. Simultaneous motion of the patient bed and rotation of the X-ray source and detectors results in a spiral trajectory of the X-rays transmitted through patient. The spiral can either be loose (a high value of the spiral pitch) or tight (a low value of the spiral pitch). A number of data acquisition parameters are under control. The most important parameter is the spiral pitch p. The spiral pitch is defined as the ratio of the table feed d per rotation of the X-ray source to the

collimated slice thickness S:

$$p = \frac{d}{S}. \tag{1.3}$$

For p values less than 1, the X-ray beams of adjacent spiral overlap, resulting in a high tissue radiation dose. For large values of p, the image blurring is greater and the effective slice thickness increases.

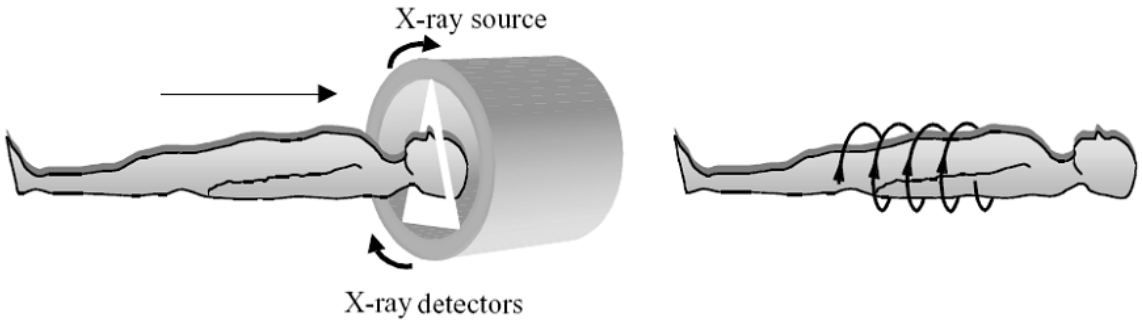

Figure 1.8: The principle of spiral CT acquisition. Simultaneous motion of the patient bed and rotation of the X-ray source and detectors (left) results in a spiral trajectory (right) of the X-rays transmitted through patient. The spiral can either be loose (a high value of the spiral pitch) or tight (a low value of the spiral pitch). Figure from [5].

Standard CT imaging has been used to study lung since 1980s via scanner developed at Mayo Clinic (Rochester, MN), known as the dynamic spatial reconstructor [34, 35]. Because early scanners required up to 2 to 5 s for acquiring and reconstruction of a single slice of the lung, CT imaging was mainly static and only for structures. With the emergence of the multidetector-row CT (MDCT), it is now possible to image both structure and function via use of a single imaging modality [36].

Current MDCT provides the ability of acquiring up to 64 thin sections with scanner rotation speeds on the order of 0.33 s/revolution. Operated in a spiral mode, these scanners can acquire images of the lung in a breath hold as short as 5 to 10 seconds.

Different pulmonary CT imaging protocols image lungs at different volume and capacities. Figure 1.9 shows an example of the lung volumes and capacities recorded on a spirometer, an apparatus for measuring inspired and expired volumes. Their definitions are as:

Tidal Volume (TV): Volume inspired or expired with each normal breath.

Inspiratory Reserve Volume (IRV): Maximum volume that can be inspired over the inspiration of a tidal volume/normal breath. Used during exercise/exertion.

Expiratory Reserve Volume (ERV): Maximal volume that can be expired after the expiration of a tidal volume/normal breath.

Residual Volume (RV): Volume that remains in the lungs after a maximal expiration. It cannot be measured by spirometry.

Inspiratory Capacity (IC): Volume of maximal inspiration: IRV + TV.

Functional Residual Capacity (FRC): Volume of gas remaining in lung after normal expiration, cannot be measured by spirometry because it includes residual volume: ERV + RV.

Vital Capacity (VC): Volume of maximal inspiration and expiration: IRV + TV + ERV = IC + ERV.

Total Lung Capacity (TLC): The volume of the lung after maximal inspiration. The sum of all four lung volumes, cannot be measured by spirometry because it includes residual volume: IRV+ TV + ERV + RV = IC + FRC.

Commonly, a static breath-hold scan is at lung volume near FRC or TLC and a 4DCT dynamic scan is at lung volumes between FRC and FRC + TV. While regional lung-density patterns can be evaluated by static breath-hold imaging at well-controlled volumes [37, 38], regional ventilation can be assessed with respiratory-gated dynamic imaging and using contrast gas such as xenon. It is also possible to reconstruct the organ of interest at any various points with a representative physiological cycle using retrospective gating methods though more radiation dose is administered to the subject [39]. As the increasing momentum in CT imaging research, it is believed that the trends of improvements in acquisition time, spatial resolution and radiation dose will continue and therefore, the CT imaging will bring us new insights for lung anatomy, etiology, pathology and physiology.

1.4 Basic Concepts in Image Registration

In order to study lung mechanics, we wish to find the motion of all tissue inside the lung due to the interactions with each other caused by the change of the transpulmonary pressure. The motion of the lung tissue, can be expressed in the form of spatial function of each region of the lung if the mapping of the region between

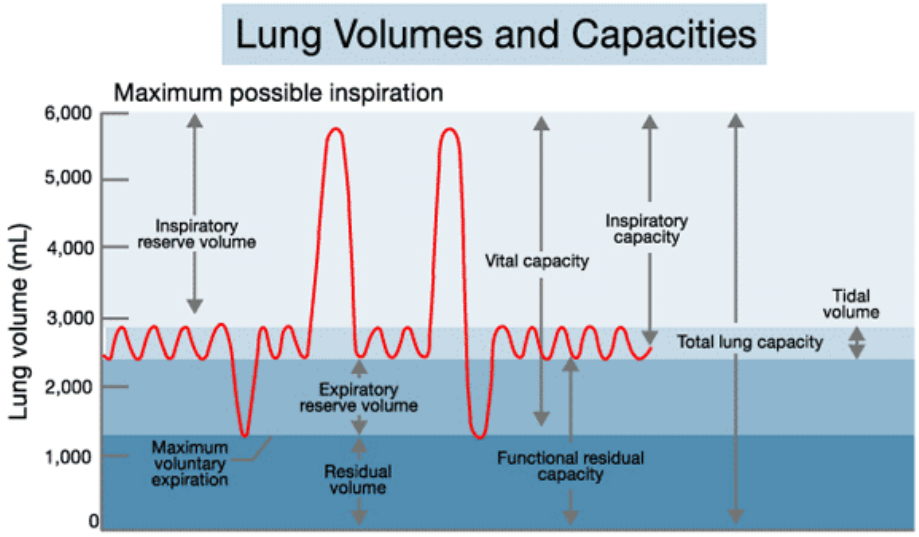

Figure 1.9: Lung volumes and capacities recorded on a spirometer, an apparatus for measuring inspired and expired volumes. Figure from [6].

different conditions can be found. Therefore, the problem can be stated as: Given images of the lungs in two or more different conditions, find the region mapping between the different conditions.

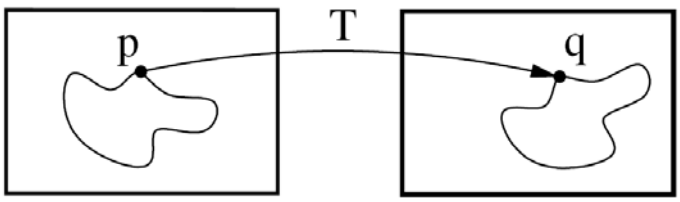

Figure 1.10: Image registration is the task of finding a spatial transormation matpping one image to another. Figure adapted from [7].

The problem statement brings us into the realm of image registration. Image registration is the task of finding a spatial transform mapping one image into another

as shown in Figure 1.10. Many image registration algorithms have been proposed and various features such as landmarks, contours, surfaces and volumes have been utilized to manually, semi-automatically or automatically define correspondences between two images [40, 41]. The basic components of the registration framework and their interconnections are shown in Figure 1.11 [7, 42].

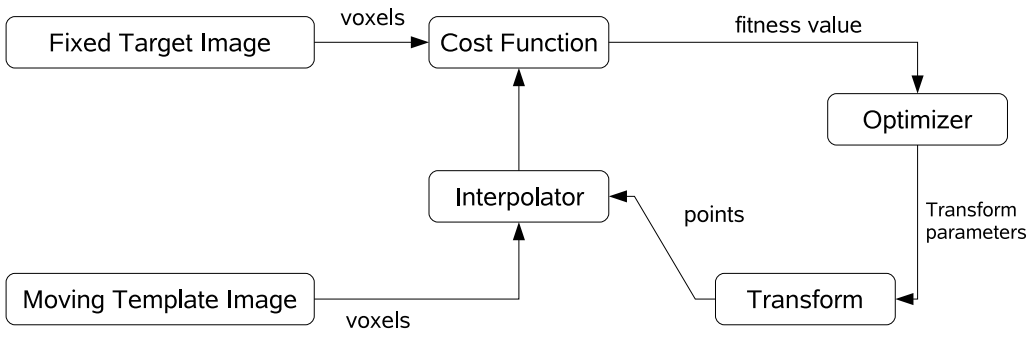

Figure 1.11: The basic components of the registration framework are two input images, a transform, a cost function, an interpolator and an optimizer. Adapted from [7].

Images: The input data to the registration process are two images. One is defined as the *moving* or *template* image I_1 and the other as the *fixed* or *target* image I_2. The registration is treated as an optimization problem with the goal of finding the spatial mapping that brings the features of the moving template image into alignment with the fixed target image. The input images can be resampled into different resolutions. The lower resolution images require less memory and computational time. The higher resolution images preserve the local details of the anatomical information. Usually,

a multi-resolution strategy is employed to speed-up registration and to make it more robust. The multi-resolution image registration starts from using a low resolution images of the original input images. Then the computed transform at that resolution is used to initialize the transform at the next level of registration with a higher resolution images of the original input images. This process repeats until the last level of resolution is done. The transform at each level of image resolution are composed to compute the final transform.

Transform: The transformation component $\mathbf{h}(\mathbf{x})$ defines how one image can be deformed to match another. The vector $\mathbf{x} = (x_1, x_2, x_3)^T$ defines the voxel coordinate within an image. The transformation $\mathbf{h}(\mathbf{x})$ can be a rigid transformation which can be described very compactly by a 3×3 matrix (9 parameters) $\mathbf{h}(\mathbf{x}) = \mathbf{A}\mathbf{x}$. It can be a affine transformation with 12 parameters for a whole image: $\mathbf{h}(\mathbf{x}) = \mathbf{A}\mathbf{x} + \mathbf{b}$. Or non-rigid registration such as the spline-based registrations [43], elastic models [44], fluid models [45], and finite element (FE) models [46] etc. The interpolator is used to evaluate the template image intensities at non-rigid positions.

For the category of non-rigid transformations, B-splines [47] are often used as a parameterized transform. Let $\phi_i = [\phi_x(\mathbf{x}_i), \phi_y(\mathbf{x}_i), \phi_z(\mathbf{x}_i)]^T$ be the coefficients of the i-th control point $\mathbf{x}_i$ on the spline grid G along each direction. The transformation is represented as

$$\mathbf{h}(\mathbf{x}) = \mathbf{x} + \sum_{i \in G} \phi_i \beta^{(3)}(\mathbf{x} - \mathbf{x}_i), \tag{1.4}$$

where ϕ_i describes the displacements of the control nodes and $\beta^{(3)}(\mathbf{x})$ is a three-

dimensional tensor product of basis functions of cubic B-Spline as

$$\beta^{(3)}(\mathbf{x}) = \beta^{(3)}(x)\beta^{(3)}(y)\beta^{(3)}(z). \tag{1.5}$$

The control point grid is defined by the amount of space between control points, which can be different for each direction. B-splines have the advantage of local support which means that the transformation of a point can be computed from only a couple of surrounding control points. With a hierarchy of B-spline grids within same image resolution, a global transform can be found with large grid space and more local transform can be found from small grid space.

Cost function: The cost function component can consist of a single metric such as a similarity measure based on geometric and intensity approaches or a compound function with other regulations and constraints depending on potential models. It measures how well the fixed target image is matched by the transformed moving template image. This function forms the quantitative criterion to be optimized by the optimizer over the search space defined by the parameters of the transform. Several similarity measures are described below.

A simple and common metric is the sum of squared difference (SSD), which measures the intensity difference at corresponding points between two images. Mathematically, it is defined by

$$C_{\text{SSD}} = \int_{\Omega} \left\{ [I_2(\mathbf{x}) - I_1(\mathbf{h}(\mathbf{x}))]^2 \right\} d\mathbf{x}. \tag{1.6}$$

Mutual information (MI) expresses the amount of information that one image contains about the other one. Unlike SSD, it accounts for the lung intensity changes between scans. The negative mutual information cost of two images is defined as [48, 49]

$$C_{\mathrm{MI}} = -\sum_i \sum_j p(i,j) \log \frac{p(i,j)}{p_{I_1 \circ h}(i) p_{I_2}(j)}, \tag{1.7}$$

where $p(i,j)$ is the joint intensity distribution of transformed template image $I_1 \circ h$ and target image I_2; $p_{I_1 \circ h}$ and $p_{I_2}(j)$ are their marginal distributions, respectively. The histogram bins of $I_1 \circ h$ and I_2 are indexed by i and j. A misregistration will result in a decrease in the mutual information and increase of the cost.

A recently developed similarity metric, the sum of squared tissue volume difference (SSTVD) [50, 51, 52, 53], also accounts for the intensity change in the lung CT images. This similarity criterion aims to minimize the local difference of tissue volume inside the lungs scanned at different pressure levels. Assume the Hounsfield units (HU) of CT lung images are primarily contributed by tissue and air. Then the tissue volume in a voxel at position $\mathbf{x}$ can be estimated as $V(\mathbf{x}) = v(\mathbf{x}) \frac{HU(\mathbf{x}) - HU_{air}}{HU_{tissue} - HU_{air}}$ where $v(\mathbf{x})$ is the volume of voxel $\mathbf{x}$. It is assumed that $HU_{air} = -1000$ and $HU_{tissue} = 55$. The intensity similarity metric SSTVD is defined as

$$\begin{aligned} C_{\mathrm{SSTVD}} &= \int_{\mathbf{\Omega}} \left[V_2(\mathbf{x}) - V_1(\mathbf{h}(\mathbf{x})) \right]^2 d\mathbf{x} \\ &= \int_{\mathbf{\Omega}} \left[v_2(\mathbf{x}) \frac{I_2(\mathbf{x}) + 1000}{1055} - v_1(\mathbf{h}(\mathbf{x})) \frac{I_1(\mathbf{h}(\mathbf{x})) + 1000}{1055} \right]^2 d\mathbf{x} \end{aligned} \tag{1.8}$$

The Jacobian of a transformation $J(\mathbf{h}(\mathbf{x}))$ estimates the local volume changes resulted

from mapping an image through the deformation. Thus, the tissue volume in image I_1 and I_2 are related by $v_1(\mathbf{h}(\mathbf{x})) = v_2(\mathbf{x}) \cdot J(\mathbf{h}(\mathbf{x}))$.

In addition to the above similarity measures, shape based similarity measure such as vesselness measurement (VM), recently developed and combined to other similarity measures by Cao et al. [54], is also used to improve the accuracy in pulmonary CT registrations by incorporating shape information of the vascular trees inside the lungs. For more details about the cost function incorporating VM, please see Chapter 5.

Optimization: Most registration algorithms can employ standard optimization ways to solve the problems to find the good transformation and there are several existing methods in numerical analysis such as the partial differential equation (PDE) solvers to solve the elastic and fluid transformation, steepest gradient descent, the conjugate gradient method etc. Among them, a limited-memory, quasi-Newton minimization method with bounds (L-BFGS-B) [55] algorithm is commonly used in B-Splines based registration. During the optimization process, it is also possible to preserve certain properties by constrain the search space of the parameters. Based on the sufficient conditions to guarantee the local injectivity of functions parameterized by uniform cubic B-Splines proposed by Choi and Lee [56], the B-Splines coefficients can be constrained so that the transformation maintain the topology of two images.

Interpolator: The commonly used interpolators are nearest neighbor, linear and N-th order B-spline interpolators. The nearest neighbour interpolator is the most

simple technique requiring least computation, but it comes with low quality. The linear interpolator's returned value is a weighted average of the surrounding voxels. For B-spline interpolater, the higher the order the better the quality, but also requiring more computation. When the $N = 0$, it is the same as nearest neighbor interpolator and when $N = 1$, it is the same as linear interpolator.

After introducing the basic components in the registration framework, there are several other important issues. One of the most important analysis coming with development and implementation of image registration algorithms is the validation of the registration algorithm. It is used to prove that the algorithm can be applied to a specific task with acceptable errors depending on the task itself. It is usually done by the methods of analyzing the distance of the corresponding landmarks before and after registration. Though this method can estimate well the errors of rigid-registration, it cannot represent all the regions in the non-rigid registration. The validation of registration will be described in the following chapters in more detail.

Based on the registration tasks, the lung CT image registrations can also be categorized into inter-subject registration and intra-subject registration. The inter-subject registration utilizes registration to find common anatomical structures or characteristics of the lungs. Li et al. [57] used landmark and intensity-based consistent image registration algorithm to compute a averaged human lung atlas from a population of normal subjects. The intra-subject lung registration focuses on measuring the shape changes or the function changes between two states of the lung. The results from our work in this thesis belong to this category. Since the inter-subject

and intra-subject lung registrations are application oriented, it is very important to choose the ideal cost function and registration models for the application. For example, the SSTVD cost is based on the assumption that the tissue volume is preserved between scans. The assumption will not hold for the intra-subject registration tasks registering scans with long time apart and it will not hold for inter-subject registration as well, considering the large anatomical difference of the lungs between subjects.

Our problem now remains in to find an ideal registration algorithm that best describes the transform of the regions of the lung between different conditions. Based on the assumptions that lung is an elastic body and that the requirements of our study that a specific region should be able to be trackable across different conditions, we introduce several registration algorithms in the following chapters which are armed with these features.

1.5 Regional Mechanics Measures from Image Registration

With the image registration displacement field, functional and mechanical parameters such as the regional volume change and compliance, stretch and strain, anisotropy, and specific ventilation can be evaluated.

We now introduce our calculation for regional mechanical parameters. The set of all particles which constitute the solid body will occupy the domain $\Omega \in \mathbb{R}^3$. The domain Ω is assumed to be the reference configuration of a moving body and points $\mathbf{x} \in \Omega$ are called material points. A transformation φ is a class C^2 function which maps any point $\mathbf{X}$ in the deformed configuration Ω^φ (= "$\varphi(\Omega)$") at time t

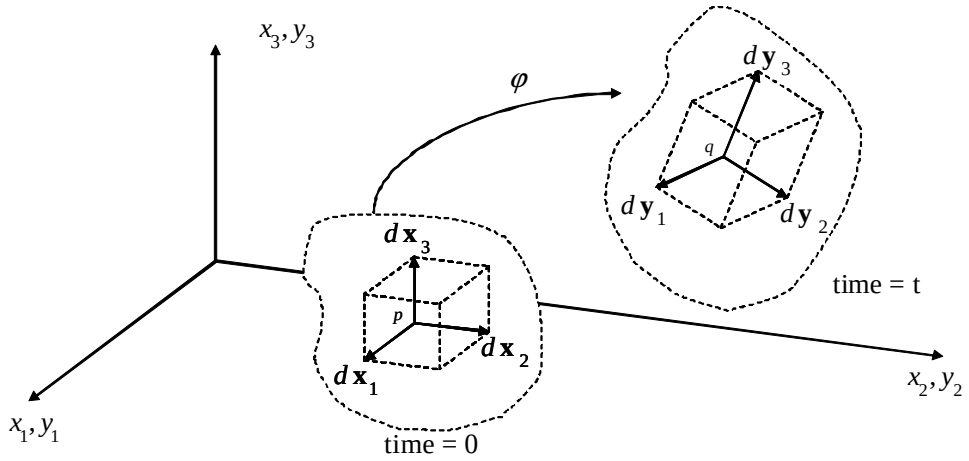

Figure 1.12: Deformation of a continuum body from the reference configuration (left) to the current configuration (right). Adapted from [8].

into its corresponding point $\mathbf{x}$ in the reference configuration at time t_0. Figure 1.12 depicts a cubic body of tissue occupying a reference configuration (left dash line) that is deformed to the current configuration (right dash line) at time t. The spatial position occupied by the material point $\mathbf{y}$ at time t is given by the transformation. The transformation or deformation $\mathbf{y} = \varphi(\mathbf{x}); \forall \mathbf{x} \in \Omega$. For any transformation which is placed in the Euclidean space, we can define the displacement field according to:

$$\mathbf{u}(\mathbf{x}) = \mathbf{y} - \mathbf{x} = \varphi(\mathbf{x}) - \mathbf{x}. \tag{1.9}$$

The deformation gradient is given by:

$$\mathbf{F} = \begin{pmatrix} \frac{\partial \varphi_1}{\partial x_1} & \frac{\partial \varphi_1}{\partial x_2} & \frac{\partial \varphi_1}{\partial x_3} \\ \frac{\partial \varphi_2}{\partial x_1} & \frac{\partial \varphi_2}{\partial x_2} & \frac{\partial \varphi_2}{\partial x_3} \\ \frac{\partial \varphi_3}{\partial x_1} & \frac{\partial \varphi_3}{\partial x_2} & \frac{\partial \varphi_3}{\partial x_3} \end{pmatrix}. \tag{1.10}$$

Regional volume change and compliance: The following derivation can be found in solid mechanics textbook [8]. Consider the infinitesimal volume element in the reference configuration (cube inside left dash line) in Fig. 1.12 with edges parallel to the Cartesian axes. The elemental material volume dv defined by

$$dv = dx_1 dx_2 dx_3, \tag{1.11}$$

In order to obtain the corresponding deformed volume, dV, in the deformed configuration (cube inside right dash line), note first that the vectors obtained by pushing forward the previous material vectors are,

$$\begin{aligned} d\mathbf{y}_1 &= \mathbf{F} d\mathbf{x}_1 = \frac{\partial \varphi_1}{\partial x_1} dx_1 \\ d\mathbf{y}_2 &= \mathbf{F} d\mathbf{x}_2 = \frac{\partial \varphi_2}{\partial x_2} dx_2 \\ d\mathbf{y}_3 &= \mathbf{F} d\mathbf{x}_3 = \frac{\partial \varphi_3}{\partial x_3} dx_3, \end{aligned} \tag{1.12}$$

The triple product of these elemental vectors gives the deformed volume as,

$$dV = d\mathbf{y}_1 \cdot (d\mathbf{y}_2 \times d\mathbf{y}_3) = \frac{\partial \varphi_1}{\partial x_1} \cdot (\frac{\partial \varphi_2}{\partial x_2} \times \frac{\partial \varphi_3}{\partial x_3}) dx_1 dx_2 dx_3, \tag{1.13}$$

Noting that the above triple product is the determinant of the $\mathbf{F}$ gives the volume change in terms of the Jacobian J as,

$$dV = J dv; J = \det(\mathbf{F}), \tag{1.14}$$

or,

$$J(\varphi(\mathbf{x})) = \begin{vmatrix} \frac{\partial \varphi_1}{\partial x_1} & \frac{\partial \varphi_1}{\partial x_2} & \frac{\partial \varphi_1}{\partial x_3} \\ \frac{\partial \varphi_2}{\partial x_1} & \frac{\partial \varphi_2}{\partial x_2} & \frac{\partial \varphi_2}{\partial x_3} \\ \frac{\partial \varphi_3}{\partial x_1} & \frac{\partial \varphi_3}{\partial x_2} & \frac{\partial \varphi_3}{\partial x_3} \end{vmatrix}. \tag{1.15}$$

Pulmonary compliance was defined as the change in volume per change in pressure $PC = \Delta V / \Delta P$ if pressure P is available.

Regional stretch and strain: The deformation gradient tensor $\mathbf{F}$ can be decomposed into stretch and rotation components:

$$\mathbf{F} = \mathbf{R}\mathbf{U}, \tag{1.16}$$

where the $\mathbf{U}$ is the right stretch tensor and $\mathbf{R}$ is an orthogonal rotation tensor. The Cauchy-Green deformation tensor is defined as

$$\mathbf{C} = \mathbf{F}^T\mathbf{F} = \mathbf{U}^2. \tag{1.17}$$

In order to obtain $\mathbf{U}$ from this equation, it is first necessary to evaluate the principal directions of $\mathbf{C}$, denoted here by the eigenvector N_1, N_2 and N_3 and their corresponding eigenvalues λ_1^2, λ_2^2 and λ_3^2. Therefore, after eigendecomposition and taking the square root of the eigenvalues of $\mathbf{C}$, we can get the eigenvalues λ_1, λ_2 and λ_3, and $\lambda_1 > \lambda_2 > \lambda_3$ of $\mathbf{U}$.

The concept of strain is used to evaluate how much a given displacement differs

locally from a rigid body displacement [8]. One of such strains for large deformations is the Lagrangian finite strain tensor, also called the Green-Lagrangian strain tensor or Green-St. Venant strain tensor, defined as:

$$\mathbf{E} = \frac{1}{2}(\mathbf{C} - \mathbf{I}) = \frac{1}{2}(\mathbf{F}^T\mathbf{F} - \mathbf{I}), \tag{1.18}$$

or,

$$\mathbf{E} = \begin{pmatrix} \varepsilon_{11} & \varepsilon_{12} & \varepsilon_{13} \\ \varepsilon_{21} & \varepsilon_{22} & \varepsilon_{23} \\ \varepsilon_{31} & \varepsilon_{32} & \varepsilon_{33} \end{pmatrix}. \tag{1.19}$$

Regional anisotropy: However, since the stretch and strain tensors are matrices and cannot be easily displayed, we extract the direction information such as fractional anisotropy, anisotropic deformation index and anisotropy ratio index, in additional to the magnitude information such as Jacobian from it:

The fractional anisotropy (FA) [58] is defined by

$$FA = \sqrt{\frac{3}{2}}\frac{\sqrt{(\lambda_1 - \lambda)^2 + (\lambda_2 - \lambda)^2 + (\lambda_3 - \lambda)^2}}{\sqrt{{\lambda_1}^2 + {\lambda_2}^2 + {\lambda_3}^2}}. \tag{1.20}$$

The anisotropy ratio index (ARI) is defined by

$$ARI = \frac{\lambda_1}{(\lambda_2 + \lambda_3)/2}. \tag{1.21}$$

The volume ratio (VR) is defined by

$$VR = \frac{\lambda_1\lambda_2\lambda_3}{(\frac{\lambda_1+\lambda_2+\lambda_3}{3})^3}. \tag{1.22}$$

Amelon et al. has proposed the slab-rod index (SRI) and anisotropic deformation index (ADI) as measures of tissue deformation (unpublished work), and they are defined by

$$SRI = \frac{\tan^{-1}(\frac{\lambda_3(\lambda_1-\lambda_2)}{\lambda_2(\lambda_2-\lambda_3)})}{\pi/2}, \tag{1.23}$$

and

$$ADI = \sqrt{(\frac{\lambda_1-\lambda_2}{\lambda_2})^2 + (\frac{\lambda_2-\lambda_3}{\lambda_3})^2}. \tag{1.24}$$

Specific ventilation: Now we define the CT based measurement of specific ventilation. Let I_1 and I_2 represent two 3D image volumes to be registered. The vector $\mathbf{x} = (x_1, x_2, x_3)^T$ defines the voxel coordinate within an image. The image registration algorithms find the optimal transformation $\mathbf{h}$ that maps the template image I_1 to the target image I_2.

The regional ventilation is equal to the difference in local air volume change per unit time. Therefore, the specific ventilation is equal to specific air volume change per unit time. Since the Jacobian tells us the local volume expansion or contraction, and if we assume that local volume change is only due to air flow, then the specific

air volume change by specific volume change (SAJ) is defined as

$$SAJ = J(\mathbf{x}) - 1. \tag{1.25}$$

The Hounsfield units (HU) in the lung CT images is a function of tissue and air content. Therefore, two other specific air volume changes can be defined using the air content information from CT. The specific air volume change by corrected Jacobian (SACJ) is defined as

$$SACJ = J(\mathbf{x})\frac{I_1(\mathbf{h}(\mathbf{x}))}{I_2(\mathbf{x})} - 1. \tag{1.26}$$

The specific air volume change by intensity (SAI) is defined as

$$SAI = 1000\frac{I_1(\mathbf{h}(\mathbf{x})) - I_2(\mathbf{x})}{I_2(\mathbf{x})(I_1(\mathbf{h}(\mathbf{x})) + 1000)} \tag{1.27}$$

More details of the derivation of these measures can be found in Chapter 5.

1.6 Applications and Significance of Our Work

Many disease or injury conditions will change lung material properties, lung mechanics, and lung function. For example, emphysema has historically been identified and classified according to the macroscopic architecture of the excised, fixed whole lung [59]. Microscopically, it shows large air space with destructed alveoli (Figure 1.13(b)) in contrast to a fine alveoli network as in normal subjects (Figure 1.13(a)). On the other hand, pneumoconiosis (or progressive massive fibrosis)

shows aggregation of macrophages as granular, black areas (Figure 1.13(c)). Such patterns will result in region changes in the mechanical behavior of the tissue, which will be detectable in vivo using high-resolution CT imaging to follow the dynamic behavior of the tissue. Using X-ray CT images, Mishima et al. [60] have examined the fractal geometry of the lung parenchyma, and interpret their results on the basis of a large, elastic spring network. It is of great interest to identify CT-based methods to directly measure lung mechanical properties (e.g., the 3D strain fields) to be used in conjunction with the anatomical detail offered by X-ray CT. Pulmonary embolism is an enormous public health problem, with an annual incidence exceeding 500,000 and mortality up to 10% [61]. Although this effect is known to be a local regulatory phenomenon, the anatomic location of the local lung compliance change (bronchioles, ducts, etc.) or the extent or local propagation of the lung stiffening in the vicinity of the embolus have never been determined.

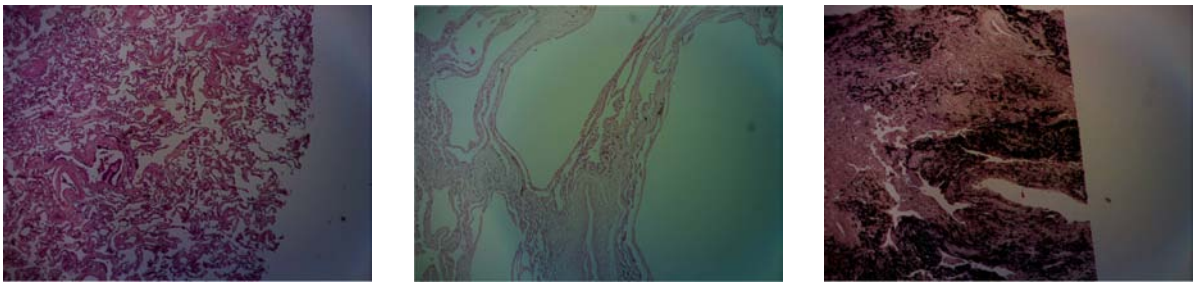

(a) (b) (c)

Figure 1.13: Microscopic sections from human lungs. (a) Section from a normal subject with fine network of tissue. (b) Section from a emphysema patient with large empty areas. (c) Section from a pneumoconiosis (progressive massive fibrosis) patient with black particles. Figure from [3].

In addition, the measurement of pulmonary function and mechanics may be useful as a planning tool during Radiation therapy planning. Radiation therapy (RT) for lung cancer is commonly limited to sub-therapeutic doses due to unintended toxicity to normal lung tissue. The radiation dose needed to control the tumor is well above that which causes toxicity to the normal lung tissue. Increase of tumor control could be achieved by delivering substantially higher radiation doses to the tumor [62], which is optimally achieved with RT delivery schemes that reduce toxicity. Reducing the frequency of occurrence and magnitude of normal lung function loss may benefit from treatment plans that incorporate relationships between regional and functional based lung information and the radiation dose. The measurement of pulmonary function and mechanics may may also be useful for tracking the progression of toxicity to nearby normal tissue during RT, and can be used to evaluate the effectiveness of a treatment post-therapy [63, 64].

In this thesis, we present a technique that uses multiple respiratory-gated CT images of the lung acquired at different levels of inflation with both breath-hold static scans and retrospectively reconstructed 4D dynamic scans, along with non-rigid 3D image registration, to make local estimates of lung tissue function and mechanics. We validate our technique using anatomical landmarks and functional Xe-CT estimated specific ventilation.

The major contributions of this thesis include: 1) developing the registration derived regional expansion estimation approach in breath-hold static scans and dynamic 4DCT scans, 2) developing a method to quantify lobar sliding from image

registration derived displacement field, 3) developing a method for measurement of radiation-induced pulmonary function change following a course of radiation therapy, 4) developing and validating different ventilation measures in 4DCT.

The ability of our technique to estimate regional lung mechanics and function as a surrogate of the Xe-CT ventilation imaging for the entire lung from quickly and easily obtained respiratory-gated images, is a significant contribution to functional lung imaging because of the potential increase in resolution, and large reductions in imaging time, radiation, and contrast agent exposure. Our technique may be useful to detect and follow the progression of lung disease such as COPD, may be useful as a planning tool during RT planning, may be useful for tracking the progression of toxicity to nearby normal tissue during RT, and can be used to evaluate the effectiveness of a treatment post-therapy.

1.7 Organization of the Thesis

This thesis is divided into 6 chapters. The rest of the thesis is organized as follows:

Chapter 2 presents our results on estimation of regional lung function from both dynamic and static image sequences. We report a technique that uses multiple respiratory-gated CT images and non-rigid 3D image registration to make local estimates of lung tissue expansion. We compare the ventral-dorsal patterns of lung expansion estimated in both retrospectively reconstructed dynamic scans and static breath-hold scans to a xenon CT based measure of specific ventilation and a semi-automatic reference standard in four anesthetized sheep studied in the supine

orientation. This chapter is based on:

1. Ding, K., Cao, K., Christensen, G.E., Raghavan, M.L., Hoffman, E.A., Reinhardt, J.M.: Registration-based lung tissue mechanics assessment during tidal breathing. In Brown, M., de Bruijne, M., van Ginneken, B., Kiraly, A., Kuhnigk, J.M., Lorenz, C., Mori, K., Reinhardt, J.M., eds.: First International Workshop on Pulmonary Image Analysis, New York (2008) 63

2. Ding, K., Cao, K., Christensen, G.E., Hoffman, E.A., Reinhardt, J.M.: newblock Registration-based regional lung mechanical analysis: Retrospectively reconstructed dynamic imaging versus static breath-hold image acquisition. Volume 7262., SPIE (2009) 72620D

Chapter 3 presents our results on evaluation of lobar sliding. We propose a method to evaluate the sliding motion of the lobar surfaces during respiration using lobe-by-lobe mass-preserving non-rigid image registration. We measure lobar sliding by evaluating the relative displacement on both sides of the fissure. This chapter is based on:

1. Ding, K., Yin, Y., Cao, K., Christensen, G.E., Lin, C.L., Hoffman, E.A., Reinhardt, J.M.: Evaluation of lobar biomechanics during respiration using image registration. In: MICCAI '09: Proceedings of the 12th International Conference on Medical Image Computing and Computer-Assisted Intervention, Berlin, Heidelberg, Springer-Verlag (2009) 739–746

Chapter 4 presents our results on comparison of pulmonary function change

following radiation therapy. We propose a method that quantitatively measures the regional changes in lung tissue function following a course of radiation therapy by using 4DCT and image registration techniques. This chapter is based on:

1. Ding, K., Bayouth, J.E., Buatti, J.M., Christensen, G.E., Reinhardt, J.M.: 4DCT-based measurement of changes in pulmonary function following a course of radiation therapy. Medical Physics **37**(3) (2010) 1261–1272

Chapter 5 presents our results on comparison of the regional measures of regional specific ventilation. We compare three different 4DCT based registration derived measures of regional ventilation to xenon-CT (Xe-CT). 4DCT and Xe-CT data sets from four adult sheep are used in this study. This chapter has not yet been published.

Chapter 6 concludes the thesis and proposes some interesting problems for future research.

CHAPTER 2
ESTIMATION OF PULMONARY FUNCTION IN DYNAMIC AND STATIC IMAGE SEQUENCES

2.1 Introduction

The lungs undergo expansion and contraction during the respiratory cycle. Pulmonary diseases can change the tissue material properties of lung parenchyma and the mechanics of the respiratory system. Pulmonary emphysema, a chronic obstructive pulmonary disease (COPD), is associated with decreased elasticity (increased compliance) of the lung tissue and idiopathic pulmonary fibrosis (IPF), a classic interstitial lung disease makes the tissue thicker and stiffer (reduced compliance). While the mechanical changes associated with the change of the material properties (and the disease processes themselves) originate at a regional level, they are largely asymptomatic and invisible to currently available global measures of lung function such as pulmonary function tests (PFTs) until they have significantly advanced and aggregated. Therefore it would be desirable to have objective methods with which to evaluate and follow the progression of disease from regional measurements. Recent advances in multidetector-row CT (MDCT) allow the entire lung to be imaged with isotropic 0.4 mm voxels in under 10 seconds. Additionally, new retrospective gating methods, initially used to reconstruct the beating heart, are being applied to produce high-resolution images of the entire breathing lung throughout the respiratory cycle. These dynamic imaging capabilities now permit the measurement of regional lung

mechanical properties which, in addition to recently established functional CT tools for measurement of regional lung ventilation [21, 22] and perfusion [65], will greatly enhance the quantitative characterization of lung structure and function.

Nuclear medicine imaging such as positron emission tomography (PET) and single photon emission CT (SPECT) can provide an assessment of lung function [16], but its application is limited by low spatial resolution in pulmonary imaging when images are acquired across several respiratory cycles. Xenon-enhanced CT (Xe-CT) measures regional ventilation by observing the gas wash-in and wash-out rate on serial CT images [21, 22, 23] but with limited axial coverage (modern MDCT currently only ranges from about 2.5 to 12 cm). Recently, investigators from other groups have studied the lung function using image registration techniques [25, 26, 27, 28, 29]. However, restricted by the experiment methods, they were not able to compare the local tissue expansion between dynamic and static imaging acquisitions. In addition, they either used very limited landmarks or global measurement such as spirometry to validate their regional estimates. In this chapter, we estimate regional lung tissue expansion using 3D image registration in both retrospectively reconstructed dynamic imaging and static breath-hold image acquisitions. We compare these two independent estimates of expansion to each other and to Xe-CT derived estimates of regional ventilation.

2.2 Materials and Methods

2.2.1 Data Acquisition

Appropriate animal ethics approval was obtained for these protocols from the University of Iowa Animal Care and Use Committee and the study adhered to NIH guidelines for animal experimentation. Four adult sheep were used for experiments. The sheep were anesthetized using intravenous pentobarbital and mechanically ventilated during experiments. All images were acquired with the animals in the supine orientation on a Siemens Sensation 64 multi-detector CT scanner (MDCT) (Siemens Medical Solutions; Erlangen, Germany).

Volumetric CT Data Acquisition by Retrospectively Reconstructed Dynamic Imaging The dynamic scans are acquired using the dynamic imaging protocol during tidal breathing with a pitch of 0.1, slice collimation 0.6 mm, rotation time 0.5 sec, slice thickness 0.75 mm, increment 0.5 mm, 120 kV, 400 mAs, and kernel B30f. Images are reconstructed retrospectively at 0, 25, 50, 75, and 100% phase points of the inspiratory portion and 75, 50 and 25% of the expiration portion of the respiratory cycle (herein denoted as the $T0$, $T1$, $T2$, $T3$, $T4$, $T5$, $T6$, and $T7$ images).

Volumetric CT Data Acquisition by Static Breath-hold Imaging The static scans are acquired in static imaging protocol at 10, 15, 20, and 25 cm H_2O (herein denoted as the $P10$, $P15$, $P20$, and $P25$ images) airway pressure with the animal held apneic. The protocol used a tube current of 100 mAs, a tube voltage 120 kV, slice collimation of 0.6 mm, an effective slice thickness of 0.75 mm, a slice separation

of 0.5 mm, a pitch of 1, and a field of view selected to fit the lung field of interest. Both of the two types of scans are acquired with a reconstruction matrix of 512 by 512 and without moving the animal between scans, so after acquisition the data sets are in rigid alignment.

Xenon CT Data Acquisition The axial locations for the Xe-CT studies are selected from the whole lung volumetric scan performed near end-expiration. Images are acquired with the scanner set in ventilation triggering mode, typically using 80 keV energy for higher Xe signal enhancement (as shown in a pilot study [66]), 160 mAs tube current, a 360° rotation, a 0.33 sec scan time, a 512 by 512 reconstruction matrix, and a field of view adjusted to fit the lung field of interest. The Xe-CT slice thickness is approximately 2.4 mm thick, or about 3.4 times thicker than the volumetric CT slices. Twelve contiguous xenon slices are acquired and provide approximately 3 cm of coverage along the axial direction. Respiratory gating during image acquisition is achieved by replacing the standard ECG gating signal with a trigger signal from a LabView program. Images were acquired at the end expiratory point during the respiratory cycle. A respiratory tidal volume of 8 cc/kg was used for the Xe-CT acquisition.

The image acquisition sequence is as follows. Acquisition starts and images are gathered as the animal breathes six to eight breaths of room air. Next, the xenon delivery system is turned on and approximately 40 breaths of pure xenon are delivered while imaging, and then the air source is switched back to room air for another 40 breaths. Thus, axial images are acquired for approximately 90 breaths as the xenon

gas washes in and out of the lungs.

2.2.2 Image Registration and Mechanical Analysis

Inverse consistent linear elastic image registration was applied to register image pairs [67]. The registration estimates the inverse consistency error between the forward and reverse transformation (see Figure 2.1), and hence provides more accurate correspondences between two images compared to independent forward and reverse transformations. Let the two input images of the registration be denoted as I_0 and I_1, and let the transforms between two images be h and g. The forward transformation h is used to deform the image I_0 into the shape of the image I_1, and the reverse transformation g is used to deform the shape of I_1 into that of I_0. The deformed template and target images are denoted by $(I_0 \circ h)$ and $(I_1 \circ g)$, respectively. The forward and reverse transformations are defined by the equations: $h(\mathbf{X}) = \mathbf{X} + u(\mathbf{X})$, $g(\mathbf{X}) = \mathbf{X} + w(\mathbf{X})$, $h^{-1}(\mathbf{X}) = \mathbf{X} + \tilde{u}(\mathbf{X})$, $g^{-1}(\mathbf{X}) = \mathbf{X} + \tilde{w}(\mathbf{X})$. The vector-valued functions u, w, $\tilde{u}$, and $\tilde{w}$ are called displacement fields since they define the transformation in terms of a displacement from a location $\mathbf{X}$.

The registration minimizes the cost function defined as:

$$\begin{aligned} C &= \sigma[C_{SIM}(I_0 \circ h, I_1) + C_{SIM}(I_1 \circ g, I_0)] + \\ &\quad \chi[C_{ICC}(u, \tilde{w}) + C_{ICC}(w, \tilde{u})] + \\ &\quad \rho[C_{REG}(u) + C_{REG}(w)], \end{aligned} \tag{2.1}$$

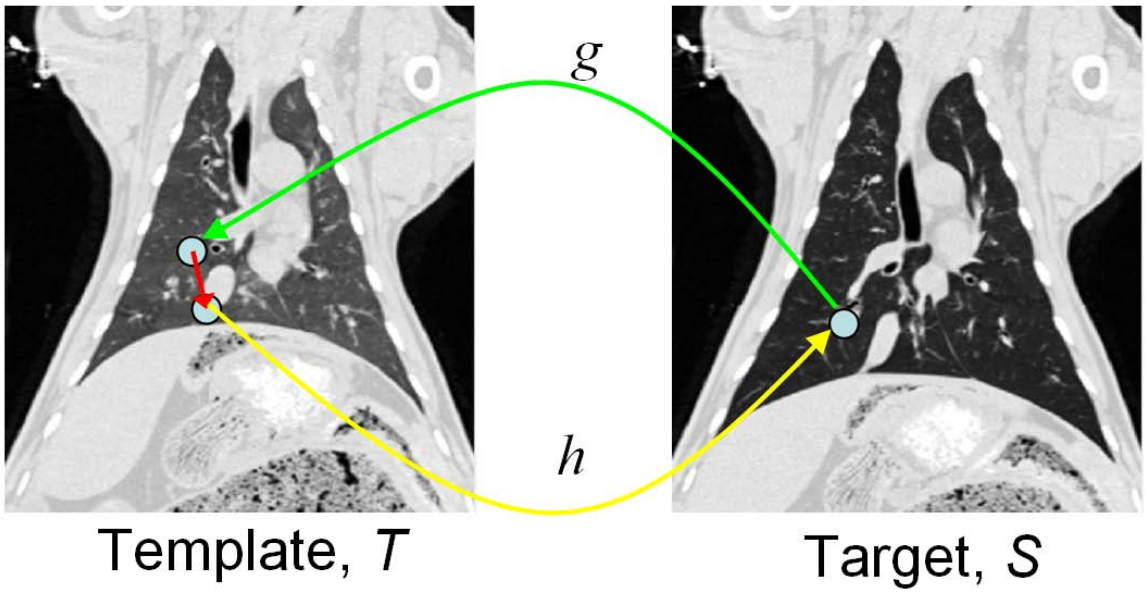

Figure 2.1: Inverse consistent linear elastic registration jointly estimating h&g helps reduce the inverse consistency error.

The C_{SIM} term of the cost function defines the symmetric intensity similarity. The C_{ICC} term is the inverse consistency constraint or inverse consistency error cost and is minimized when the forward and reverse transformations are inverses of each other. The C_{REG} term is used to regularize the forward and reverse displacement fields. A 3D Fourier series representation [68] is used to parameterize the forward and reverse transformations. Christensen and Johnson [67, 69] describe the Fourier series parameterization used in the consistent registration algorithm in detail. The constants σ, χ and ρ are used to enforce/balance the constraints. In our registrations, the mean squared intensity difference is used as similarity measure to drive the registration, and we set the weighting constants $\sigma = 1$, $\chi = 600$, and $\rho = 0.00125$. The parameters were decided on the basis of pilot experiments, previous work and experience. The forward

and reverse transformations are parameterized using Fourier series representation and the gradient descent is used in the optimization step. More details of the inverse consistent registration can be found in [67, 70].

After finding out the transforms and the correspondence for each voxel of two images, we are ready for mechanical analysis on a regional level. In three-dimensional space, the vector displacement function $\vec{u}(x, y, z)$ that maps image I_0 to image I_1 is used to calculate the local lung expansion using the Jacobian determinant $J(x, y, z)$ defined as:

$$J(x,y,z) = \begin{vmatrix} 1+\frac{\partial u_x(x,y,z)}{\partial x} & \frac{\partial u_x(x,y,z)}{\partial y} & \frac{\partial u_x(x,y,z)}{\partial z} \\ \frac{\partial u_y(x,y,z)}{\partial x} & 1+\frac{\partial u_y(x,y,z)}{\partial y} & \frac{\partial u_y(x,y,z)}{\partial z} \\ \frac{\partial u_z(x,y,z)}{\partial x} & \frac{\partial u_z(x,y,z)}{\partial y} & 1+\frac{\partial u_z(x,y,z)}{\partial z} \end{vmatrix},$$

where $u_x(x, y, z)$ is the x component of $\vec{u}(x, y, z)$, $u_y(x, y, z)$ is the y component of $\vec{u}(x, y, z)$, and $u_z(x, y, z)$ is the z component of $\vec{u}(x, y, z)$.

The Jacobian measures the differential expansion at position (x, y, z) in the image I_1. If the Jacobian is greater than one, there is local tissue expansion; if the Jacobian is less than one, there is local tissue contraction (Figure 2.2).

2.2.3 Image Preprocessing and Registration Procedures

All volumetric CT data were converted from DICOM format and stored in 16-bit Analyze^{TM} (Mayo Clinic, Rochester, MN) format. To reduce memory requirements during the image registration and increase the image contrast, the original 16-bit CT data were then converted to 8-bit values [0, 255] using a threshold window

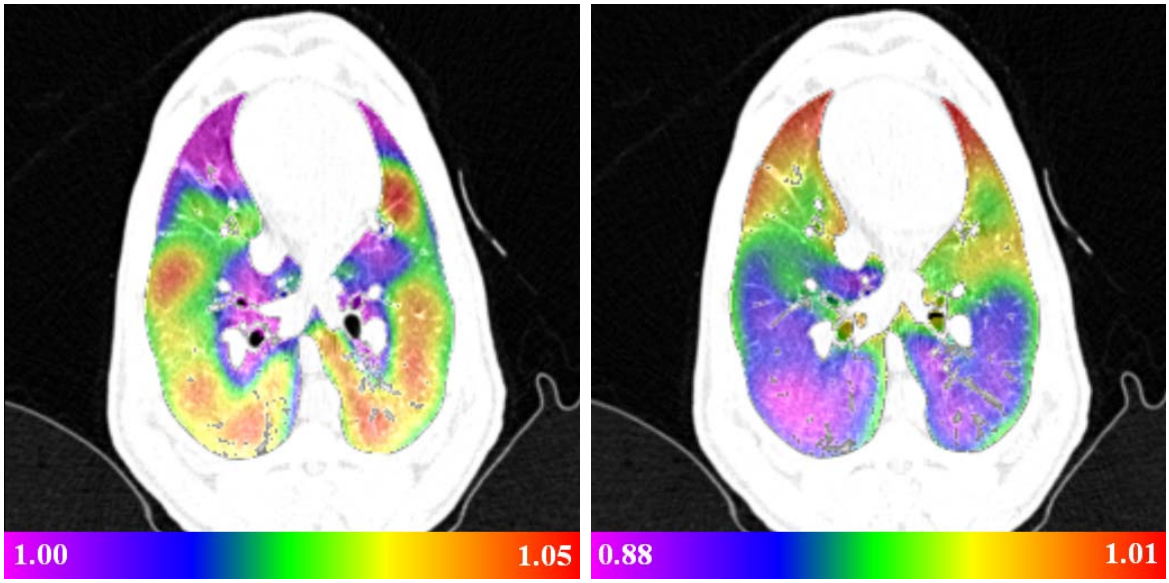

(a) (b)

Figure 2.2: Color-coded maps showing (a) the Jacobian of the image registration transformation (unitless) for approximately the same anatomic slice computed from the $T0-T1$ inspiration image pair and (b) the $T4-T5$ expiration image pair. Note that the color scales are different for (a) and (b). Red regions on the inspiration image (a) are regions that have high expansion while dark blue regions on the expiration image (b) have high contraction.

of [-1024HU, 0HU]. The intensity discontinuity at the boundary along the chest wall and the large intensity difference between the regions inside and outside the lung increase the mean squared intensity difference of our similarity measure and thus the total cost function, if the regions are misaligned at boundaries. In this way, the boundaries of each region are forced to match. Yet the matching does not constrain the sliding motion between the lungs and the ribs along the boundary at different pressure or phases (Figure 2.3)

As described Section 2.2.2, the inverse consistent registration algorithm uses Fourier series representation to parameterize the transformations, so it requires the

sizes of the input images to be a power of two. Therefore the images are padded with zeros to size $512 \times 512 \times 2^{\text{round}(\log_2 N_z)}$, where N_z is the size of the image in Z-direction. Then to reduce the memory requirements, the images are downsampled by a factor of two in all three directions using trilinear interpolation.

Since both of the dynamic and static scans are acquired without moving the animal between scans, and after acquisition the data sets are in rigid alignment, so the common rigid registration step to initially align two images as seen in other papers is not performed.

In our study, inverse consistent image registration followed by regional mechanical analysis as described in Section 2.2.2 is performed for $T0$ to $T1$, $T1$ to $T2$, ..., and $T6$ to $T7$ in the dynamic scans and for $P10$ to $P15$, $P15$ to $P20$ and $P20$ to $P25$ in the static scans.

2.2.4 Xenon CT and Specific Ventilation

Review of Xenon CT Imaging Xe-enhanced computed tomography (CT; Xe-CT) is a method for the noninvasive measurement of regional pulmonary ventilation in intact subjects [71, 21, 22]. Xenon is a nonradioactive, monatomic noble gas that is denser than air. When imaged in a conventional CT scanner, the density of Xe measured in Hounsfield units (HU) increases linearly with its concentration. When Xe concentrations of 30-60% in air are delivered to the lung, CT enhancements of parenchymal density of 50-150 HU are obtained. If the Xe is introduced and eliminated from the lung during a controlled washin-washout (wi/wo) ventilation protocol, repeat CT scans taken at constant lung volume (i.e., at the same point in the

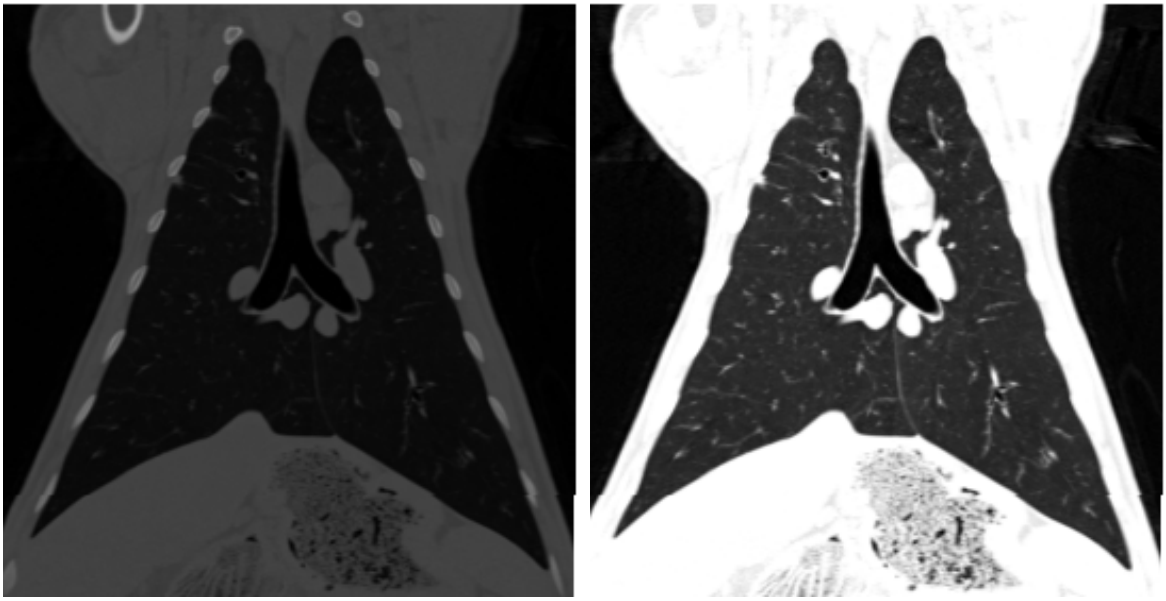

(a) (b)

Figure 2.3: The intensity transformation maps the CT values to 8-bit unsigned character data before registration. (a) Original CT data. (b) Data after intesity mapping.

respiratory cycle) will yield a local exponential density curve for any specified region of interest (ROI)within the lung field. The regional ventilation can be quantified by fitting a single-compartment exponential model to the rise and decay portions of the curve using a least-squares fit. For each ROI to be analyzed, the mean region density, $D(t)$, is calculated versus time (or equivalently, image number). For the wash-in phase, the compartment model gives [71]:

$$D(t) = \begin{cases} D_0 & 0 \leq t < t_0 \\ D_0 + (D_f - D_0)(1 - e^{-\frac{t-t_0}{\tau}}) & t \geq t_0, \end{cases} \tag{2.2}$$

where D_0 is the baseline density in the ROI prior to switching to xenon gas, D_f is the density that would be observed if xenon was inspired until equilibrium, t_0 is the start

time of the switchover from room air to xenon, and τ is the model time constant. Thus, using this model, the $D_f - D_0$ term represents the enhancement due to the inspired xenon. The model gives a similar expression for the wash-out phase:

$$D(t) = \begin{cases} D_f & 0 \leq t < t_0 \\ D_0 + (D_f - D_0)e^{-\frac{t-t_0}{\tau}} & t \geq t_0, \end{cases} \tag{2.3}$$

where for the wash-out phase t_0 denotes the time of switchover from xenon back to room air. Figure 2.4 shows the density–time variation predicted by the model.

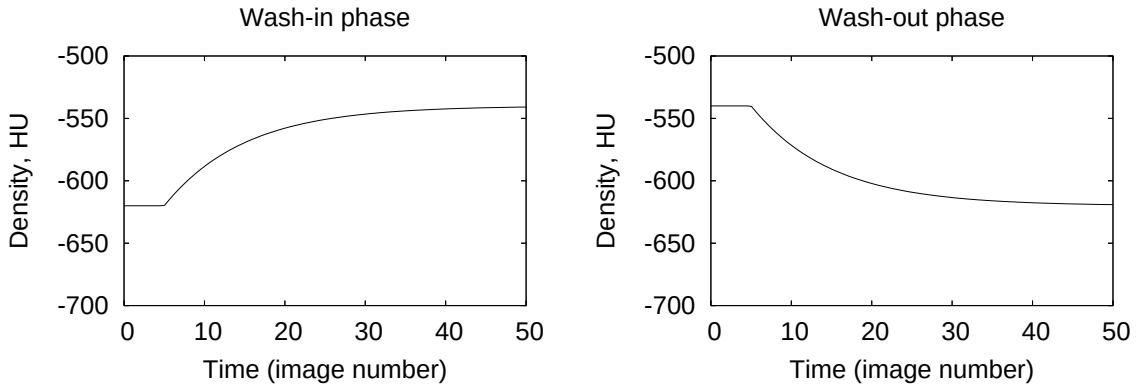

(a) (b)

Figure 2.4: Wash-in and wash-out behaviors predicted by compartment model for $t_0 = 5$ seconds, $\tau = 10$ seconds, $D_0 = -620$ HU, and $D_f = -540$ HU. Figure from [9]

.

Xenon CT Ventilation Analysis Prior to Xe-CT data analysis, the lung region was defined using the method from [72], followed, when necessary, by manual editing. Figure 2.5a shows an example Xe-CT slice with the lung segmentation overlaid. After

lung segmentation, non-overlapping 8×8 pixel regions of interest (ROIs) were defined in the lung region on each 2D slice.

As discussed by [23], the time constants of the rising and falling phases of the curves may be fitted separately or may be forced to be equal. In our analysis, only the wash-in phase of the Xe protocol was analyzed. To reduce aberrations in the time series data due to the ROIs overlapping with large blood vessels or regions of atelectasis (see, for example, the bottom left side of the lungs shown in Figure 2.5a), we eliminated from consideration any ROI that had more than 40% of its pixels above -300 HU. Time series data was measured and analyzed for the remaining ROIs. Specific ventilation (sV, ventilation per unit lung air volume in min^{-1}) for each ROI was calculated as the inverse of the time constant τ.

Figures 2.5a–b shows screen shots from the software tool "time-series image analysis" (TSIA) used to analyze the Xe-CT data [23]. This tool facilitates lung segmentation, region of interest specification, and allows control over the curve fitting parameters during the exponential fits.

2.2.5 Quantitative Evaluation of Registration Accuracy

Although registration result can be assessed by visual comparison, it is highly desired to have quantitative evaluation of registration accuracy. An attempt has been made to establish the registration reference by synthetically warping data such that the original image and the transformed image are known in advance as well as the ideal transform between them [73]. However, this approach provides only a generic evaluation and algorithm performance on real clinical data cannot be measured in

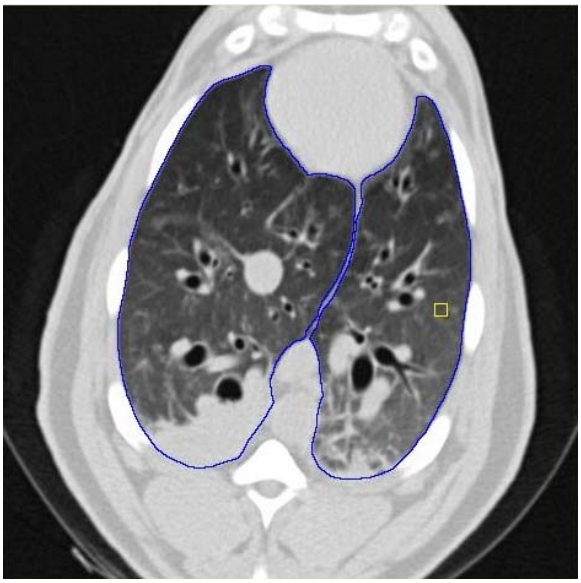

(a)

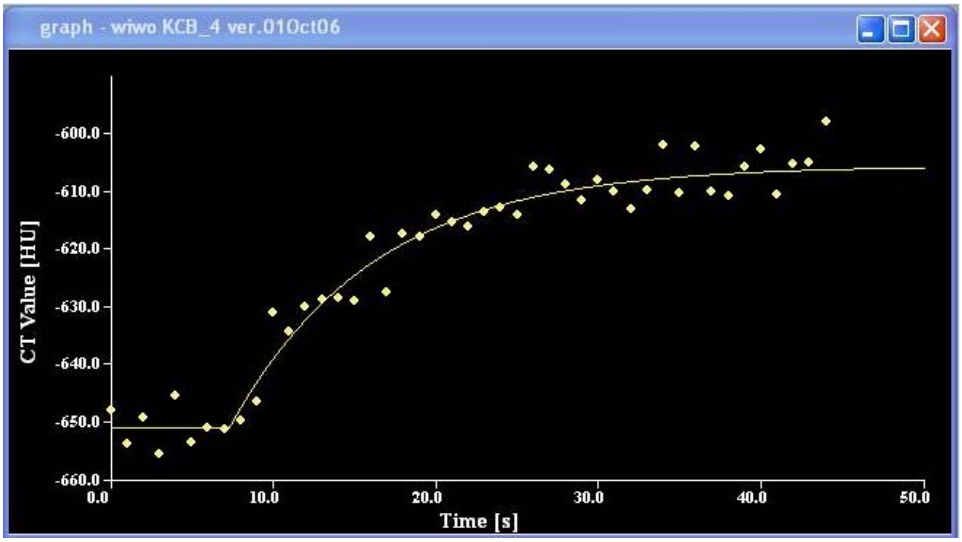

(b)

Figure 2.5: Time series data from Xe-CT study. (a) shows the Xe-CT image of the lungs, with the lung boundaries marked in blue and a rectangular region of interest in yellow. (b) shows the raw time series data for this region of interest (wash-in phase) and the associated exponential model fit.

this way. In [9], we measured the registration accuracy based on a small number of manually annotated landmarks which provide information about the registration quality at only a few manually selected locations at airway branches. While the airway branchpoints can be easily recognized by trained observer, the mean movement of the airway branchpoints may not represent the movement of parenchyma in other regions which have larger movement during respiration. It is our interest to know how the algorithm performs in the regions where large deformation appears, such as the regions near diaphragm (Figure 2.6).

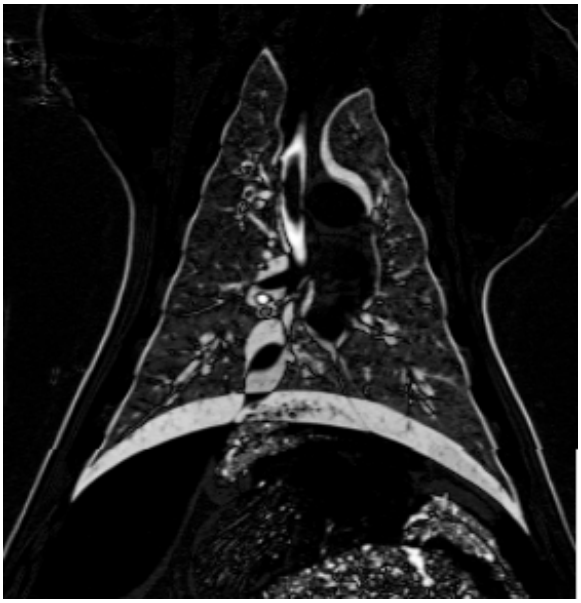

Figure 2.6: An example of image intensity difference before registration which depicts larger difference near the diaphragm than other regions.

Semi-Automatic Reference Standard An automatic landmark detection algorithm [10] was applied to find and match the landmarks across the static scans and the dynamic scans. The algorithm automatically detects "distinctive" points in the fixed image as the landmarks based on a distinctiveness value $D(p)$. Around each point p, 45 points, $q_1 ... q_{45}$ are uniformly distributed on a spherical surface with a radius of 8 voxels. A region of interest $ROI(q_i)$ is compared with the corresponding region of interest $ROI(p)$ around the original point p. $D(p)$ is calculated as:

$$D(p) = \frac{G(p)}{\max_j(G(p_j))} \sum_{i=1}^{45} \frac{\text{Diff}(ROI(p), ROI(q_i))}{45} \tag{2.4}$$

where $G(p)$ is the gradient value of point $p(x, y, z)$, j is the total number of the landmarks we intend to have and $\text{Diff}(ROI(p), ROI(q_i))$ is the average difference of the voxel intensities in the two ROIs.

Figure 2.7 shows an example projection view of all landmarks generated by the algorithm for a scan.

A semi-automatic system [10] is then applied to guide the observer to find the landmarks in the fixed image with their corresponding voxels in the moving image. Each landmark-pair manually annotated by the observer is added to a thin-plate-spline to warp the moving image. The system utilize the warped image to estimate where the anatomic match will be located for a new landmark point presented to the observer, therefore the observer can start the matching from a system estimated location. Thus, as the warped image becomes more accurate by the new added landmarks, the task of the observer and becomes easy. The system will calculate

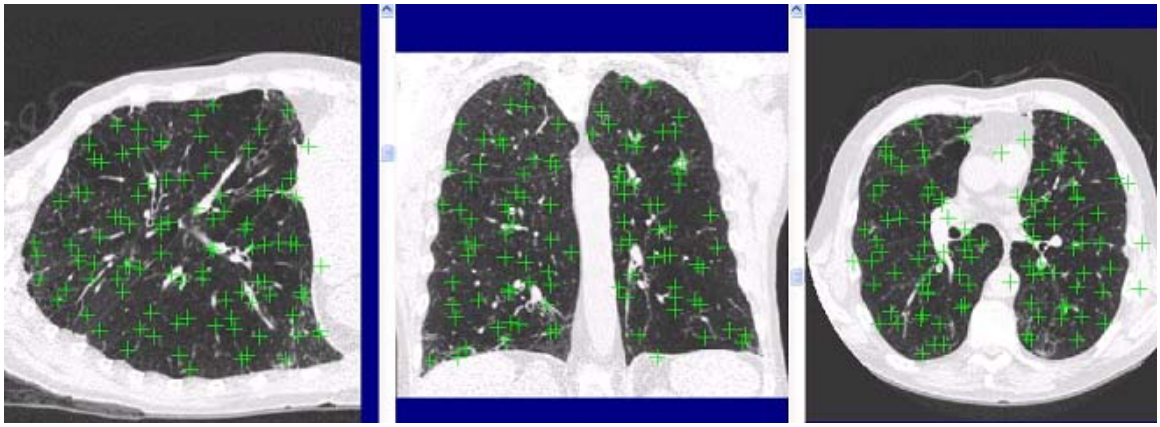

Figure 2.7: An example projection view of all landmarks generated by the algorithm for a scan. Figure from Murphy et al. [10].

the automatic point correspondence for the rest of the landmarks if the user has successfully marked 30 landmarks fully manually and the computer has predicted at least 10 correspondences in a row correctly. Screen shots from the system are shown in Figure 2.8.

For each animal, after 200 anatomic landmarks are identified in the static scan $P10$ and dynamic scan $T0$, the observer marked the locations of the voxels corresponding to the anatomic locations of the landmarks in the rest static or dynamic scans. For each landmark, the actual landmark position was compared to the registration-derived estimate of landmark position and the error was calculated.

2.2.6 Comparison between Estimates from Registration and sV

Comparison between Estimates of Lung Expansion from Dynamic Scans and sV To compare the Jacobian values with the sV, we must identify correspond-

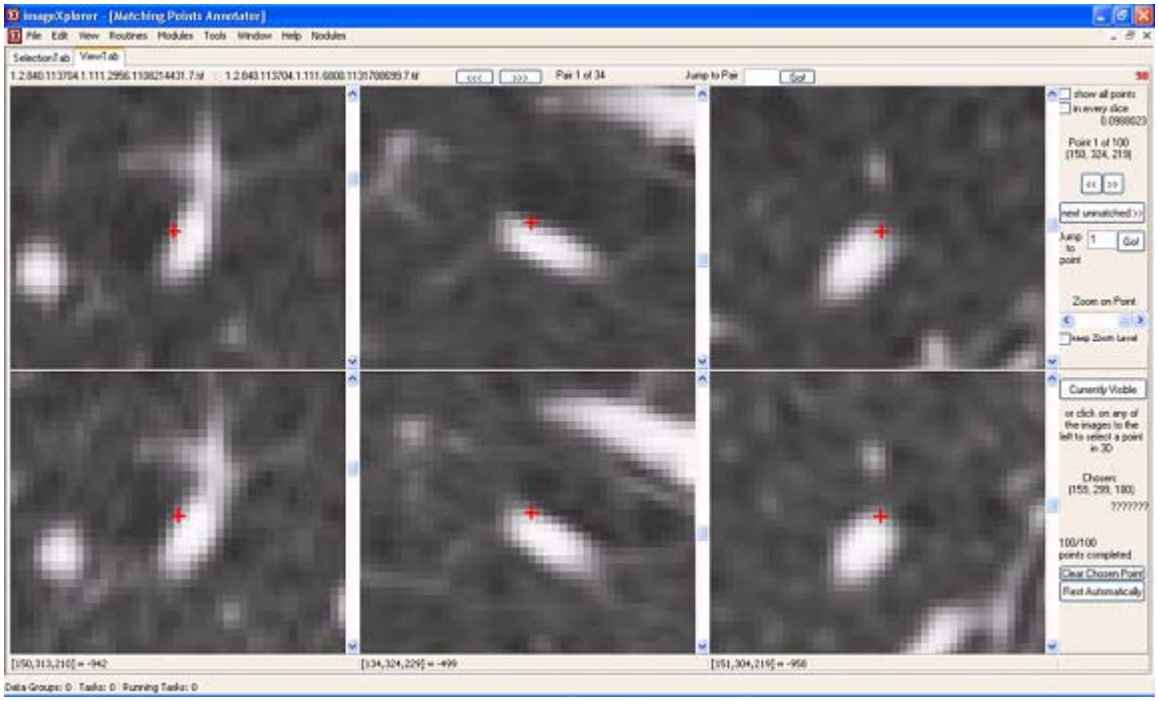

Figure 2.8: A screen shot of the software system used to semi-automatically match hundreds of landmarks. Figure from Murphy et al. [10].

ing regions in the two images. The Xe-CT has only twelve slices of axial coverage and the data sets are acquired in rigid alignment as described in Section 2.2.1, so we register the twelve-slice Xe-CT data to the $T0$ whole-volume retrospectively reconstructed dynamic CT data using rigid affine registration as shown in Figure 2.9. We subdivide the Xe-CT data into around 30 slabs along the y (ventral–dorsal) axis. We track the deformation of each slab across the sequence of volume images (i.e., from $T0$ to $T1$, $T1$ to $T2$ and etc.) and compare the average Jacobian within each slab to the corresponding average sV measurement in the Xe-CT images in the manner of correlation coefficient by linear regression.

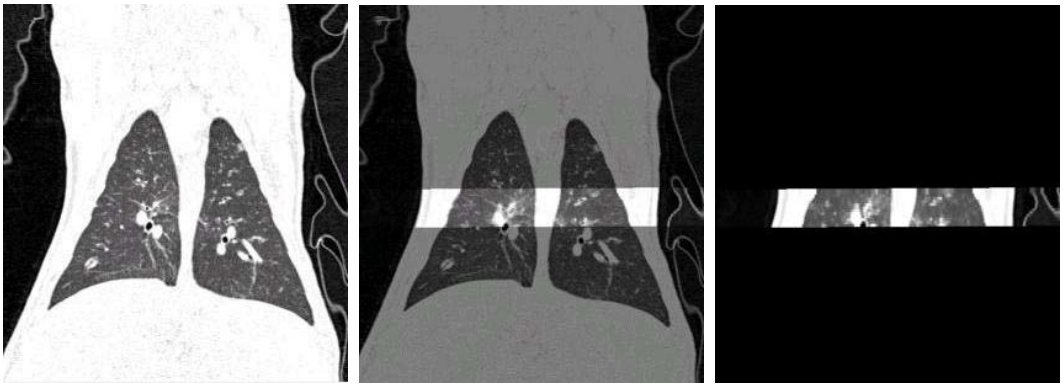

(a) (b) (c)

Figure 2.9: Example of the result of affine registration between Xe-CT data and dynamic respiratory-gated CT data. (a) $T0$ whole-volume dynamic respiratory-gated CT data. (b) Fused image. (c) Deformed first breath of the Xe-CT data.

Comparison between Estimates of Lung Expansion from Static Scans and sV Similarly, we first register the twelve-slice Xe-CT data to the $P10$ whole-volume breath-hold static CT data using same rigid affine registration. The lung region corresponding to the Xe-CT image in the static scan is divided into slabs and the motion of each slab can be tracked using resulting displacement fields. Then the average Jacobian in each slab is compared with the average sV. The correlation coefficients between the two estimates are calculated by linear regression.

It is worth noticing that because of the different data acquisition methods of the dynamic scans, static scans and Xe-CT data, the correlation coefficient may be affected by different breathing patterns. For example, the Xe-CT data and the dynamic scans are all acquired when the animals are during tidal breathing while the static data is acquired at discrete breath-hold pressures.

2.3 Results

2.3.1 Registration Accuracy

In our study, 200 landmarks were automatically generated by the algorithm described in Section 2.2.5. Figure 2.10(a) and 2.10(b) show the projection of the automatically-generated landmark locations onto coronal and sagittal slices for one animal. This figure shows that landmarks are distributed widely inside the lung.

Figure 2.11 shows the landmark error across eight phase change pairs and three pressure change pairs. Overall the registration accuracy is on the order of 2 mm, except for the abnormally large landmark errors in pressure change pair $P10$ to $P15$ for animal AS70078. After further inspection, we attribute this to the poor image contrast near dorsal region in this image pair due to atelectasis and edema.

2.3.2 Lung Expansion and Xe-CT Estimates of sV

Figure 2.12 shows the correlation coefficients r^2 from the linear regression of average Jacobian and sV for each phase change pair and pressure change pair for each animal. The phase change pair $T2$ to $T3$ shows the highest average correlation $r^2 = 0.85$, and the pressure change pair $P20$ to $P25$ shows the highest average correlation $r^2 = 0.84$. Figure 2.13 shows the different phases change pair for different regions of the lung when largest expansion and contraction occur. Most of the lung regions will have the largest expansion at the middle phase ($T1$ to $T2$ or 25% to 50% of the inspiration duration) and the largest contraction at the beginning phase ($T4$ to $T5$ or 100% to 75% of the expiration duration). Compared with static acquisition, dynamic acquisition can provide temporal mechanical changes in the respiratory cycle

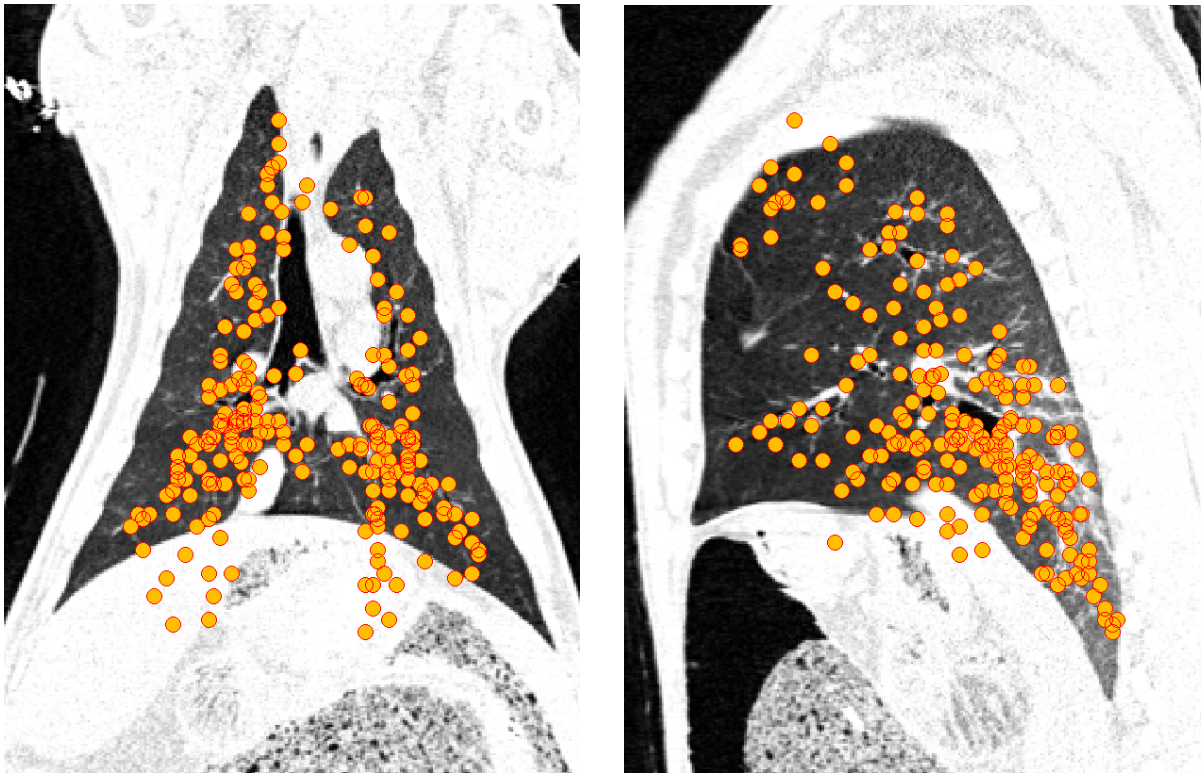

(a) (b)

Figure 2.10: Automatically-generated landmark locations projected onto (a) a coronal slice and (b) a sagittal slice for one animal at T0 breathing phase. Note that all the landmarks are inside of lung in 3D view.

between different phases.

2.4 Discussion

From Section 2.3.2, we see that the registration-based estimates of regional lung expansion from the two imaging protocols show equally high correlation to the Xe-CT sV. Since the Xe-CT data is collected over several breaths during tidal breathing, it is reasonable to expect that the Jacobian calculated from the dynamic scans would more closely reflect the ventilation patterns measured by the Xe-CT. However,

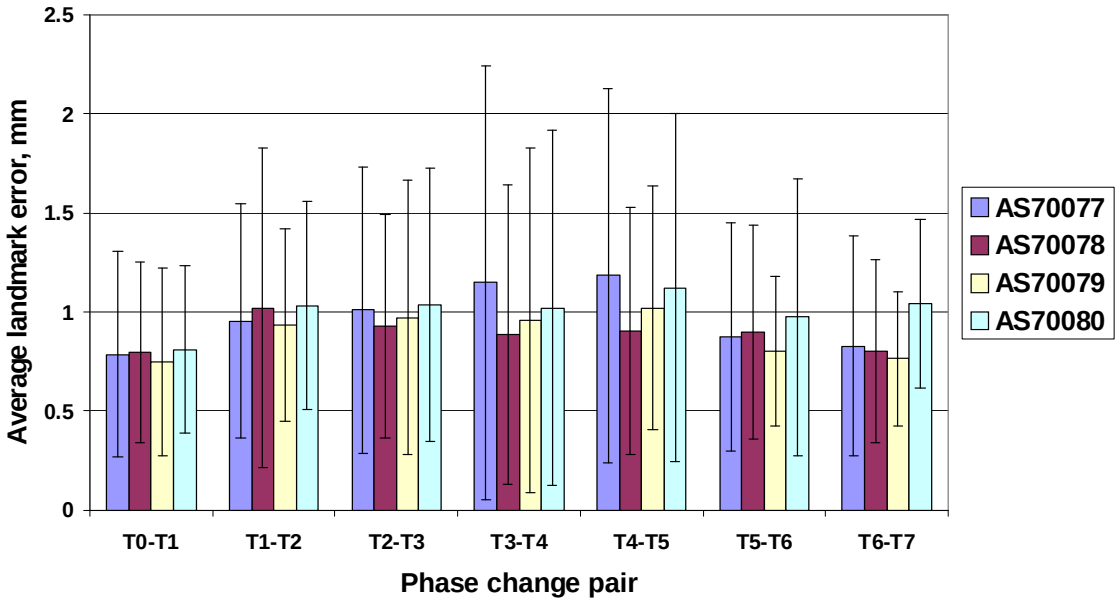

(a)

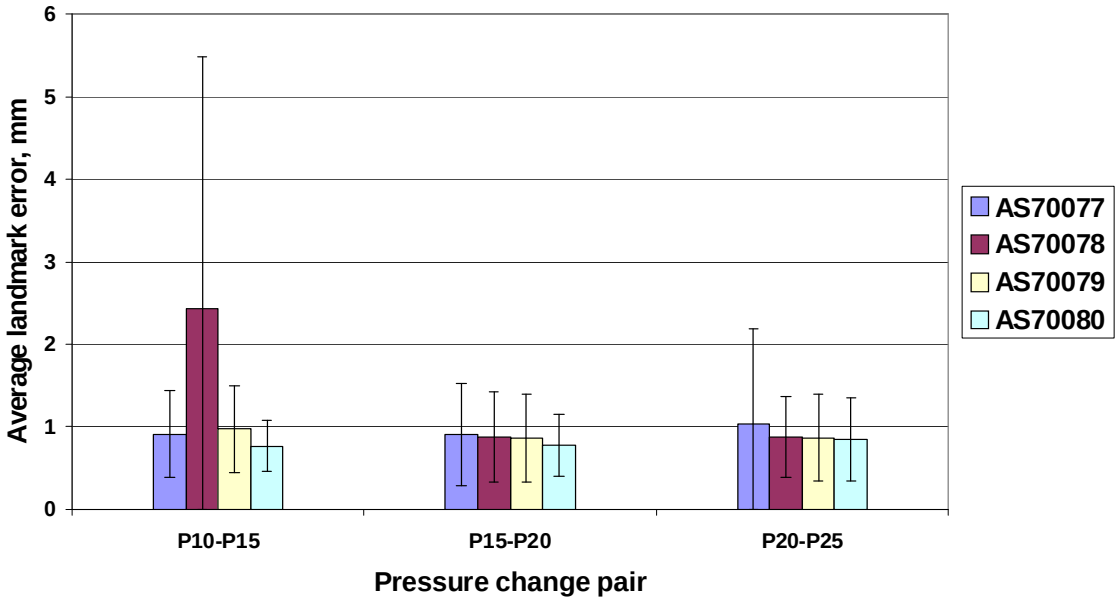

(b)

Figure 2.11: Registration accuracy from semi-automatic reference standard (200 landmarks) by mean ± standard deviation of landmark errors for each animal for each (a) phase change pair and (b) pressure change pair.

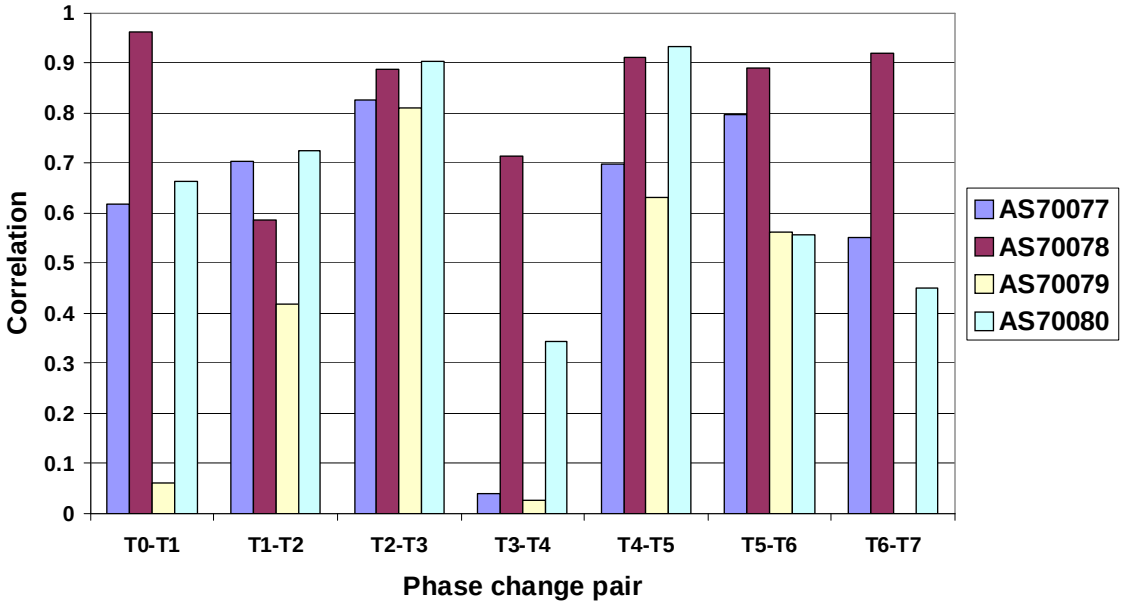

(a)

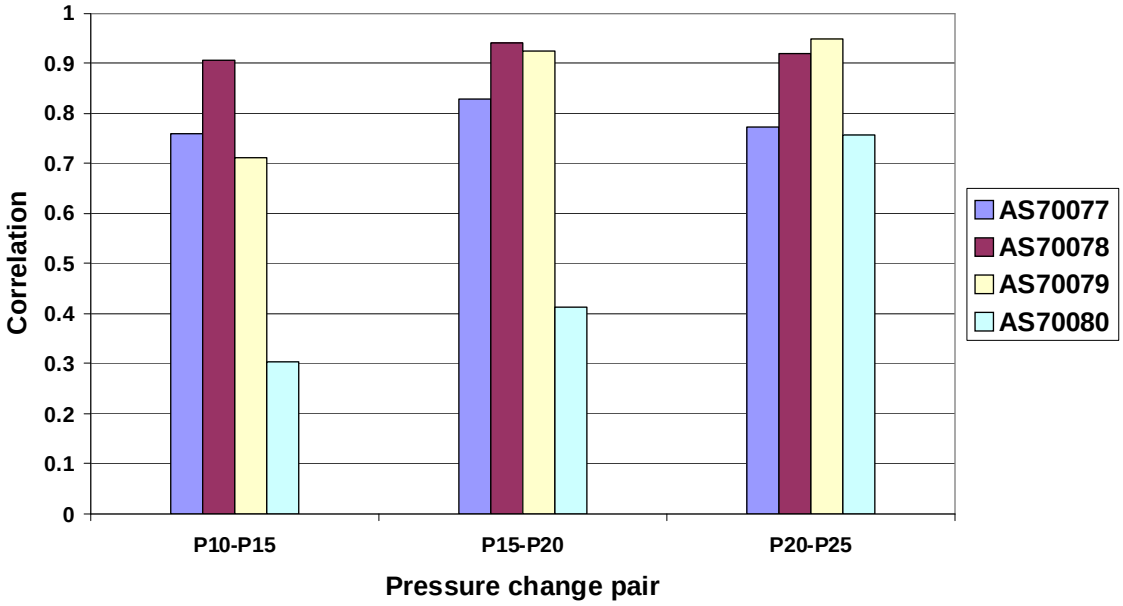

(b)

Figure 2.12: Correlation coefficients r^2 from the linear regression of average Jacobian and sV for each animal for each for each (a) phase change pair and (b) pressure change pair.

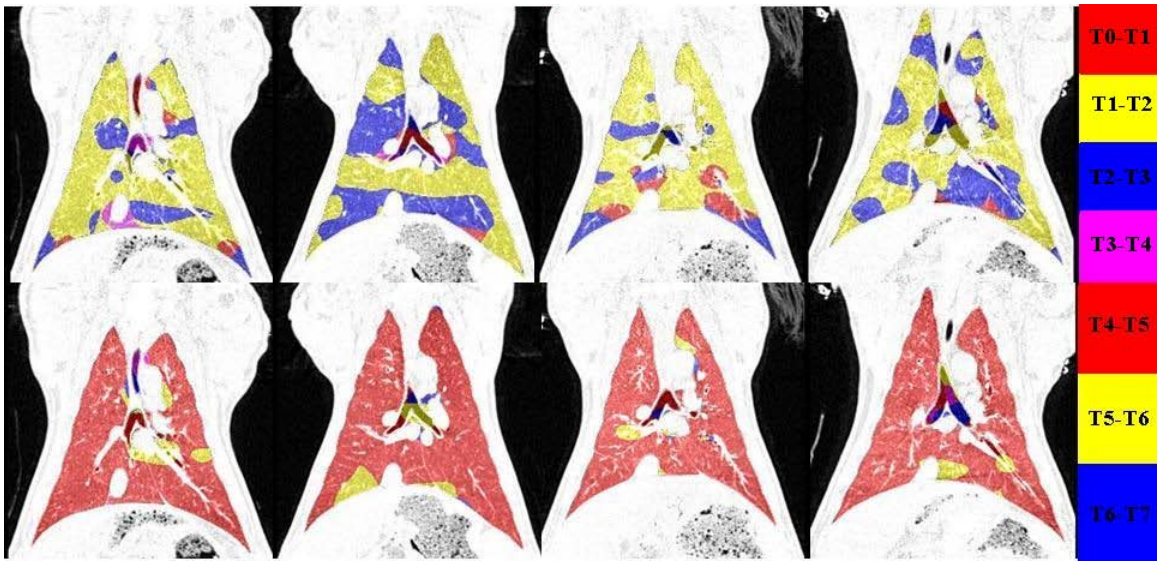

(a)

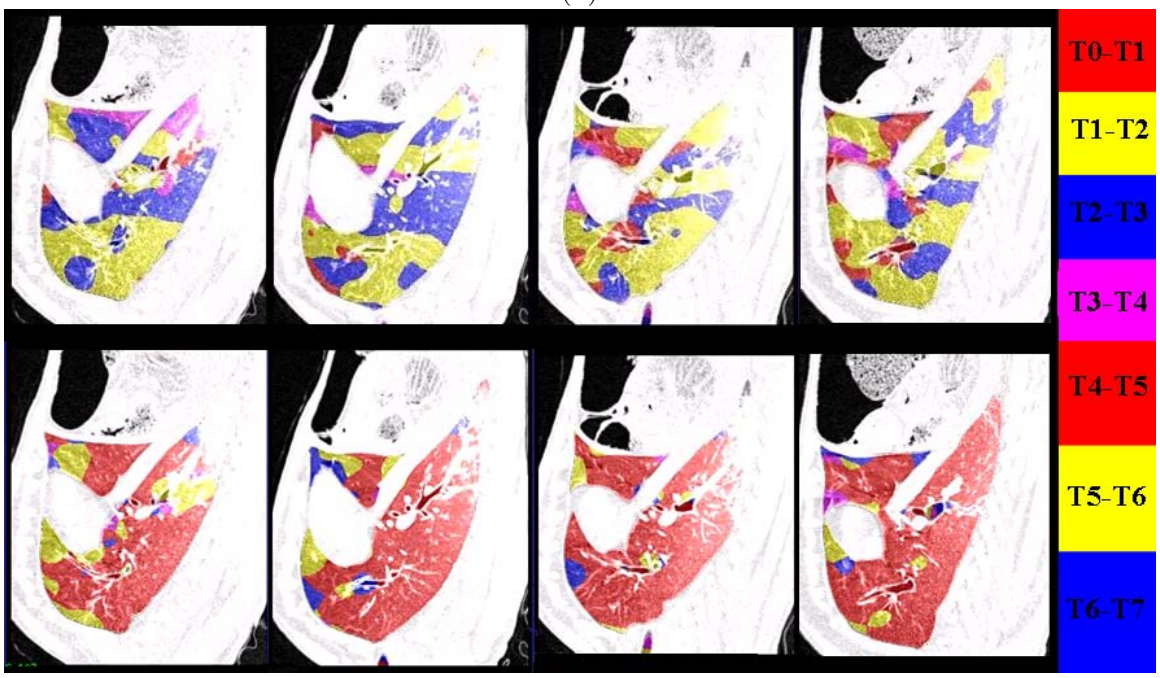

(b)

Figure 2.13: Color coded image showing (a) coronal view and (b) sagittal view of the the phase change pair when the largest expansion occurs during inspiration (first row) and the largest contraction occurs during expiration (second row). From left to right: Sheep AS70077, AS70078, AS70079 and AS70080.

the results do not support these expectations. One explanation for the close match between the Jacobian calculated from the static scans and the sV is that some of the pressure steps used in the static acquisition are close to the mouth pressure observed during tidal breathing. Further investigation of the pressure measurement for the dynamic scans during the tidal breathing is needed. Even though the compari-

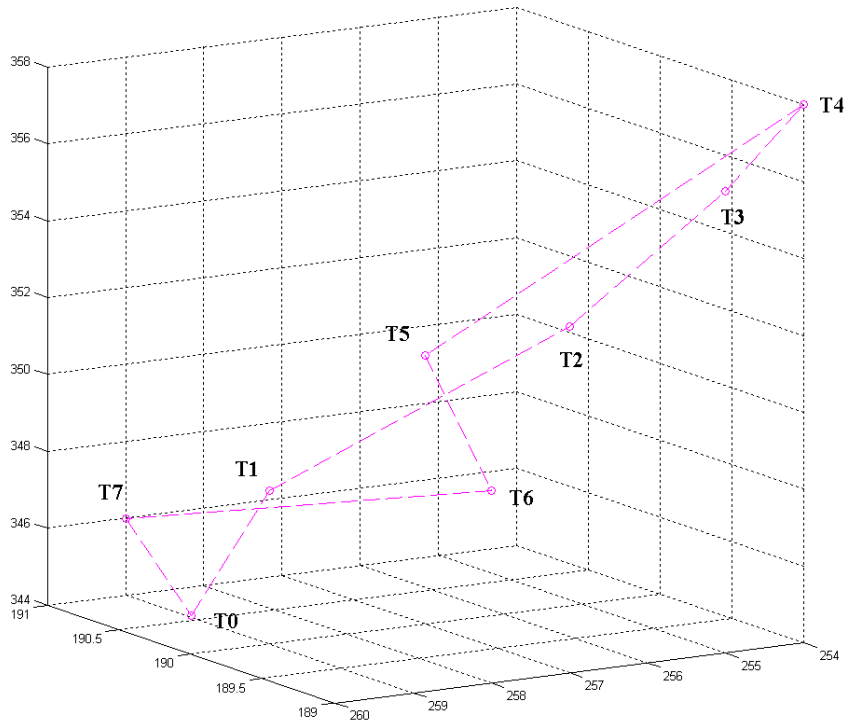

Figure 2.14: An example of the motion hysteresis of a point near diaphragm of sheep AS70078 during tidal breathing.

son of the Jacobian to the sV shows equally good correlations for both the dynamic scans and the static scans, the true dynamics of the respiratory system are probably better revealed using dynamic scans acquired across free breathing since the moving

lungs may exhibit viscoelastic behavior. The color-coded regions in Figure 2.13 show that the lung does not expand or contract uniformly along the phases. For example, some regions along the diaphragm in Figure 2.13(a) have larger expansion in the later phases than the earlier phase. It would be interesting to determine if the regions of maximal expansion vary with body position and level of inspiration. The motion hysteresis, which is patient specific, can be revealed by tracking individual points using the deformation field across dynamic scans as shown in Figure 2.14. On the other hand, the static scans have better image contrast, improved spatial resolution, and deliver relatively lower radiation dose compared to the dynamic scans. Dynamic imaging requires regular and repeatable breathing patterns, so the subject must be trained to breath properly before images are acquired. In addition, the subject will receive more radiation dose using the dynamic acquisition than from the single pair of static breath-hold images.

In Section 2.2.2, we mentioned that the registration algorithm is based on a linear elastic model. Because of the assumption of linear elasticity, the registration based on the elastic model is only applicable to small deformations and may fail when recovering large image differences. Though in Section 2.2.2 we have shown small average landmark errors (less than 2 mm), it is our interest to know the relationship between the landmark errors and the volume difference in the input images or in other words, the pressure change in our experiments. Since our objective is to translate our methods for use with humans, it is necessary to understand the limitations of the registration algorithm through more experiments. In many clinical exams, the

patient is scanned at two different lung volumes - near functional residual capacity (FRC) and near total lung capacity (TLC). Because of the large anatomic differences between these two lung configurations, it is unclear whether the basic assumptions of the linear elastic model are appropriate, or if more sophisticated modeling is needed.

We have compared registration-based regional lung expansion estimates to Xe-CT derived measures of regional ventilation to validate our measurements. The correlation to the Xe-CT sV is equally high in the Jacobian calculated from the dynamic retrospectively reconstructed scans ($r^2 = 0.85$) and from the static breath-hold scans ($r^2 = 0.84$). Our semi-automatic reference standard to quantitatively evaluate the accuracy of 3D image registration shows that the average registration error is on the order of 2 mm. Though Xe-CT based regional lung function assessment has the advantage of directly measuring specific ventilation, it requires the use of expensive xenon gas which has a strong anesthetic effect that must be carefully monitored. Xe-CT image acquisition also requires imaging across several respiratory cycles to observe the gas wash-in or wash-out in order to measure regional ventilation. In contrast, registration-based estimates of lung expansion may provide valuable lung function information from a single pair of respiratory-gated CT images, or from a dynamic image sequence retrospectively reconstructed across changing respiratory phase. As these new methods are extended to use in humans, they may provide valuable new tools for studying the normal and diseased lung.

CHAPTER 3
EVALUATION OF LOBAR BIOMECHANICS DURING RESPIRATION

3.1 Introduction

As introduced in Chapter 1, the human lungs are divided into five independent compartments called lobes as shown in Figure 3.1. Here we briefly review the anatomy for lungs. Each lung is surrounded by a closed sac, the pleural sac, consisting of a thin sheet of cells called pleura. The relationship between a lung and its pleural sac can be visualized by imagining what happens when you push a fist into a fluid-filled balloon. The fist becomes coated by one surface of the balloon. The opposite surfaces lie close together but are separated by a thin layer of fluid. Unlike the balloons and fist, however, the plural surface coating the lung (visceral pleural) is firmly attached to the lung by connective tissue. Similarly, the outer layer (the parietal pleura) is attached to and lines the interior thoracic wall and diaphragm. The visceral pleural also lines the surface of lobes. Figure 3.2 shows the spatial locations of the fissures and lobes. A lobar fissure is a thin space (approximately 0.5 mm depending on volume of pleural fluid) separating the lung lobes. The left lung is divided into the left upper (LUL) and left lower (LLL) lobes, separated by the oblique fissure. The right lung is partitioned into the right upper lobe, middle lobe, and the lower lobe, separated by the oblique and horizontal fissures. The branching patterns of the bronchial and vascular trees also follow the lobar structure of the lung.

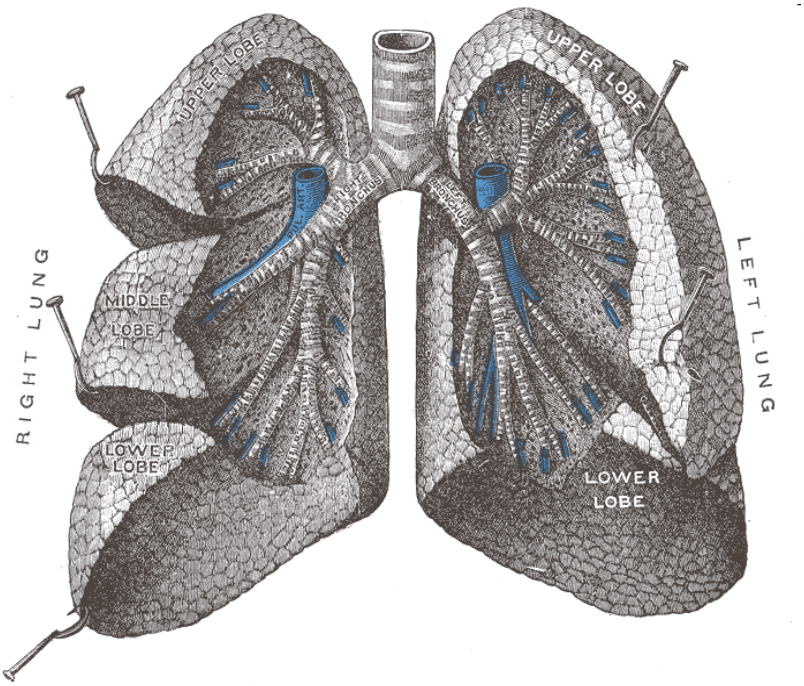

Figure 3.1: Drawing of human lungs cut open. Figure from [11].

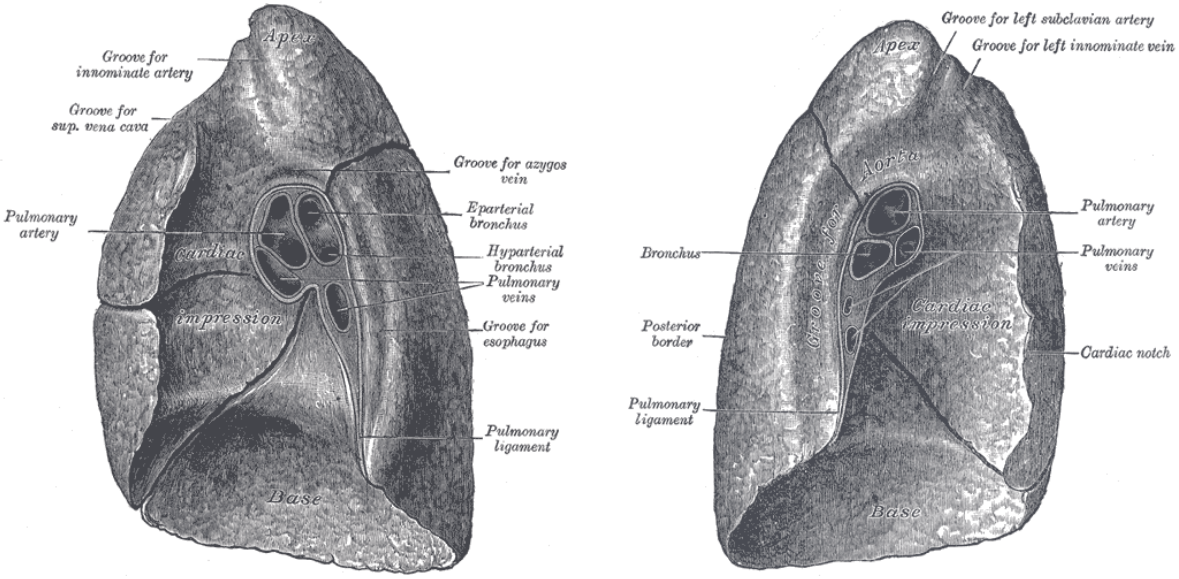

(a) (b)

Figure 3.2: Drawing of the mediastinal surface of (a) right lung and (b) left lung. Figure from [11].

Regional function and biomechanics depend on the material properties of the lung parenchyma and the complex interaction between the lobes, diaphragm, and chest wall. Hubmayr et al. [74] have used embedded metal markers and X-ray projection images to study regional lung mechanics. Recently, image registration has been used to assess regional lung function and tissue biomechanics using multiple 3D images at different lung volumes by CT [29, 25, 9] and MRI [27]. Although those results show regional changes in lung function and mechanics, they do not explicitly account for the interaction between the lung lobes. It is believed that during respiration the lobes move relative to each other (sliding and rotation), and this motion may provide a means to reduce the lung parenchymal distortion and avoid regions of high local stress [74]. In addition, understanding of how lobes slip relative to one another is of importance to the understanding of how the lung accommodates chest wall shape changes while minimizing effects on regional distribution of ventilation.

In this chapter, we investigate lung biomechanics using a lobe-by-lobe registration technique. Our approach explicitly accounts for the registration displacement field discontinuity at the fissure (due to lobar sliding), and should provide more accurate image registration near the fissure and, as a result, better biomechanical measurements. We measure lobar sliding by evaluating the relative displacement on both sides of the fissure. We compare whole-lung-based registration accuracy to lobe-by-lobe registration accuracy using vessel landmarks.

3.2 Materials and Methods

3.2.1 Method Overview

Our goal is to measure lobar sliding by looking at the discontinuity of displacement filed in the line profile perpendicular to the fissure surface. Figure 3.3 shows a block diagram of the entire process. Two image data sets are used in the processing. A functional residual capacity (FRC) scan and a total lung capacity (TLC) scan were acquired for each subject. A automatic lobe segmentation algorithm is applied to get masked lobe images $\mathrm{FRC_{Lobe}}$ and $\mathrm{TLC_{Lobe}}$. To compare the difference of the registration from traditional lung-by-lung based approach, automatic lung segmentation algorithm is also applied to $\mathrm{FRC_{CT}}$ and $\mathrm{TLC_{CT}}$ to get the masked lung images $\mathrm{FRC_{Lung}}$ and $\mathrm{TLC_{Lung}}$.

Nonlinear image registration is used to define transformations on these data sets. Transformation T1 consists transformations defined between each lobe, and are recombined to the lungs. Transformations T2 is defined between each lung. These two transformations are used to assess local lobar sliding ($\mathrm{SD_{Fissure}}$) on the fissure surface via the sliding calculation of the transformations.

3.2.2 Data Acquisition

All data were gathered under a protocol approved by our institutional review board. Three pairs of volumetric CT data sets from three normal human subjects were used in this study. Each image pair was acquired with a Siemens Sensation 64 multi-detector row CT scanner (Forchheim, Germany) during breath-holds near functional residual capacity (FRC) and total lung capacity (TLC) in the same scanning session.

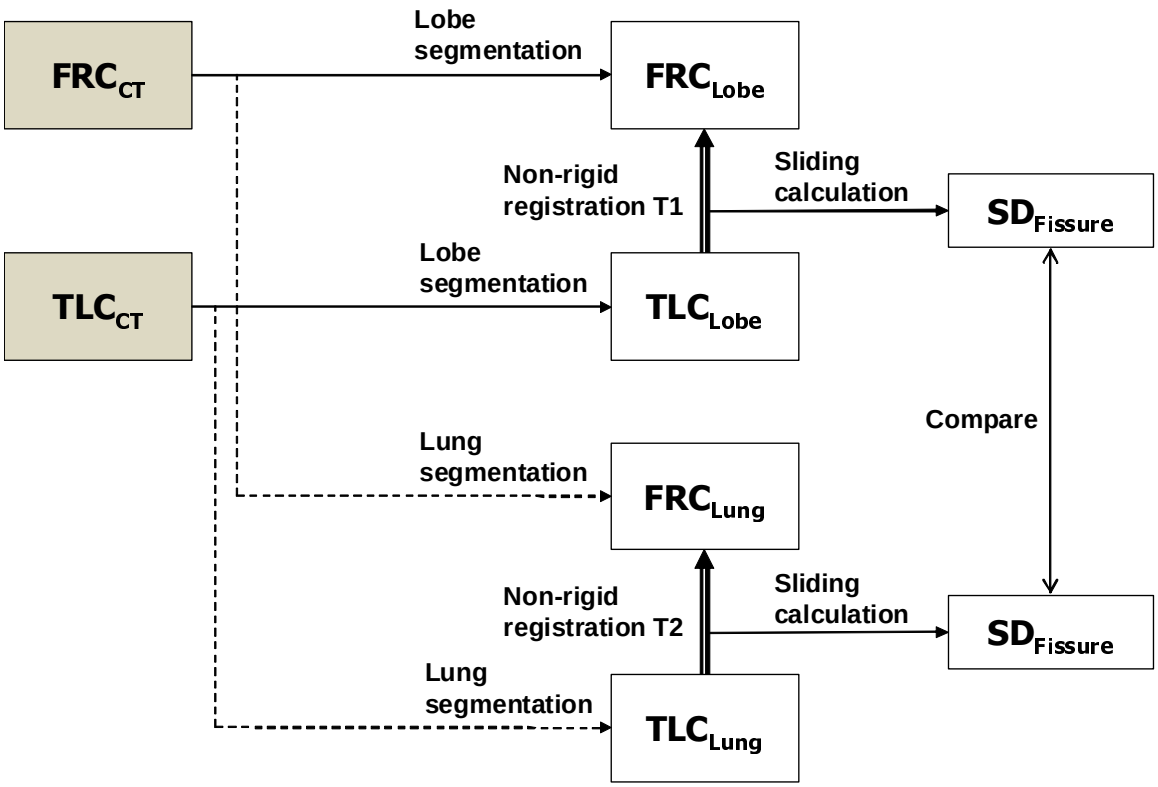

Figure 3.3: Figure shows the two images (FRC_{CT} and TLC_{CT}) that are analyzed during the processing. A automatic lobe segmentation algorithm is applied to get masked lobe images FRC_{Lobe} and TLC_{Lobe}. To compare the difference of the registration from traditional lung-by-lung based approach, automatic lung segmentation algorithm is also applied to FRC_{CT} and TLC_{CT} to get the masked lung images FRC_{Lung} and TLC_{Lung}. Lobe-by-lobe transformation T1 and lung-by-lung T2 register total lung capacity (TLC) data to functional residual capacity (FRC) data and can be used to assess local lobar sliding ($SD_{Fissure}$) on the fissure surface via the sliding calculation of the transformations. (Shaded boxes indicate CT image data; white boxes indicated derived or calculated data; thick arrows indicate image registration transformations being calculated; thin solid lines and thin dashed lines indicate other operations.)

Each volumetric data set was acquired at a section spacing of 0.5 $\sim$ 0.6 mm and a reconstruction matrix of 512 $\times$ 512. In-plane pixel spacing is approximately 0.6 mm $\times$ 0.6 mm.

3.2.3 Automatic Lobe Segmentation

An automatic method is applied for lobe segmentation [75]. The initial estimation of the lobe begins with the segmentation of the lungs, airways, and vessels using the automatic methods reported in [72, 76, 77]. The branch point of the airway tree is labeled using the method reported in [76]. The original vessel segmentation algorithm has two steps: line filtering and vessel tracking, but only the first step is used for lobe segmentation since the vessel tracking step is time consuming and not necessary. The vessel distance map is then generated and combined with the original CT image to form a modified distance map so that the airways and vessels are forced to be the minima (basins) of the gray-level topography. In this modified distance map, the fissures are near the watersheds separating the basins. A watershed transform is then applied to the modified distance map and the resulting basins are merged according to the automatically selected markers from the anatomically labeled airway tree in the previous step. The second stage for fissure refinement is achieved by optimal surface detection. For the oblique fissure, firstly the region of interest (ROI) is extracted as a region of voxels with certain distance to the initial fissure segmentation. The ROI is then rotated and resampled to form the bounding-box for proper calculation of the optimal surface. Secondly, the ridgeness map is calculated and combined with the original image to define the cost function. The graph search algorithm is applied to

find the optimal surface for the oblique fissure. For refining the horizontal fissure, it is similar to the steps for refining the oblique fissure.

3.2.4 Image Registration

The CT scans at FRC and TLC are registered for each subject. The FRC–TLC image pairs show large lung volume change, large tissue deformation, and large voxel intensity changes. To account for these differences between the images during registration, we used a lung mass preserving registration method [50]. The method uses a similarity metric that estimates the local tissue and air fraction within the lung and minimizes the local tissue mass difference. This method has been shown to be effective at registering across large lung volume changes (such as FRC–TLC pairs) [50].

From the CT value of a given voxel, the tissue volume can be estimated as

$$V(\mathbf{x}) = \nu(\mathbf{x})\frac{I(\mathbf{x}) - HU_{air}}{HU_{tissue} - HU_{air}} = \nu(\mathbf{x})\gamma(I(\mathbf{x})), \tag{3.1}$$

where $\nu(\mathbf{x})$ denotes the volume and $I(\mathbf{x})$ is the intensity of a voxel at position $\mathbf{x}$. HU_{air} and HU_{tissue} refer to the intensity of air and tissue, respectively [78]. In this work, we assume that air is -1000 HU and tissue is 55 HU. $\gamma(I(\mathbf{x}))$ is introduced for notational simplicity.

Given (5.2), we can then define the similarity measure as the sum of squared

local tissue volume difference:

$$C = \sum_{\mathbf{x}\in\Omega} \left[V_r(\mathbf{x}) - V_f\left(T(\mathbf{x})\right)\right]^2 = \sum_{\mathbf{x}\in\Omega} \left[\nu_r(\mathbf{x})\gamma(I_r(\mathbf{x})) - \nu_f\left(T(\mathbf{x})\right)\gamma(I_f(\mathbf{x}))\right]^2, \quad (3.2)$$

where Ω denotes the overlapping lung regions in the two images, and $T(\mathbf{x})$ is the warping function. In this work, $T(\mathbf{x})$ is a cubic B-splines transform:

$$T(\mathbf{x}) = \mathbf{x} + \sum_{\mathbf{k}\subset K} \phi_{\mathbf{k}}\ \beta(\mathbf{x}), \quad (3.3)$$

where ϕ describes the displacements of the control nodes and $\beta(\mathbf{x})$ is a three-dimensional tensor product of basis functions of cubic B-Spline.

Given a warping function $T(\mathbf{x})$, $I_f(T(\mathbf{x}))$ can be interpolated from the moving image. $\nu_f(T(\mathbf{x}))$ can be calculated from the Jacobian $J(\mathbf{x})$ of the deformation as $\nu_f(T(\mathbf{x}) = J(\mathbf{x})\nu_r(\mathbf{x})$. Note that the Jacobian value must be positive here, which can be achieved by using displacement constraints on the control nodes.

3.2.5 Computational Setup

In this study, the lobe-by-lobe registration is used to investigate lobar sliding. Our current analysis is limited to the upper and lower lobes of the left lung, since the three lobes in the right lung will likely have more complicated interaction.

We start with the lobar segmentations of the TLC and FRC images as described in 3.2.3. After segmentation we match the TLC left upper lobe to the FRC left upper lobe, and the TLC left lower lobe to the FRC left lower lobe. After registration, the displacement fields are recombined into one left lung displacement field.

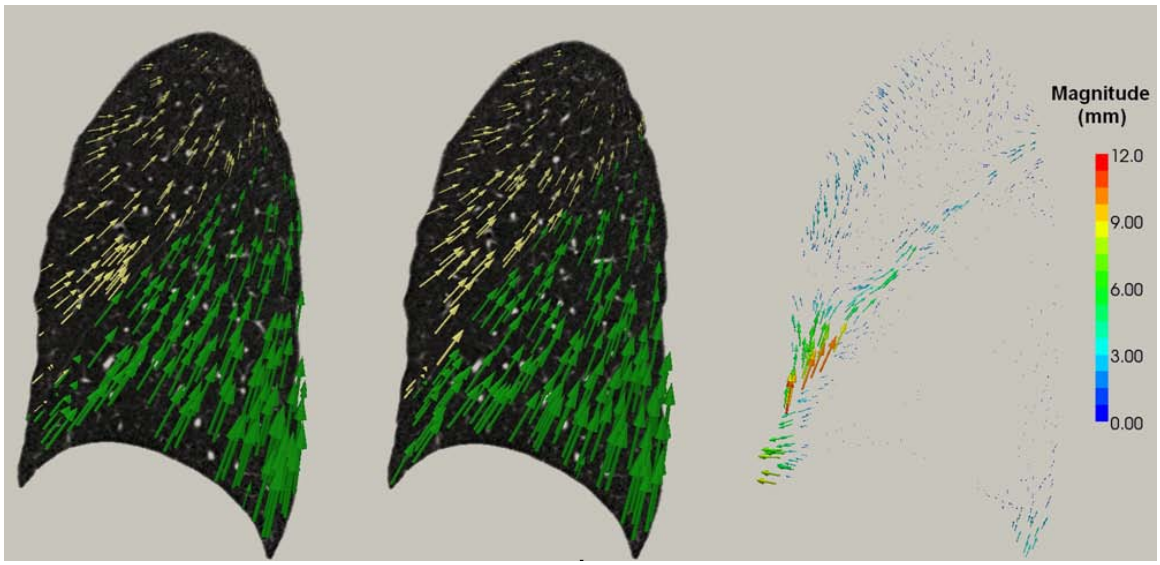

Figure 3.4: Comparison of displacement field between the lobe-by-lobe registration (left column) and the lung-by-lung registration (middle column) for the LUL (yellow) and LLL (green). The right column is the difference of the two displacement fields with the magnitude indicated by the color bar.

We also perform conventional lung-by-lung registration to match the TLC left lung to the FRC left lung, using the same registration algorithm.

Discontinuities of the displacement field along the fissure surface are indications of lobar sliding. Figure 3.4 shows the displacement fields generated by lobe-by-lobe and lung-by-lung registration methods for one subject. The figure shows a considerable difference between these methods along the fissure surface.

3.2.6 Assessment of Image Registration Accuracy

Vascular bifurcation points are used as landmarks to evaluate registration accuracy. An observer uses a landmark annotating system [10] to find corresponding landmarks in the FRC and TLC images. For each landmark, the actual landmark

position is compared to the registration-derived estimate of landmark position from the two registration methods and the landmark error is calculated.

3.2.7 Evaluation of Local Lobar Sliding

Once the lobe segmentations are obtained, the oblique fissure surface between LUL and LLL is extracted as a triangular mesh. The normal direction is then calculated at each vertex of the mesh. The sliding motion is quantified for each point along the fissure surface by looking at the discontinuity in the line profile perpendicular to the fissure surface as shown in Figure 3.6. On each side, the profile of tangent component of the displacement is fitted as a 3rd order polynomial function $\mathbf{d}$ of the distance to the fissure surface. The sliding distance $s(\mathbf{x})$ at fissure surface position $\mathbf{x}$ is then defined as

$$s(\mathbf{x}) = \| \mathbf{d}_0^+ - \mathbf{d}_0^- \|, \quad \mathbf{x} \in \mathcal{S}. \tag{3.4}$$

where $\mathbf{d}_0^+$ is the predicted value on the fissure surface from the polynomial function along the positive normal direction (we define the normal direction pointing the LUL as positive.) while $\mathbf{d}_0^-$ is the predicted value from the other side.

Figure 3.5 shows examples of the results from the process. The fissure surface is based on the lobe segmentation result (Figure 3.5(a)). It is extracted as a triangular mesh (Figure 3.5(b)) from the left upper lobe. The displacement profiles of tangent components along a line perpendicular to the fissure surface at different locations (red dots in Figure 3.5(c)) are compared for both the whole-lung-based and the lobe-based

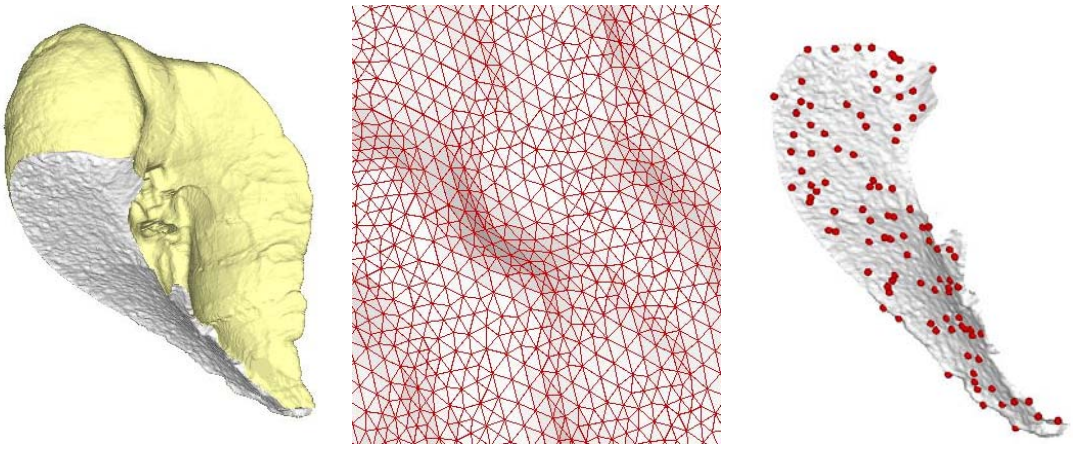

(a) (b) (c)

Figure 3.5: Examples of the results from the process. (a) Surface rendering of the segmentation of the left upper lobe. (b) The surface between the left upper lobe and left lower lobe is extracted as a triangular mesh. (c) The displacement profiles of tangent components along a line perpendicular to the fissure surface at different locations (red dots) are compared for both the whole-lung-based and the lobe-based registration methods.

registration methods.

3.3 Results

3.3.1 Registration Accuracy

For each lobe, 20 to 40 landmarks are identified. Table 3.1 shows the results of the landmark distance before and after registration for the lobe-based and whole-lung based registrations. The average landmark errors are 0.83 mm and 0.73 mm for whole-lung-based registration and lobe-based registration.

3.3.2 Local Lobar Sliding

The sliding distance at each fissure surface point was calculated to evaluate the local lobar sliding. A step length of 1 mm and 10 sample points were used along

Table 3.1: Comparison of registration accuracy between lobe-based and whole-lung-based registrations with distances in mm.

Subject	Lobe	Before Registration	Whole-lung-based Registration	Lobe-based registration
A	LUL	19.08 ± 8.25	0.99 ± 0.99	0.95 ± 0.81
	LLL	35.79 ± 12.69	0.94 ± 1.12	0.71 ± 0.41
B	LUL	15.09 ± 4.03	0.72 ± 0.81	0.57 ± 0.30
	LLL	38.33 ± 6.55	0.87 ± 0.48	0.75 ± 0.43
C	LUL	13.45 ± 6.59	0.78 ± 0.72	0.78 ± 0.83
	LLL	35.45 ± 10.76	0.68 ± 0.24	0.67 ± 0.30

the normal direction on each side of the surface. A surface point was not taken into consideration if any of its 20 sample points were outside the lobes. Figure 3.6 shows the displacement profile of the tangent component along a line perpendicular to the fissure surface at three different locations (near the apex, near the lingula and near the base) for the whole-lung-based (square) and the lobe-based (solid circle) methods. The results show increased sliding (larger discontinuity) in the more basal positions using the lobe-by-lobe analysis. However, these discontinuities are not apparent using the lung-by-lung analysis.

Figure 3.7 compares the estimated lobar sliding distances between two different registration methods. The whole-lung-based registration shows small sliding distance ($\leqslant$ 1 mm) because the transformation model enforces displacement field smoothness across the fissure, while the lobe-by-lobe registration method recovers the displacement field discontinuity along the fissure.

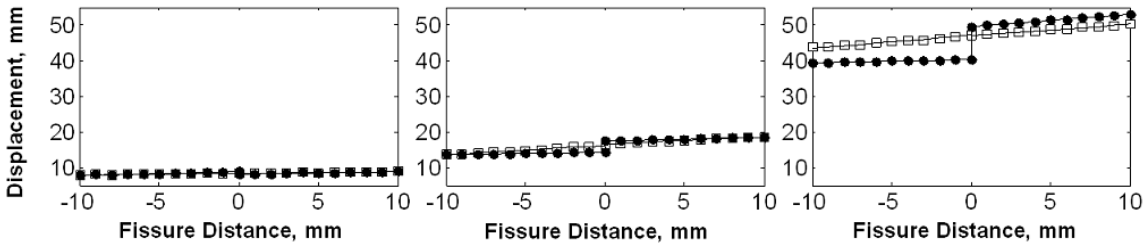

(a) Subject A with volume change = 3.2 Liters

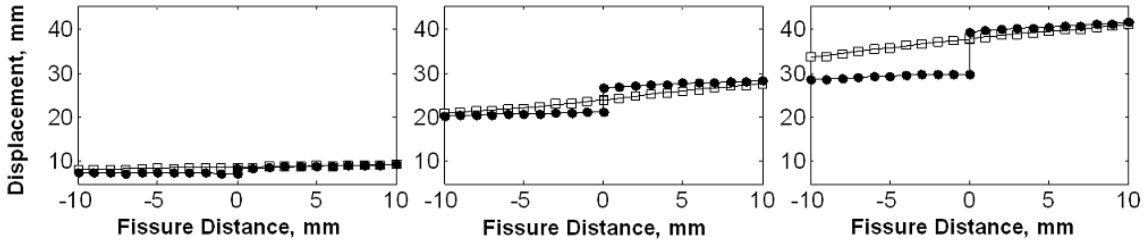

(b) Subject B with volume change = 2.3 Liters

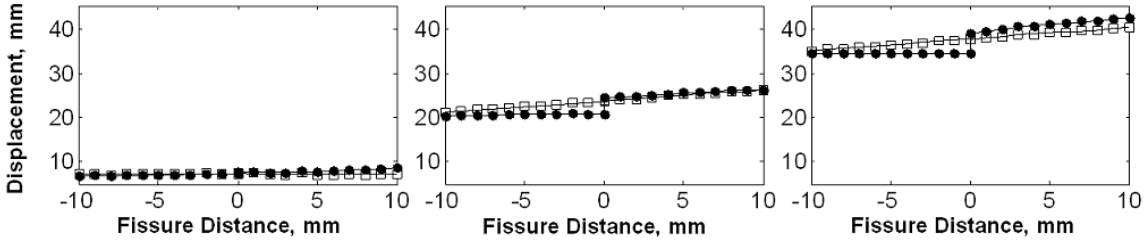

(c) Subject C with volume change = 2.4 Liters

Figure 3.6: Displacement profile of tangent components along a line perpendicular to the fissure surface at three different locations (left: near apex; middle: near lingula; and right: near base) for both the whole-lung-based (square) and the lobe-based (solid circle) methods.

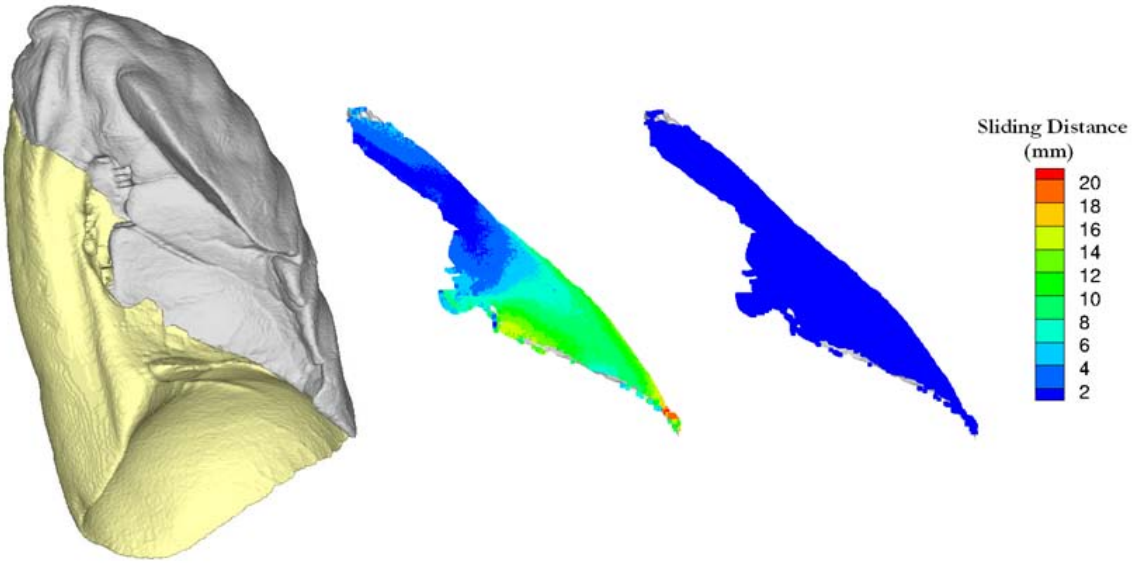

(a) Subject A with volume change = 3.2 Liters

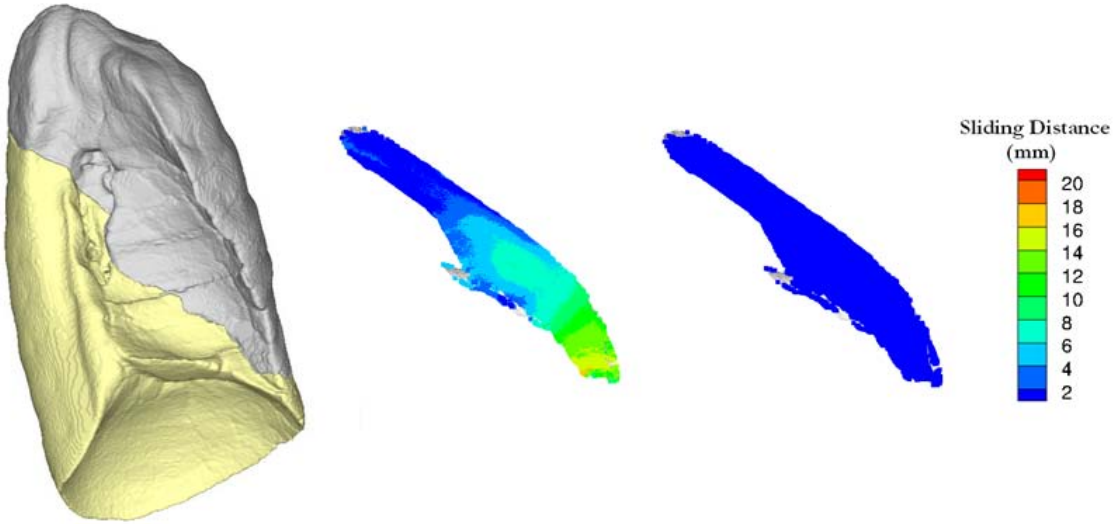

(b) Subject B with volume change = 2.3 Liters

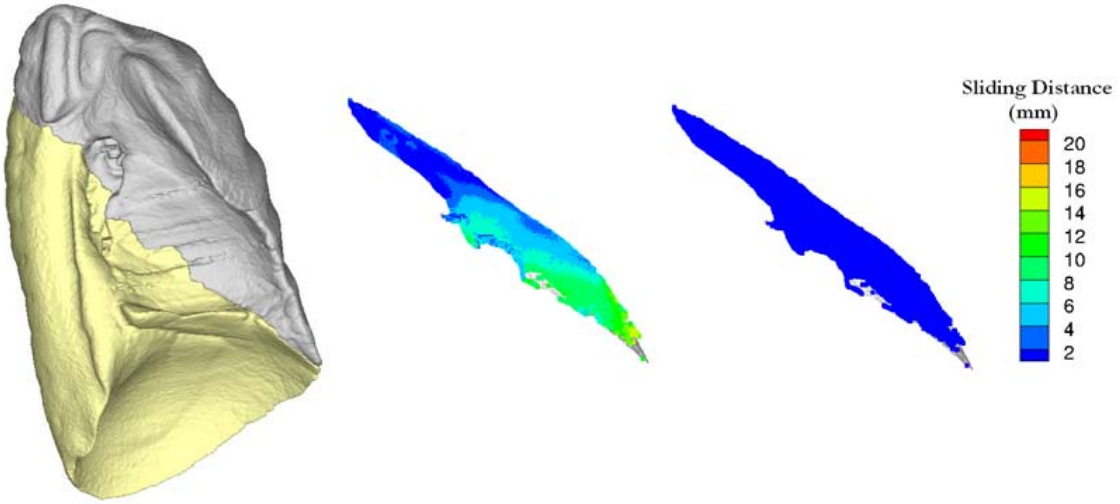

(c) Subject C with volume change = 2.4 Liters

Figure 3.7: The color-coded sliding distance map overlays on the fissure surface. Left most column is the surface rendering of LUL (gray) and the LLL (gold); second column shows the sliding distance from the lobe-based registration; and right most column shows the sliding distance from the whole-lung registration.

3.4 Discussion

We proposed a method to estimate local lobe sliding using lobe-by-lobe lung-mass-preserving registration. In addition, we compared the displacement field, the landmark error, and the sliding distance between the lobe-by-lobe registration and the lung-by-lung registration for the left lungs of three normal human subjects. We used major vascular bifurcation as landmarks. Thus, there are not large numbers of landmarks near fissures. As seen in Figure 3.4, both methods yield similar matching results in the center regions of the lobes while a considerable difference is observed in the vicinity of fissure. Thus, as seen in Table 3.1 there is not a very significant decrease in the overall landmark error while there are significant regional differences. Visual inspection of the displacement field shows considerable differences along the fissure. The manually annotated landmarks located in the major vessel bifurcations show that the lobe-by-lobe registration yields smaller average landmark error than the whole-lung-based registration. Moreover, the lung-by-lung registration is not able to capture the sliding between the lobes while the lobe-by-lobe registration shows the same superior-inferior gradient of sliding distance in all three cases. One possible explanation for this pattern is that the lungs contract and expand more at the diaphragm than at the apex and the LUL is more firmly anchored to the chest wall than LLL.

It would be ideal to validate our methods using physical phantoms or by results from other methods such as hyperpolarized helium (He^3) MRI [79]. However, a visualization inspection can help to validate by comparing the patterns of calculated

sliding distance with the known anatomy features of the lungs. Comparing the Figure 3.7 left most column with Figure 3.2(b), one can recognize the fissure surface goes across the main left lung branches of the bronchus, pulmonary arteries and pulmonary veins (the center location with three openings in Figure 3.2(b) and the hollow region in Figure 3.7). This region is located near the carina which serves the anchor point of the lungs. Therefore, the result of lower value of the sliding distance in this region from second column of Figure 3.7 is also confirmed by the local anatomy constraints.

In addition to evaluating lobar sliding, the lobe-by-lobe registration may yield more physiologically meaningful assessments of regional lung function and mechanics. Registration transformation functions that do not explicitly model the lobar fissure are not able to capture lobar sliding and thus experience more registration errors near the fissure. These findings may have implications in using registration to estimate lung function (specific volume change and lung expansion) and for tracking lung tissue and lung nodules, across the respiratory cycle. These methods can be directly extended to respiratory-gated CT of the lung, where CT data is reconstructed at multiple points across the respiratory cycle.

In conclusion, we have described a method to evaluate the local lobar sliding using a lobe-by-lobe lung-mass-preserving registration. Application of these methods may be useful for increasing our understanding of function and biomechanical behavior of the respiratory system.

CHAPTER 4
MEASUREMENT OF PULMONARY FUNCTION CHANGES FOLLOWING RADIATION THERAPY

4.1 Introduction

Radiation therapy (RT) for lung cancer is commonly limited to sub-therapeutic doses due to unintended toxicity to normal lung tissue. The radiation dose needed to control the tumor is well above that which causes toxicity to the normal lung tissue. Increase of tumor control could be achieved by delivering substantially higher radiation doses to the tumor [62], which is optimally achieved with RT delivery schemes that reduce toxicity. Reducing the frequency of occurrence and magnitude of normal lung function loss may benefit from treatment plans that incorporate relationships between regional and functional based lung information and the radiation dose.

The complex inter-relationship between RT treatment and the resultant changes in pulmonary function, or radiation induced lung toxicity, are poorly defined. Common toxicities include radiation pneumonitis, radiation fibrosis and ultimately altered respiratory capacity. Recent dose escalation studies of radiosurgery show a clear dose response relationship for primary lung tumors and that toxicity increased with dose [80, 81, 82, 83]. The relationship between radiation dose and normal lung tissue toxicity has been investigated since CT based planning became commonplace over a decade ago [84], yet the clear indicators for toxicity remain elusive [85, 86, 87, 88, 89]. It has been broadly accepted that radiation dose has a direct effect on treated lung tis-

sue and the lung in the treatment field shows radiographic fibrotic changes consistent with fibrosis [90]. It is largely assumed that this is the predominant and in some cases only significant effector of altered lung function despite known changes in inflammatory cells outside the treated area. Most current avoidance methods for lung tissue are solely based on direct dose-volume relationships with treated lung [84, 87, 91, 92], assuming lung tissue is homogeneous in its response to toxicity, irrespective of tissue location or underlying function [63]. Recently Yaremko et al. [63] proposed a method incorporating image registration derived estimate of ventilation to reduce normal lung irradiation. However, the radiation induced pulmonary function change may depend on the location, underlying function of that lung prior to radiations, radiation dose and other factors, especially in diseased lungs [93, 94]. No human studies have investigated the relationships between local lung function, spatial radiation dose distribution, and radiation induced lung function changes. However, rat studies have investigated changes in pulmonary function based on irradiation of different regions of rat lung. Luijk et al. showed structural changes in the lung were only correlated with changes in breathing rate when irradiating lateral lung regions (shielding the mediastinum) [95], and that greater lung damage was observed when irradiating the heart [96] while holding mean lung dose and volume of lung irradiated constant. They showed irradiation of larger volumes with smaller doses causes greater toxicity than treating smaller volumes with larger doses [97]. This is a result confirmed by others [98]. A common yet unspecified thread in the rat studies is that radiation treatments including the mediastinum caused a greater change in pul-

monary function. Establishing a quantitative measurement of the pulmonary function change before and after RT may greatly accelerate similar studies of the relationship between RT treatment and resultant changes in pulmonary function. Furthermore, this could translate into clinically relevant data for future treatment planning schemes that avoid increased functional injury to the lungs.

The pulmonary function test is a common clinical measurement tool to assess lung function, but only provides global information on the entire respiratory system. Regional pulmonary function can be measured using various imaging modalities. Nuclear medicine imaging, such as positron emission tomography (PET) and single photon emission CT (SPECT), can provide an assessment of local lung function [17, 16, 99]. Hyperpolarized noble gas MR imaging has been developed for functional imaging of pulmonary ventilation [18, 19, 20]. Xenon-enhanced CT (Xe-CT) can measure regional ventilation by observing the gas wash-in and wash-out rate on serial CT images [21, 23]. Image registration derived regional expansion can be used to indicate pulmonary function since there is a high correlation between regional lung expansion and regional ventilation. We previously demonstrated a correlation between the image registration based estimate of regional expansion (average Jacobian) and the Xe-CT derived specific ventilation [9] (linear regression, average $r^2 = 0.73$) in both static and dynamic image acquisition [100].

This chapter describes a technique using 4DCT, image registration, and lung biomechanical analysis to measure regional lung function before and after radiation therapy. The validity of the non-rigid image registration is evaluated by indepen-

dently assessing 120 vascular bifurcation points within the lung. Changes in regional lung function before and after RT are compared with the radiation dose distribution by transforming the pulmonary function maps into the same coordinate system as that of the computed dose distribution. This provides a framework to examine the relationship between lung function change, delivered dose, and treatment location within the lung.

4.2 Material and methods

4.2.1 Method Overview

Our goal is to measure changes in lung function by comparing regional lung volumes at end-inspiration and end-expiration before and after treatment. Figure 4.1 shows a block diagram of the entire process. Five image data sets are used in the processing. A "free breathing" pretreatment (FB_{PRE}) fan beam CT scan for treatment planning is acquired prior to RT using an ungated protocol with the subject breathing quietly during the scan. The FB_{PRE} image is used during the treatment planning process as the target data set; all radiation dose calculations and daily localization procedures are registered to the FB_{PRE} CT coordinate system. A 4DCT scan is also acquired prior to RT, and CT data sets are reconstructed at ten distinct phases of respiration. For this study we focus on the data sets from two of the phases, a volume at end expiration (EE_{PRE}) and a volume at end inspiration (EI_{PRE}). A second 4DCT study was acquired after RT and used in this study as "post" RT scans for analysis of post-RT changes (EE_{POST} and EI_{POST}).

Nonlinear image registration is used to define four transformations on these

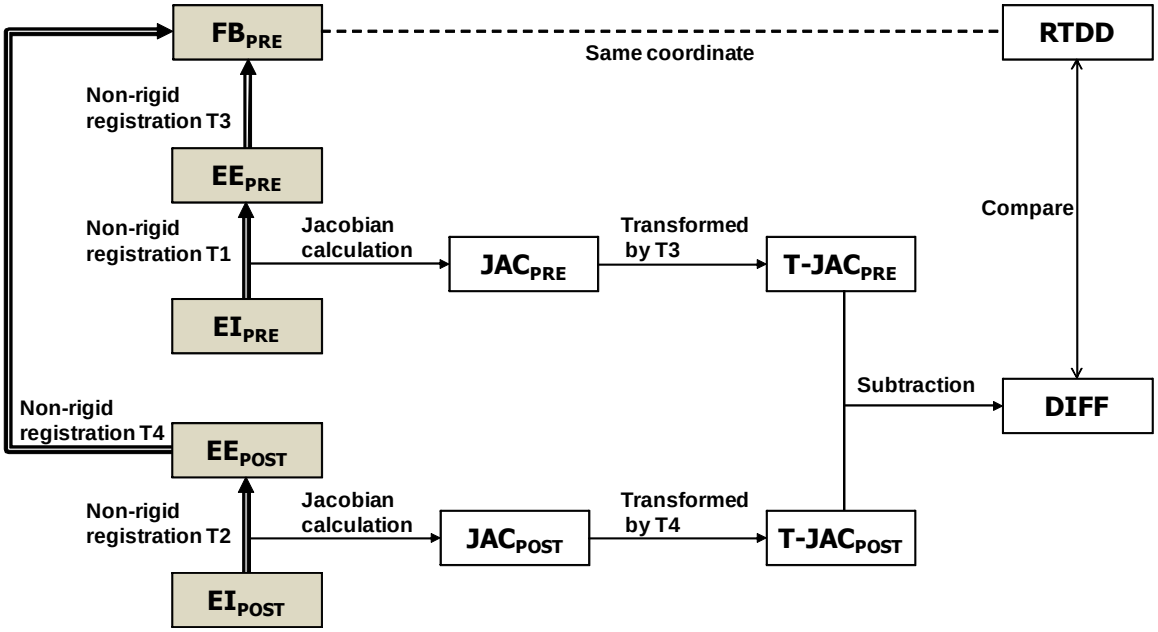

Figure 4.1: Figure shows the five images (EE_{PRE}, EI_{PRE}, EE_{POST}, EI_{POST}, and FB_{PRE}) that are analyzed during the processing. Transformations T1 and T2 register end inspiration (EI) to end expiration (EE) data and can be used to assess local lung function via the Jacobian (JAC) of the transformations. PRE and POST indicate before and after RT. The difference (DIFF) between the pre- and post-treatment Jacobian data can be be used to look for changes in pulmonary function. Transformations T3 and T4 map the Jacobian data into the coordinate system of the FB_{PRE} (planning CT) image, which allows direct comparison with the radiation treatment dose distribution (RTDD). FB_{PRE} and RTDD are in the same coordinate system since the FB_{PRE} scan is used to create the dose plan. (Shaded boxes indicate CT image data; white boxes indicated derived or calculated data; thick arrows indicate image registration transformations being calculated; thin solid lines indicate other operations.)

data sets. Table 4.1 summarizes these four transformations. Transformations T1 and T2 are defined between respiratory phase points on the 4DCT, and are used to estimate local lung expansion. Transformations T3 and T4 are used to convert the lung expansion data into same coordinate system as the RT dose map, and are used to compare changes in lung expansion with delivered RT dose.

Local lung function is assessed via the Jacobian (JAC) of the transformations T1 and T2 which register end inspiration (EI) to end expiration (EE) data. The Jacobian of the transformation T1 (JAC_{PRE}) describes the volume changes from EI_{PRE} to EE_{PRE} and the Jacobian of transformation T2 (JAC_{POST}) describes the volume changes from EI_{POST} to EE_{POST}. To compare these changes, the Jacobian of T1 and the Jacobian of T2 were mapped to the FB_{PRE} coordinate system with transformations T3 and T4, respectively. Additional details on the registration algorithms and other processing steps are given below.

4.2.2 Image Data Sets

All data sets were gathered under a protocol approved by the University of Iowa IRB. Data sets from two subjects with lung tumors treated in the Department of Radiation Oncology at the University of Iowa Hospitals and Clinics were analyzed retrospectively for this study: all scans were acquired as clinically indicated. Both subjects had two 4DCT studies - the first study was prior to the first course of RT and the second study followed delivery of RT. Both 4DCT studies included a contrast-enhanced free breathing CT scan used for RT treatment planning dose calculations. Prior to each 4DCT scan, the subject received respiratory training using a biofeedback

Table 4.1: Summary of image registrations performed to detect RT-induced changes in lung function. Names of images and transformations refer to those given in Figure 4.1.

Transformation Name	Image Transformed	Used To	Algorithm Used
T1	$EI_{PRE} \rightarrow EE_{PRE}$	Calculate pre-RT lung expansion map (Jacobian of T1)	SICLE [67]
T2	$EI_{POST} \rightarrow EE_{POST}$	Calculate post-RT lung expansion map (Jacobian of T2)	SICLE [67]
T3	$EE_{PRE} \rightarrow FB_{PRE}$	Transform pre-RT Jacobian into RT dose planning system coordinate system for comparison	SICLE [67]
T4	$EE_{POST} \rightarrow FB_{PRE}$	Transform post-RT Jacobian into RT dose planning system coordinate system for comparison	Elastix-NRP [101]

system (RESP@RATE, Intercure Ltd., Lod, Israel) to identify their nominal breathing rate. Musical cues were used to pace respiration during imaging employing a technique developed at our institution and shown to have high success and compliance [102].

For subject A, the EE_{POST} and EI_{POST} data were acquired after a complete course of RT treatments (approximately one year after the FB_{PRE} scan and 48 Gy in 16 Gy/fx for 3 fractions). For subject B, the EE_{POST} and EI_{POST} data were acquired after 13 of 37 fractions (23.4 Gy in 1.8 Gy/fx out of 66.6 Gy total), approximately one month later after the FB_{PRE} scan. These patient scans were selected for analysis because they contained 4DCT data sets both pre-RT and post-RT, with a known planned dose distribution. For subject A, the tumor was a solitary mass (~ 4 cm^3) located in the left lung and the right lung was disease-free. For subject B, the tumor

was located in the right lung as well as the mediastinum and extending all the way up into the right supra-clavicular region while the left lung was disease-free. Each volumetric data set was acquired with a section spacing of 2 to 3 mm and a reconstruction matrix of 512 × 512. In-plane pixel spacing is approximately 0.97 mm × 0.97 mm.

4.2.3 Image Registration

Review of small deformation inverse consistent linear elastic (SICLE) image registration: SICLE [67] was used to estimate transformations T1, T2 and T3 shown in Table 4.1 and Figure 4.1. The SICLE algorithm minimizes the inverse consistency error between the forward transformation h from template image T to target image S and the reverse transformation g from S to T, providing more accurate correspondences between two images compared to algorithms that independently estimate forward and reverse transformations. The transformations h and g are jointly estimated by minimizing the cost function

$$\begin{aligned} C = \sigma(&\int_\Omega |T(h(x)) - S(x)|^2 dx + \int_\Omega |S(g(y)) - T(y)|^2 dy) \\ &+ \chi(\int_\Omega ||h(x) - g^{-1}(x)||^2 dx + \int_\Omega ||g(y) - h^{-1}(y)||^2 dy) \\ &+ \rho(\int_\Omega ||Lu(x)||^2 dx + \int_\Omega ||Lw(y)||^2 dy), \end{aligned} \tag{4.1}$$

where Ω is the domain of the images T and S. Assume that $h(x) = x + u(x)$, $h^{-1}(y) = y + \widetilde{u}(y)$, $g(y) = y + w(y)$ and $g^{-1}(x) = x + \widetilde{w}(x)$ where $h^{-1}(h(x)) = x$ and $g^{-1}(g(y)) = y$. Here u, w, $\widetilde{u}$ and $\widetilde{w}$ are called displacement fields since they

define the transformation in terms of a displacement from a location x. The first two integrals of the cost function define the cumulative intensity squared error (shape differences) between the deformed image $T \circ h$ and image S and the differences between the deformed image $S \circ g$ and image T. The second two integrals define the inverse consistency error which is minimized when $h = g^{-1}$. This constraint couples the estimation of h and g together and penalizes transformations that are not inverses of each other. The third two integrals are linear elastic constraint which applies the linear elasticity operator [67] L to ensure that the transformations maintain the topology of the images T and S. This term is used to regularize the forward and reverse voxel displacement fields $u(x)$ and $w(y)$, so that they are smooth and continuous by penalizing large derivatives of the displacement fields. For this study, the weighting constants were set as $\sigma = 1$, $\chi = 600$, and $\rho = 0.00125$. These parameters are similar to those used in our previous work [9].

B-splines image registration with local rigidity penalty (Elastix-NRP): A high probability exists for the tumor to have changed fundamentally in size and shape between the $\mathrm{FB_{PRE}}$ study and the $\mathrm{EE_{POST}}$ and $\mathrm{EI_{POST}}$ scans, since substantial radiation dose has been delivered and significant time has passed. In order to avoid introducing an apparent local function change due to tumor size change due to RT, the T4 transformation that registers $\mathrm{EE_{POST}}$ to $\mathrm{FB_{PRE}}$ is computed by a non-rigid registration with a local rigidity penalty (NRP) term [101] using Elastix (http://elastix.isi.uu.nl). The $\mathrm{EE_{POST}}$ image is registered to the $\mathrm{FB_{PRE}}$ image using mutual information and a B-splines parameterized transformation. To define the

local rigidity constraint, the lung is segmented using the method from [72] and the tumor region is manually segmented. The non-rigid registration with local rigidity penalty term method has been previously described in [101]. The impact of the local rigidity penalty was analyzed by visual inspection, difference imaging, and overall quantitative effect on computed vector displacement of voxels within and immediately surrounding the tumor.

4.2.4 Computational Setup

Processing starts by resampling all five CT data sets to a voxel size of 1 mm $\times$ 1 mm $\times$ 1 mm. After resampling, the main airways are identified on all images using the Pulmonary Workstation 2.0 (VIDA Diagnostics, Inc., Iowa City, IA). The airway segmentation algorithm uses a seeded region growing method with an adaptive threshold. The segmentation is initialized with seed voxels from the trachea. After airway segmentation, the images are translated into a common coordinate system by aligning the carinas. Image FB_{PRE} is defined as the reference image.

After this preprocessing, EE_{PRE} is registered to FB_{PRE} using SICLE to find T3. Next T1 (EI_{PRE} to EE_{PRE}) and T2 (EI_{POST} to EE_{POST}) are estimated using SICLE.

To find T4 (EE_{POST} to FB_{PRE}), the non-rigid registration with local rigidity penalty term method is applied. This registration is performed in two stages. For the first stage of initial alignment, five image resolutions are used and no lung mask and rigid penalty term are applied. B-spline grid spacing is set to 10 voxels and the number of optimization iterations is 500 for each resolution. For the second stage

of fine alignment, the lung mask in the target image (FB_{PRE}) is applied and rigid penalty term is specified. The rigidity is set to 1.0 in the tumor region and 0.0 in other lung regions. In this stage, the full resolution images are registered with B-spline grid spacing of 10 voxels followed by registration using B-spline grid spacing of 5 voxels. In this way, the cost function is first optimized for the whole lung region and then specifically for the rigid tumor region. For more details about the parameter settings for our study, please see http://elastix.isi.uu.nl/wiki.php.

4.2.5 Assessment of Image Registration Accuracy

Approximately 120 vascular bifurcation points are used as landmarks to evaluate registration accuracy. A landmark annotating system [10] is used to guide the observer to find the corresponding landmarks in the FB_{PRE}, EE_{PRE}, EI_{PRE}, EE_{POST}, and EI_{POST} images. Each landmark pair manually annotated by the observer was added to a thin-plate-spline to warp the FB_{PRE} image and predict the position for the next unmatched landmark for the observer. The matching task for the observer becomes easier as the warped image is deformed by previously selected landmarks. For each landmark, the actual landmark position is compared to the registration-derived estimate of landmark position and the landmark error is calculated.

4.2.6 Computing Changes in Pulmonary Function

Lung volume change across respiratory cycle is predominantly due to inspired or expired air [52, 24]. Lung ventilation is defined as the volume of air inspired into or expired out of the lungs in a unit time (usually in 1 minute), so air volume change

is proportional to ventilation. Therefore, lung volume change should be correlated to ventilation and specific volume change should be correlated to specific ventilation. We previously shown that the Jacobian is directly related to local specific volume change (sVol, expansion) as sVol $= J - 1$, where J is the Jacobian of the image registration transformation between two images acquired at different lung volumes [9]. Thus, the Jacobian should also be correlated to specific ventilation. Using a sheep model, we compared the regional lung expansion estimated by registering images acquired at different pressures (breath-hold) and respiratory phases (tidal breathing) with the xenon CT specific ventilation in four adult sheep. Regional lung expansion, as estimated from the Jacobian of the image registration transformations, was well correlated with xenon CT specific ventilation [9, 100] (linear regression, average $r^2 = 0.73$). Therefore, the Jacobian can be used as a local measure of pulmonary function. Note that the image pairs used to estimate regional pulmonary expansion via the Jacobian must be acquired within a relatively short time interval, or the assumption that all lung volume change is due to air volume change may not hold.

In our process, local lung expansion can be calculated from the Jacobian of the transformations T1 and T2. The vector transformation function $h(x)$ that maps image T to image S as described in Section 5.2.3 is used to calculate the local lung

expansion and contraction using the Jacobian determinant $J(h(x))$ defined as:

$$J(h(x)) = \begin{vmatrix} \frac{\partial h_1(x)}{\partial x_1} & \frac{\partial h_2(x)}{\partial x_1} & \frac{\partial h_3(x)}{\partial x_1} \\ \frac{\partial h_1(x)}{\partial x_2} & \frac{\partial h_2(x)}{\partial x_2} & \frac{\partial h_3(x)}{\partial x_2} \\ \frac{\partial h_1(x)}{\partial x_3} & \frac{\partial h_2(x)}{\partial x_3} & \frac{\partial h_3(x)}{\partial x_3} \end{vmatrix}. \tag{4.2}$$

where $h_1(x)$ is the x component of $h(x)$, $h_2(x)$ is the y component of $h(x)$, and $h_3(x)$ is the z component of $h(x)$. In a Lagrangian reference frame, there is local tissue expansion if the Jacobian is greater than one; and there is local tissue contraction if the Jacobian is less than one. If we consider a small volume V_s at point x in S and the corresponding volume V_t at $h(x)$ in T, then $J(h(x)) = V_t/V_s$. Therefore, if a lung tissue point has $J(h(x)) = 1.5$, it means the $V_t = 1.5V_s$. Based on our earlier findings [9, 100], a higher Jacobian value reflects a higher specific ventilation.

Transformations T3 and T4 transform the Jacobian data into the coordinate system of FB_{PRE} where they can be compared to look for changes in lung function. As shown in Figure 4.1, the subtraction of the transformed Jacobian data $\text{T-JAC}_{\text{PRE}}$ from Jacobian data $\text{T-JAC}_{\text{POST}}$ results the Jacobian difference image which is the image of the pulmonary function change.

4.2.7 Comparing Regional Pulmonary Function Change to Planned Radiation Dose Distribution

We are interested in looking at the resultant change in the local Jacobian and comparing those changes with the computed RT planning system dose distribution map. The radiation dose distribution image has voxel size of 4 mm × 4 mm × 4 mm

(Pinnacle treatment planning system, version 8.0). Linear interpolation was used to resample the radiation dose distribution image to the same voxel size as the FB_{PRE} image (1 mm $\times$ 1 mm $\times$ 1 mm). After interpolation, the Jacobian difference and the dose distribution image were aligned to the FB_{PRE} image. Registration of both images and the dose distribution to a common coordinate system allows the radiation dose and the change in pulmonary function to be compared.

4.3 Results

4.3.1 Registration Accuracy

Approximately 120 manually identified landmarks within the lungs were used to compute registration accuracy. The landmarks were nominally uniformly distributed between two lungs for each subject. Figure 4.2 shows an example of the distribution of the landmarks in subject B for the FB_{PRE} image, where the red region is the manually-segmented tumor within the right lung and blue spheres are the landmarks. The (x,y,z) coordinate of each landmark location was recorded for each CT data set (EI_{PRE}, EE_{PRE}, EI_{POST}, EE_{POST} and FB_{PRE}) before and after registration for both subjects. Figure 4.3(a) shows the magnitude of respiratory motion for subject A prior to RT, with anatomical landmarks having pre-RT excursions of 2 to 12 mm in the contralateral lung and half that distance in the ipsilateral lung. Following the non-rigid registration of the EI_{PRE} and EE_{PRE} data sets, the average landmark distances are of the order of 1 mm. Figure 4.3(b) shows similar motion of landmarks post-RT before registration, with $\sim$ 1 mm distances between landmark points following registration. The registration pair EE_{PRE} and FB_{PRE} (Fig. 4.3(c))

shows the smallest landmark distance both before and after registration in two cases. The amplitude of breathing during the free breathing scan FB_{PRE} was assumed to have been acquired with a mean position predominantly weighted by the end of expiration of 4DCT. Thus, there is little anatomic difference in the registration pair EE_{PRE} and FB_{PRE} compared to other registration pairs. Conversely, Fig. 4.3(d) shows the EE_{POST} is different from the FB_{PRE} image, as these are acquired on different days. For this subject the non-rigid registration produced superior agreement between landmarks in the ipsilateral lung than observed in the contralateral lung. The respiratory motion from Subject B (Fig. 4.4) produced larger pre-RT excursions (range 2 to 18 mm) which were reduced overall following $\sim$ 23 Gy of RT. Overall the post-RT excursions (Fig. 4.4(b)) were of the same magnitude in the both lungs. The trends for subject B in Fig. 4.4(c) and Fig. 4.4(d) were consistent with those observed for subject A, in both pre-RT and post-RT. These results demonstrate that the average landmark registration error is on the order of 1 mm for both subjects.

4.3.2 Regional Pulmonary Function Change and Planned Radiation Dose Distribution

Figure 4.5 illustrates the difference between SICLE method and Elastix-NRP method. The first row of the figure shows transverse slices from the target image FB_{PRE} and the template image EE_{POST} at approximately the same anatomic location. The figure shows that, as expected, the tumor volume has decreased after the RT. The second row shows the difference between the registration result (the transformed template image) and the target image for both registration algorithms. While most

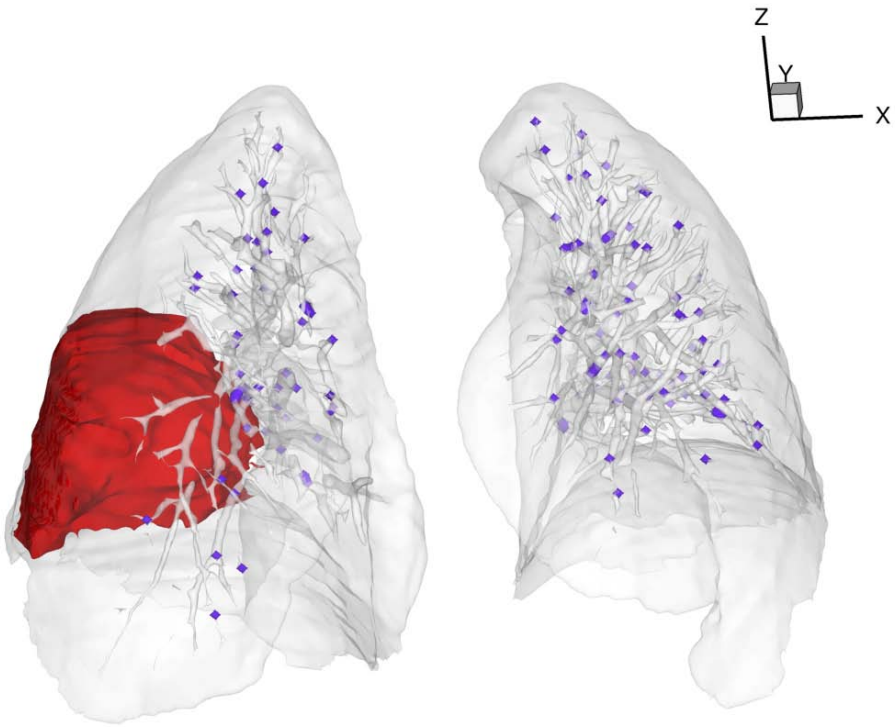

Figure 4.2: 3D view of landmarks as vessel bifurcation points in the FB_{PRE} for subject B. The red region is the manually-segmented tumor and the blue spheres are the manually-defined landmarks.

regions show similar patterns in the difference images, there are some differences in the tissue regions immediately adjacent to the the tumor location. Because the SICLE algorithm has no information about the tumor region, it forces the tumor boundary to match before and after RT. However, the rigidity map in the Elastix-NRP method keeps the tumor as a rigid structure, and is able to capture the differences in the tumor region before and after RT. The third row of the figure shows the resulting

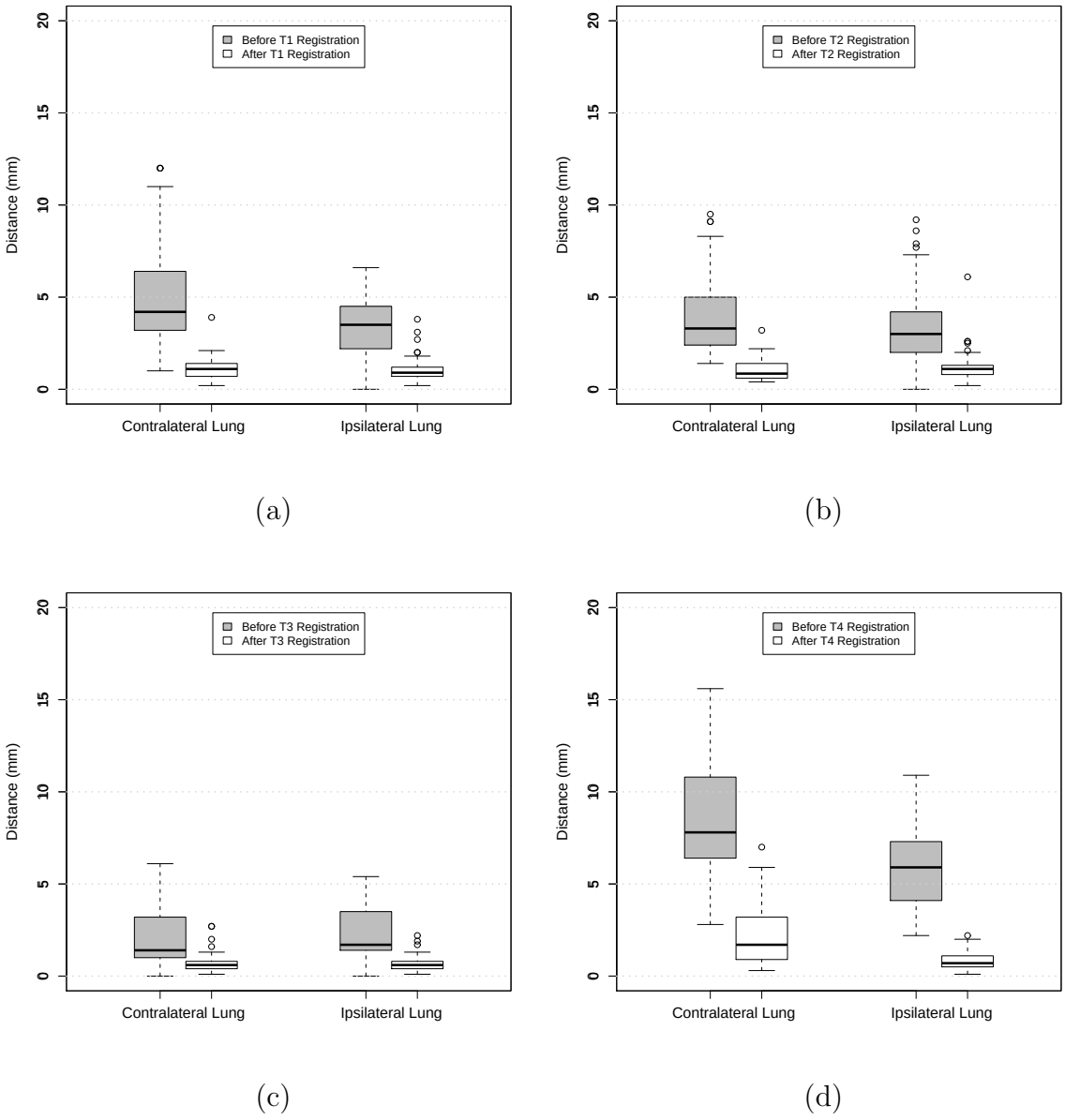

Figure 4.3: Landmark distances for subject A before and after registration. Distances between registration pairs (a) T1: EI_{PRE} and EE_{PRE}; (b) T2: EI_{POST} and EE_{POST}; (c) T3: EE_{PRE} and FB_{PRE}; and (d) T4: EE_{POST} and FB_{PRE}. Boxplot lower extreme is first quartile, boxplot upper extreme is third quartile. Median is shown with solid horizontal line. Whiskers show either the minimum (maximum) value or extend 1.5 times the first to third quartile range beyond the lower (upper) extreme of the box, whichever is smaller (larger). Outliers are marked with circles.

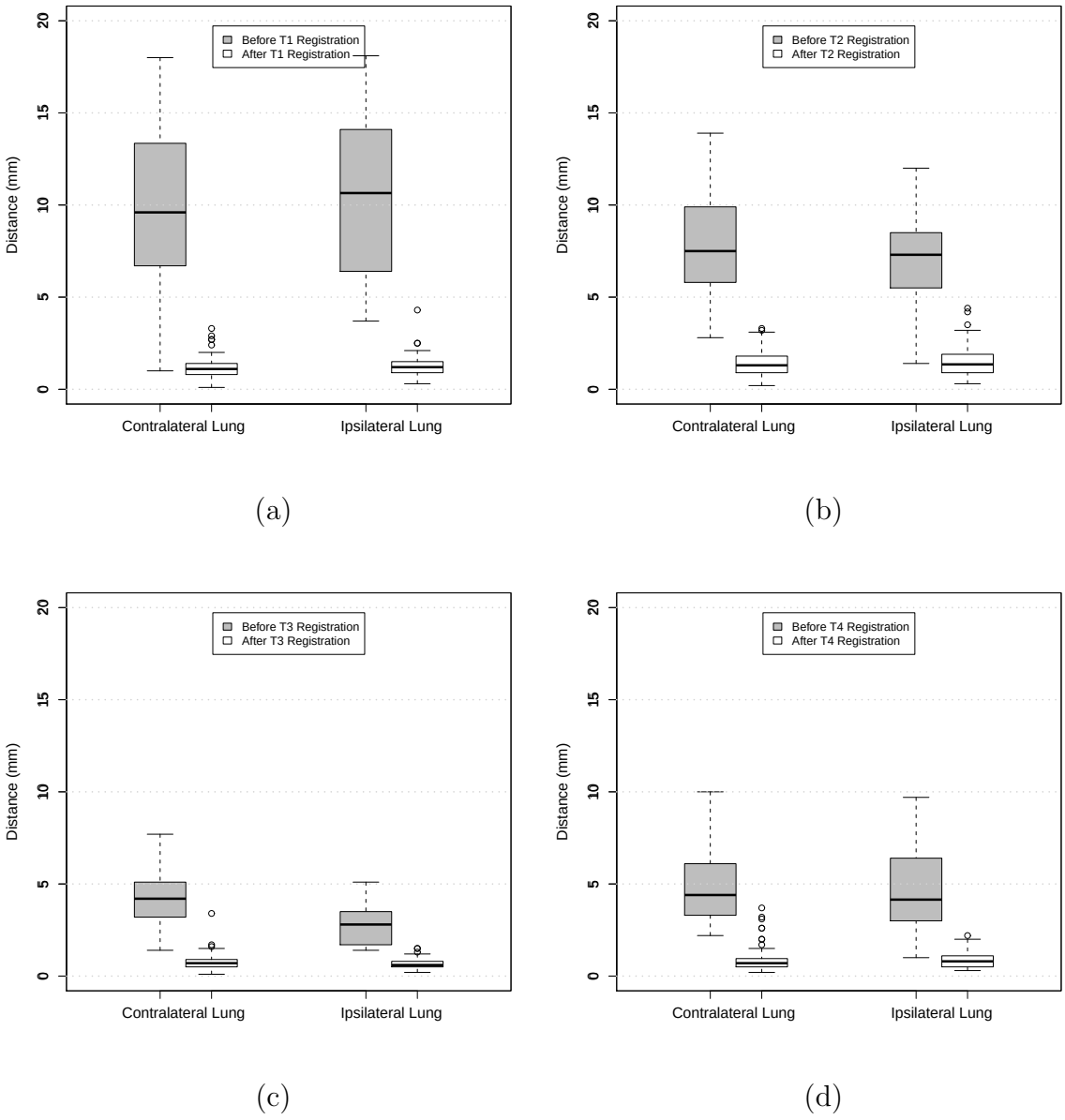

Figure 4.4: Landmark distances for subject B before and after registration. Distances between registration pairs (a) T1: EI_{PRE} and EE_{PRE}; (b) T2: EI_{POST} and EE_{POST}; (c) T3: EE_{PRE} and FB_{PRE}; and (d) T4: EE_{POST} and FB_{PRE}. Boxplot lower extreme is first quartile, boxplot upper extreme is third quartile. Median is shown with solid horizontal line. Whiskers show either the minimum (maximum) value or extend 1.5 times the first to third quartile range beyond the lower (upper) extreme of the box, whichever is smaller (larger). Outliers are marked with circles.

deformation fields near the tumor for SICLE and Elastix-NRP methods. It can been seen that in the regions at the left upper and left lower corners of the image around the tumor, the deformation field from SICLE shows expansion and the deformation field from Elastix-NRP is kept rigid. The final figure in the third row shows the difference in pulmonary function change (DIFF) calculated using SICLE and Elastix-NRP to find the T4 transformation. Again, this result shows that there is a difference in the pulmonary function change estimates derived from these two methods in the regions at the left upper and lower left corner of the image around the tumor.

Figure 4.6 shows the color-coded pulmonary function images and function change image DIFF for both subjects. The first column shows the pulmonary function map before RT. The second column shows the pulmonary function map after RT. Note that the color scales for these images are different for the different subjects because of differences in tidal volume. For example, in subject A, green and blue indicate normally functioning (expanding) lung tissue with a Jacobian value greater than 1.1, while orange and red regions show decreased lung function with a Jacobian value less than 0.95. As described in Section 4.2.7, both function images are mapped to FB_{PRE} using transformations T3 and T4. The pulmonary function change images are shown in column three. In the difference images, blue regions represent increased pulmonary function and the red regions represent decreased pulmonary function. The rightmost column in the figure is the planned radiation dose distribution, in units of Grays (Gy). The spatial map of functional changes in column three can be visually compared to the regions receiving the highest radiation doses (column four).

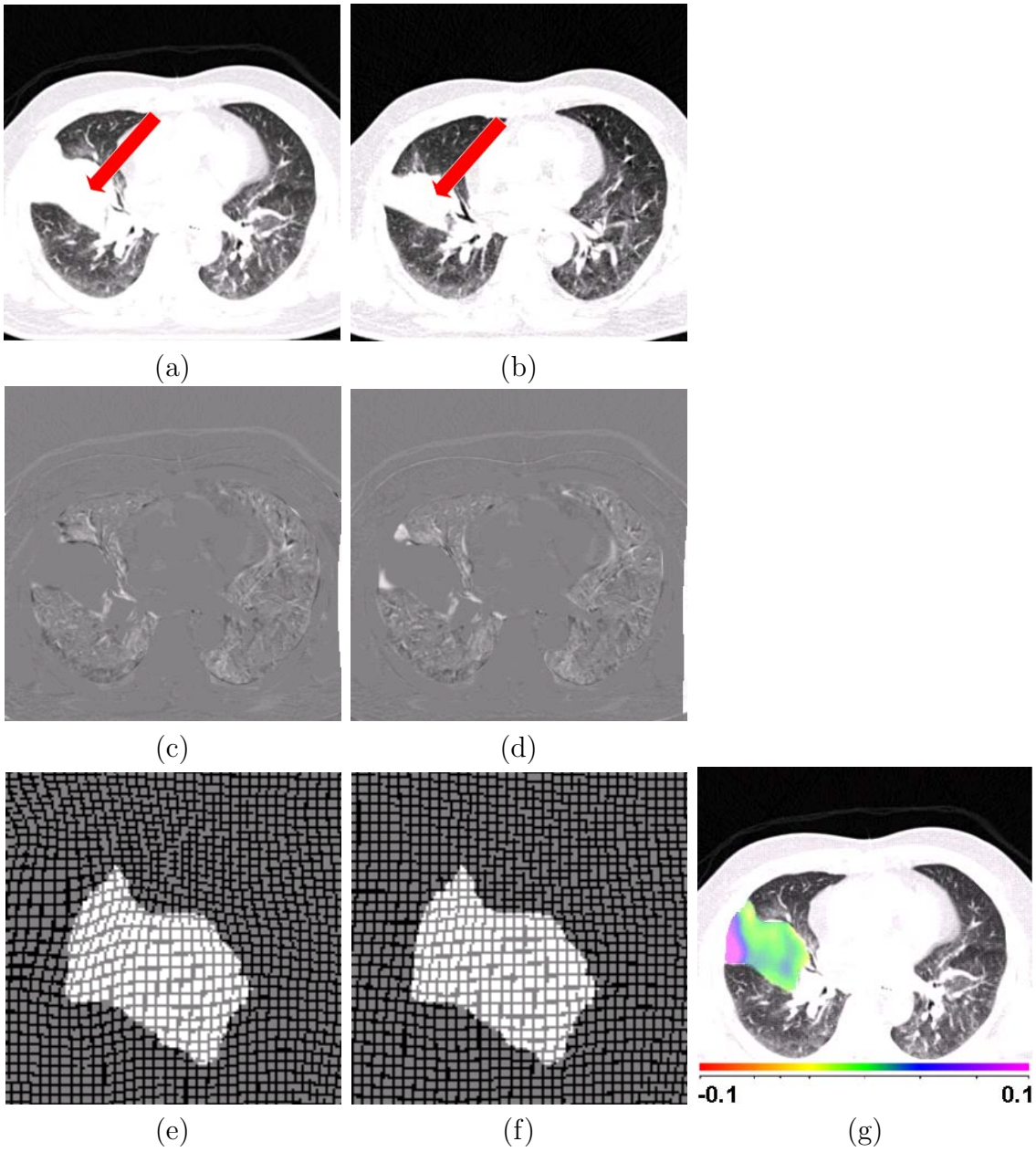

Figure 4.5: Comparison between the SICLE and Elastix-NRP registrations. (a) and (b): Target image FB_{PRE} and template image EE_{POST} with red arrows showing the tumor region. (c) and (d): difference of the registration result with the target image for the purely non-rigid registration SICLE and non-rigid registration with local rigidity penalty term Elastix-NRP. (e) and (f): the resulting deformation field near the tumor for SICLE and Elastix-NRP. (g): the difference of the pulmonary function change from SICLE and Elastix-NRP.

For subject A, the most dramatic change in pulmonary function is seen in the treated left lung (right side of figure), demonstrating changes from significant expansion (green and blue) before RT to little or no expansion (orange to red) after RT in high dose regions. Notice that more regions in the left lung have increased lung function (blue) following RT than the right lung. However, the right lung (left side of the figure) also shows modest changes in lung function while receiving modest radiation (< 8 Gy). The Jacobian change ranges from -0.15 to 0.1 with a mean value of -0.02 in the right lung and from -0.22 to 0.23 with a mean value of -0.02 in the left lung. It is consistent with our expectation that the left lung (ipsilateral lung, where the radiation dose is targeted) has larger change of pulmonary function than the right lung (contralateral lung, where the radiation dose is much lower). The similar mean value of Jacobian change in both lung may be caused by the small volume of the tumor in subject A. For subject B, the first and second columns show modest changes in pulmonary function before and after RT for the untreated left lung, while there is large increase in pulmonary function in the treated right lung following 13 of 37 fractions of RT. The third column in subject B also indicates that the rim of the tumor shows an increase in lung function induced by the decrease in tumor volume. The Jacobian change ranges from -0.40 to 0.39 with a mean value of -0.03 in the contralateral lung and from -0.25 to 0.50 with a mean value of 0.11 in the ipsilateral lung. This change in function might have been concealed if purely nonrigid image registration algorithms were used to estimate T4. The correlation coefficients (linear regression) for pulmonary function change and the radiation dose

were calculated for each patient and each lung. For the subject A, the r value is -0.19 in the ipsilateral lung and -0.14 in the contralateral lung. For subject B, the r value is -0.37 in the ipsilateral lung and 0.25 in the contralateral lung. Therefore, the correlation between the pulmonary function change and radiation dose for the whole lung is very weak and other factors such as treatment location may play a role in this relationship.

Figure 4.7 presents data showing how the relationship between radiation dose and pulmonary function change may have a location-dependent factor. Figures 4.7(a) and 4.7(b) show scatter plots of voxel-by-voxel pulmonary function change (Jacobian change) vs. radiation dose for the entire contralateral and ipsilateral lung in subject A. Figure 4.7(a) shows modest increases in pulmonary function in the contralateral lung post-RT, even though there is much less radiation dose in these regions compared to the treated lung. Figure 4.7(b) shows the same relationship for the ipsilateral lung, where changes in function and radiation doses are much more pronounced. In both lungs, for regions receiving radiation dose smaller than 24 Gy, either an increase or a decrease in pulmonary function is observed. For regions receiving a radiation dose larger than 24 Gy, all regions show a decrease in pulmonary function.

Figures 4.7(c)–(f) show scatter plots between pulmonary function change and radiation dose in the ipsilateral lung within disk-shaped regions at fixed distances from the tumor center. A weak correlation between the dose and pulmonary function change is found at distances from 20 to 25 mm to the tumor (linear regression, $r = -0.73$), suggesting that detected locally-compromised pulmonary function may

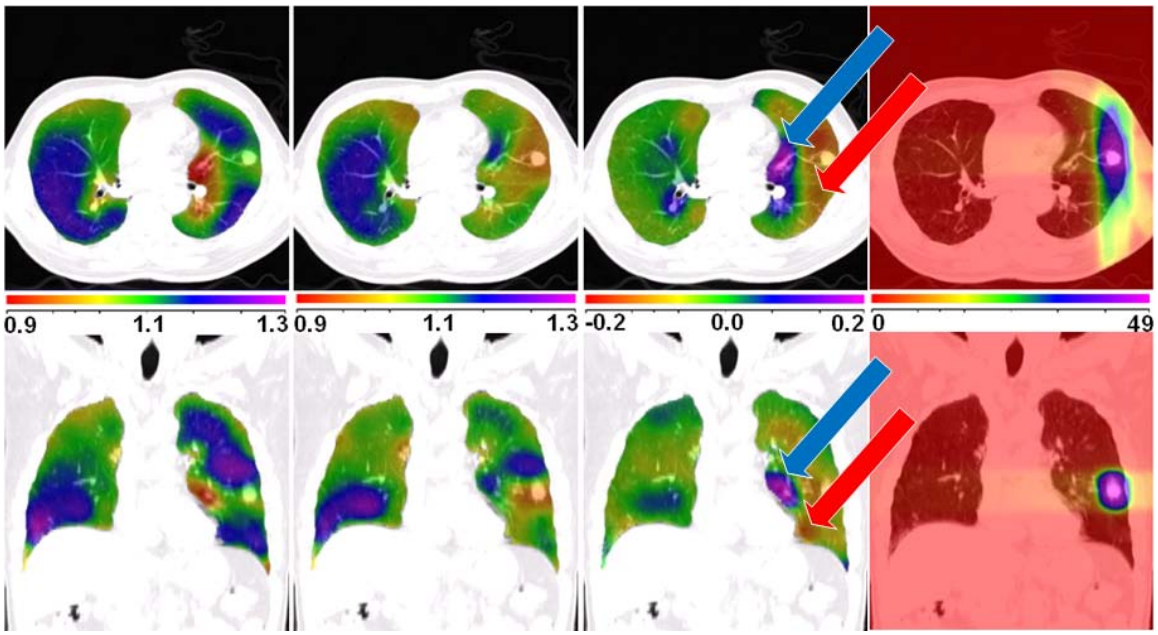

(a) Subject A

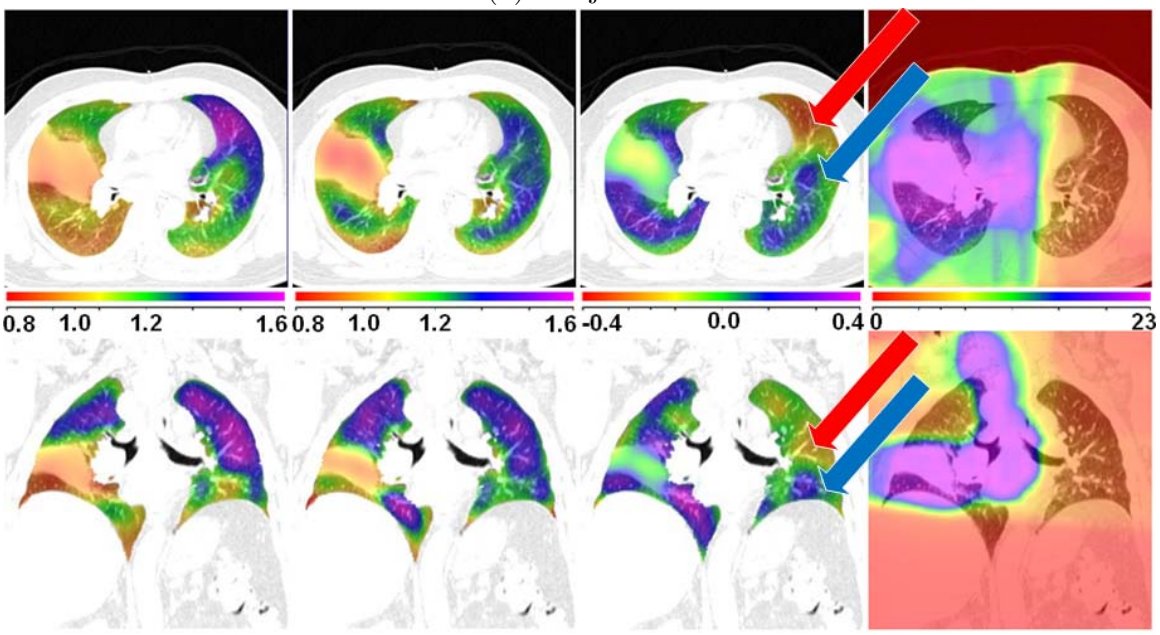

(b) Subject B

Figure 4.6: The pulmonary function change compare to the planned radiation dose distribution. The dose map, pulmonary function and pulmonary function change are overlaid on the FB_{PRE}. The first column is the pulmonary function before RT. The second column is the pulmonary function after RT. The third column is the pulmonary function change from the subtraction of the previous two images. The fourth column is the planned radiation dose distribution. In the third column, the red arrows show regions with decreased pulmonary function and the blue arrows show regions with increased pulmonary function.

have resulted from radiation injury. The figures shown for other distances from the tumor center do not portray such a simple linear relationship. It is likely that dose and distance from the tumor are not the only factors affecting pulmonary function change, and factors such as the initial pulmonary function within the region, anatomic location, and proximity to other pulmonary anatomy will have an effect. More work is needed to investigate these effects and their complex interrelationships.

4.4 Discussion

We have described a method to measure radiation induced spatial pulmonary function change using 4DCT and image registration. Major vascular bifurcations are used as landmarks to evaluate the image registration. Average registration landmark error is on the order of 1 mm.

The SICLE algorithm is used to assess local lung expansion via the Jacobian of the image registration transformation. The SICLE and Elastix-NRP registration methods are used to transform the Jacobian images into the same coordinate system for comparison, and for comparison with the radiation dose map.

The Elastix-NRP algorithm was used with a local rigidity map, to account for the change in lung tumor size before and after RT. Using this approach, the increased pulmonary function of the regions outside tumor after RT can be mapped correctly to the regions inside tumor before RT. For simplicity, we set the rigidity coefficient for the tumor region in the EE_{POST} as one (zero as completely nonrigid tissue and one for rigid tissue). However, in the EE_{PRE} to FB_{PRE} registration using the inverse consistent registration, the average Jacobian value in the tumor region is about 0.94

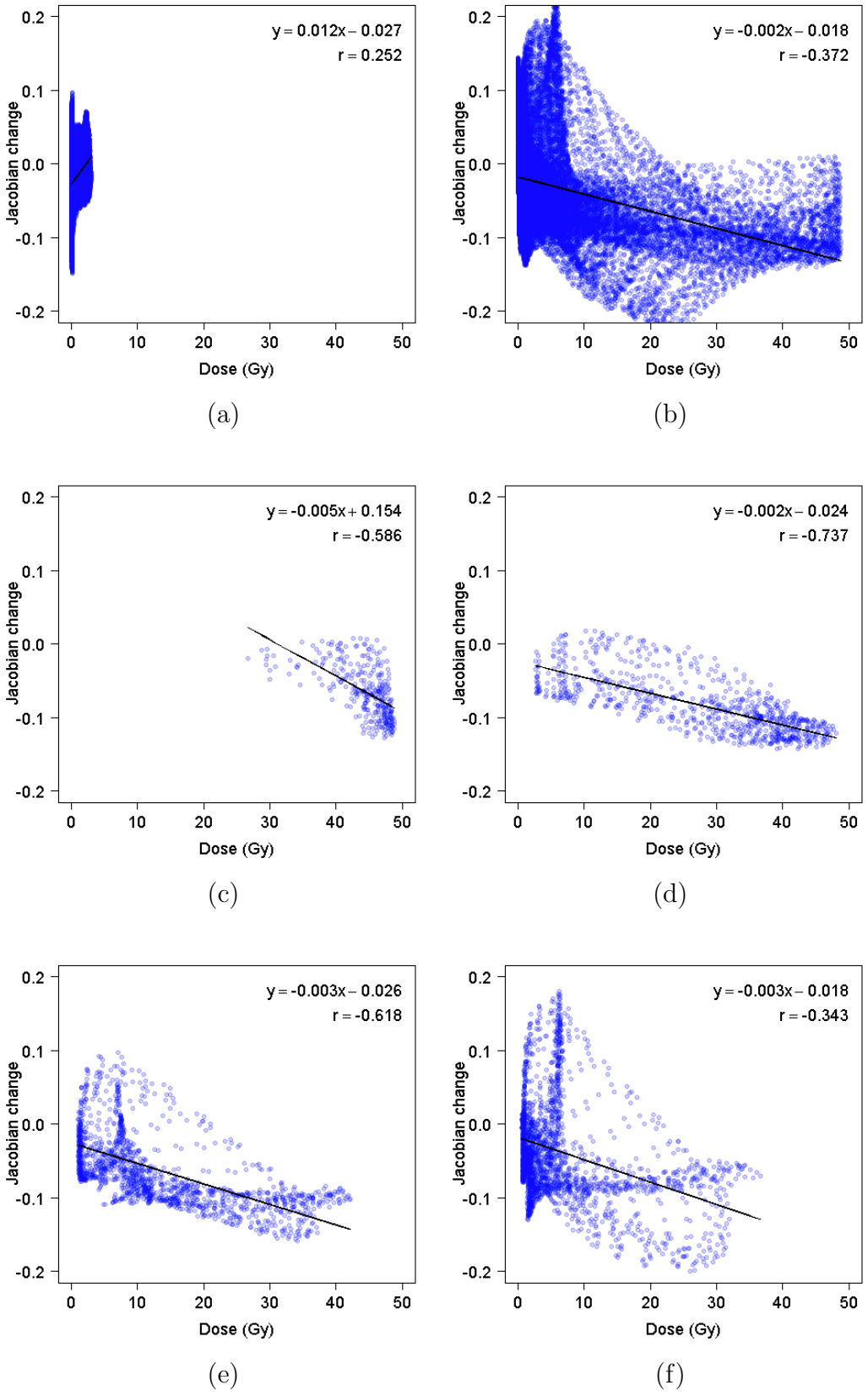

Figure 4.7: Pulmonary function change in subject A compared to the radiation dose in scatter plot with linear regression in (a) contralateral lung, (b) ipsilateral lung and in the ipsilateral lung regions which are at the distance of (c) 10 to 15 mm, (d) 20 to 25 mm, (e) 30 to 35 mm, and (f) 40 to 45 mm to the center of tumor region.

which indicates there is small amount of compression in the tumor region (a value of unity indicates no expansion or contraction). Therefore, more experimentation is needed to find the best rigidity coefficient in tumor to yield physiologically meaningful results.

The pulmonary function change measured by change in the Jacobian of the image registration transformations was compared with the planned radiation dose distribution in two subjects. One subject had fully completed the entire course of RT and the other subject had completed about one-third of the treatment (13 of 37 fractions).

In this study, the difference in pulmonary function change between the treated lung and non-treated lung was examined within each subject. Since in both patients the tumor was confined to one lung (left lung for subject A and right lung for subject B), the pulmonary function change observed in the contralateral lung may be able to serve as a control for the changes observed in the ipsilateral lung. Caution should be used with this approach since spatial functional changes appear to be a function of more than planned radiation dose. Figure 4.6 shows noticeable differences in pulmonary function change between the untreated regions and the treated regions. These differences correlate well with the radiation dose distribution in the high dose regions. Therefore, a more sophisticated analysis that divides the region based on the isocontours of the radiation dose may be more effective in describing this relationship.

In subject A, the treated regions show large decrease of pulmonary function (red) around tumor region and large increase of pulmonary function (blue) in the

ipsilateral lung. For subject B, there is a significant increase of the pulmonary function at the basal regions of the treated (right) lung after the treatment indicating the effectiveness of the radiation therapy. Since the EE_{POST} and EI_{POST} images for subject B are acquired after one-third of the RT treatments, it would be interesting to acquire additional EE_{POST} and EI_{POST} images at other points during therapy so that pulmonary function change can be examined throughout the treatment.

The results in Figure 4.7 show that function change is not only a function of dose, but that there is likely a spatial dependence between the dose distribution and pulmonary function change as well. Other factors, such as initial level of pulmonary function, anatomic location and proximity to the surrounding anatomy, and the effects of a particular RT treatment plan, may also impact lung tissue function change post-RT. Additional work, perhaps using animal models, is required to investigate these effects and their complex interrelationships.

One uncertainty of this comparison is introduced by the difference between the planned and actual dose. The delivered dose at each voxel could be estimated by convolving the planned dose with the known respiratory motion. The motion used would need to be unique for each fraction delivered. Our approach assumes insignificant lung tissue motion to occur during radiation delivery, as the treatment delivery was gated to allow respiratory motion less than the resolution of the dose grid.

The analysis has been limited to comparing response in the ipsilateral vs. contralateral lung. However, it would be natural to consider changes in pulmonary

function at the lobar level as well. It is our expectation that regional pulmonary function may also be affected mechanically by the neighboring lobe. Lobar segmentations, such as those provided by [75], could be overlaid on top of both the dose distribution maps and the pulmonary function change images to observe these effects on a lobe-by-lobe basis.

In conclusion, we have described a method to measure regional pulmonary function change following a course of radiation therapy using image registration. This method may be useful to study the relationships between radiation dose distribution and pulmonary function change, to increase our understanding of the lung toxicity, and to improve radiation therapy for lung tumor control.

CHAPTER 5
COMPARISON OF REGIONAL VENTILATION MEASURES

5.1 Introduction

Lung ventilation is the term used to characterize the volume of air per unit time that enters or exits the lung. Regional ventilation is the measurement of ventilation on a local, or regional, level. Since the primary function of the lung is gas exchange, ventilation can be interpreted as an index of lung function. Injury and disease processes can alter lung function on a global and/or a local level. Recent advances in multi-detector-row CT (MDCT), 4DCT respiratory gating methods, and image processing techniques enable us to study pulmonary function at the regional level with high resolution anatomical information compared to other methods. MDCT can be used to acquire multiple static breath-hold CT images of the lung taken at different lung volumes, or with proper respiratory control, 4DCT images of the lung reconstructed at different respiratory phases [103, 104, 105]. Image registration can be applied to this data to estimate a deformation field that transforms the lung from one volume configuration to the other. This deformation field can be analyzed to estimate local lung tissue expansion, calculate voxel-by-voxel intensity change, and make biomechanical measurements. When combined with image segmentation algorithms, functional and biomechanical measurements can be reported on a lung, lobe, and sublobar basis, or interpreted relative to the anatomy of other important respiratory structure, such as the airway tree [9, 106, 100, 107].

An important emerging application of these methods is the detection of pulmonary function change in subjects undergoing radiation therapy (RT) for lung cancer. During RT, treatment is commonly limited to sub-therapeutic doses due to unintended toxicity to normal lung tissue. Reducing the frequency of occurrence and magnitude of normal lung function loss may benefit from treatment plans that incorporate relationships between regional and functional based lung information and the radiation dose. Yaremko et al. [63] proposed a method incorporating image registration derived estimate of ventilation to reduce normal lung irradiation. We have described how the measurement of pulmonary function may be useful as a planning tool during RT planning, may be useful for tracking the progression of toxicity to nearby normal tissue during RT, and can be used to evaluate the effectiveness of a treatment post-therapy [64].

The physiologic significance of the registration-based measures of respiratory function can be established by comparing to more conventional measurements, such as nuclear medicine or contrast wash-in/wash-out studies with CT or MR. Xenon-enhanced CT (Xe-CT) measures regional ventilation by observing the gas wash-in and wash-out rate on serial CT images [21, 22, 23]. Xe-CT imaging has the advantage of high temporal resolution and anatomical information. Although it comes along with limited axial coverage, it can be used to compare with registration-based measures of regional lung function in animal studies for validation purpose.

This chapter describes three measures to estimate regional ventilation from image registration of CT images. These different measures are evaluated by compar-

ison with Xe-CT estimated ventilation. Individual regional ventilation measures are compared to Xe-CT estimated ventilation by transforming them to the same coordinate system. This provides a clue of which measure to use in order to estimate regional ventilation from image registration of CT images.

5.2 Material and methods

5.2.1 Method Overview

Our goal is to validate and compare the measures used to estimate regional lung ventilation from image registration by comparing them to Xe-CT estimated ventilation. Figure 5.1 shows a block diagram of the entire process. Two types of data were acquired for each animal: a 4DCT scan and a Xe-CT scan. In order to make our comparisons under the same physiological conditions, each animal was scanned and mechanically ventilated with the same tidal volume (TV) and positive end-expiratory pressure (PEEP) during the two types of scans. The data sets from the 4DCT scan were reconstructed at eight phases of respiration. For this study we focus on the data sets from two of the phases, a volume near end expiration (EE) and a volume near end inspiration (EI). For the Xe-CT scan, 45 distinctive partial lung volumetric scans were performed at volume near end expiration, or the initial end expiration scan (EE_0) to the last expiration scan (EE_{44}).

The nonlinear image registration is used to define the transformation T1 between the EE and EI in order to measure the regional lung ventilation from the 4DCT scan. The Xe-CT-based estimated regional lung ventilation is computed on the EE_0 by using Pulmonary Analysis Software Suite 11.0 (PASS) software [108]. The same

nonlinear image registration is also applied to define the transformation T2 which maps the EE_0 to the EE so that the Xe-CT based estimate of ventilation can be mapped into the same coordinate system as that of the registration-based estimate of ventilation. Additional details on the registration algorithm and other processing steps are given below.

5.2.2 Image Data Sets

Appropriate animal ethics approval was obtained for these protocols from the University of Iowa Animal Care and Use Committee and the study adhered to NIH guidelines for animal experimentation. Four adult male sheep A, B, C, and D (with weights 44.0, 37.8, 40.4, and 46.7 kg) were used for this study. The sheep were anesthetized using intravenous pentobarbital and mechanically ventilated during experiments. The 4DCT images were acquired with the animals in the supine position using the dynamic imaging protocol with a pitch of 0.1, slice collimation of 0.6 mm, rotation time of 0.5 sec, slice thickness of 0.75 mm, slice increment of 0.5 mm, 120 kV, 400 mAs, and kernel B30f. Images were reconstructed retrospectively at 0, 25, 50, 75, and 100% of the inspiration duration and 75, 50 and 25% of the expiration duration. The 0% (EE) and 100% (EI) inspiration phases were used for later ventilation measurements. A twelve contiguous axial locations and approximately 45 breaths for Xe-CT studies were selected from the whole lung volumetric scan performed near end-expiration. Images were acquired with the scanner set in ventilation triggering mode with 80 keV energy (for higher Xe signal enhancement), 160 mAs tube current, a 360° rotation, a 0.33 sec scan time, and 2.4 mm slice thickness. Respiratory gating

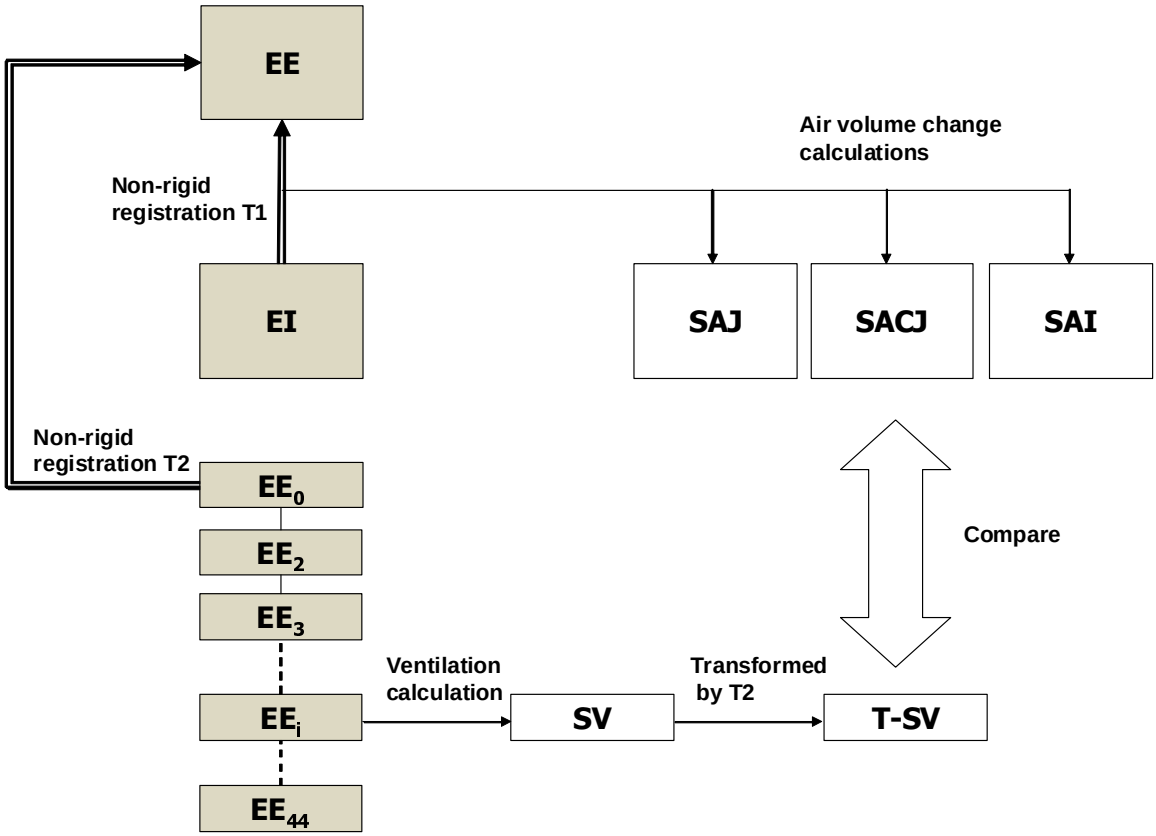

Figure 5.1: Figure shows the two types of images (a image pair from 4DCT scan, the full lung volumetric phases EE and EI, and 45 distinctive partial lung volumetric Xe-CT scans EE_0 to EE_{44} that are analyzed during the processing. Transformations T1 registers end inspiration (EI) to end expiration (EE) data and can be used to assess local lung function via calculations of three ventilation measures: specific air volume change by specific volume change (SAJ), specific air volume change by corrected Jacobian (SACJ), and specific air volume change by intensity (SAI). The 45 distinctive partial lung volumetric Xe-CT scans EE_0 to EE_{44} are used to calculate Xe-CT-based measure of specific ventilation (SV). Transformations T2 maps the SV data into the coordinate system of the EE image (end expiration phase of the 4DCT scan), which allows direct comparison with the 4DCT and registration based measures of ventilation. Both EE and EE_0 are at volumes near end inspiration. (Shaded boxes indicate CT image data; white boxes indicated derived or calculated data; thick arrows indicate image registration transformations being calculated; thin solid lines indicate other operations.)

is achieved by replacing the standard ECG gating signal with a trigger signal from a LabView program. The respiratory rate (RR) for four animals ranges from 15 to 18 breaths per minute. Both of the two types of images were acquired with a matrix of 512 by 512 and without moving the animal between scans.

5.2.3 Image Registration

The tissue volume and vesselness measure preserving nonrigid registration (TVP) algorithm is used to estimate transforms EI to EE and EE_0 to EE. The algorithm minimizes the sum of squared tissue volume difference (SSTVD) [50, 52, 53, 109] and vesselness measure difference (SSVMD), utilizing the rich image intensity information and natural anatomic landmarks provided by the vessels. This method has been shown to be effective at registering across lung CT images with high accuracy [110, 54].

Let I_1 and I_2 represent two 3D image volumes to be registered. The vector $\mathbf{x} = (x_1, x_2, x_3)^T$ defines the voxel coordinate within an image. The algorithm find the optimal transformation $\mathbf{h}$ that maps the template image I_1 to the target image I_2 by minimizing the cost function

$$C_{\text{TOTAL}} = \rho \int_{\Omega} [V_2(\mathbf{x}) - V_1(\mathbf{h}(\mathbf{x}))]^2 \, d\mathbf{x} + \chi \int_{\Omega} [F_2(\mathbf{x}) - F_1(\mathbf{h}(\mathbf{x}))]^2 . \quad (5.1)$$

where Ω is the union domain of the images I_1 and I_2. The transformation $\mathbf{h}$ is a (3×1) vector-valued function defined on the voxel lattice that $\mathbf{h}(\mathbf{x})$ gives its corresponding

location in the template image at location $\mathbf{x}$ in the target image. The first integral of the cost function defines the SSTVD cost and the second integral of the cost function defines the SSVMD cost.

The SSTVD cost assumes that the measured Hounsfield units (HU) in the lung CT images is a function of tissue and air content. Following the findings by Hoffman et. al [78], from the CT value of a given voxel, the tissue volume can be estimated as

$$V(\mathbf{x}) = \nu(\mathbf{x})\frac{I(\mathbf{x}) - HU_{air}}{HU_{tissue} - HU_{air}} = \nu(\mathbf{x})\beta(I(\mathbf{x})), \tag{5.2}$$

and the air volume can be estimated as

$$V'(\mathbf{x}) = \nu(\mathbf{x})\frac{HU_{tissue} - I(\mathbf{x})}{HU_{tissue} - HU_{air}} = \nu(\mathbf{x})\alpha(I(\mathbf{x})), \tag{5.3}$$

where $\nu(\mathbf{x})$ denotes the volume of voxel $\mathbf{x}$ and $I(\mathbf{x})$ is the intensity of a voxel at position $\mathbf{x}$. HU_{air} and HU_{tissue} refer to the intensity of air and tissue, respectively. In this work, we assume that air is -1000 HU and tissue is 0 HU. $\alpha(I(\mathbf{x}))$ and $\beta(I(\mathbf{x}))$ are introduced for notational simplicity, and $\alpha(I(\mathbf{x})) + \beta(I(\mathbf{x})) = 1$.

Given (5.2), we can then define the SSTVD cost:

$$C_{\text{SSTVD}} = \int_{\mathbf{\Omega}} \left[V_2(\mathbf{x}) - V_1(\mathbf{h}(\mathbf{x}))\right]^2 d\mathbf{x} \tag{5.4}$$

$$= \int_{\mathbf{\Omega}} \left[\nu_2(\mathbf{x})\beta(I_2(\mathbf{x})) - \nu_1(\mathbf{h}(\mathbf{x}))\beta(I_1(\mathbf{x}))\right]^2 d\mathbf{x} \tag{5.5}$$

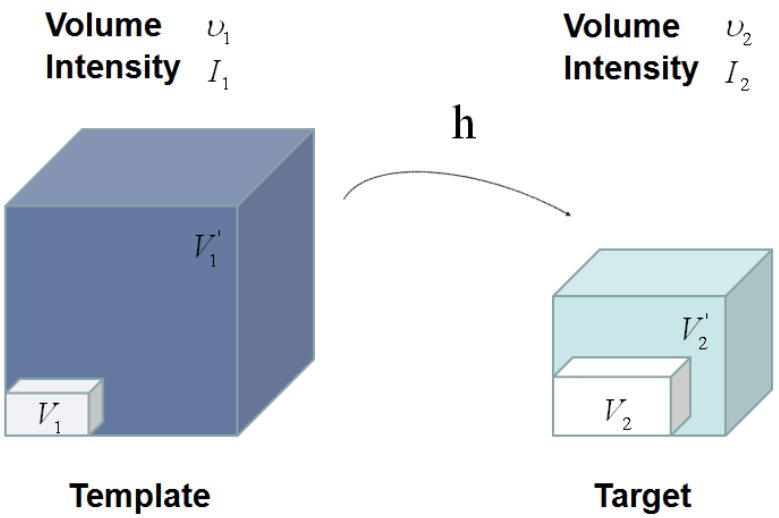

Figure 5.2: Example of a given voxel under deformation $\mathbf{h}(\mathbf{x})$ from template image to target image. V_1 and V_2 are tissue volumes. V_1' and V_2' are air volumes.

With the warping function $\mathbf{h}(\mathbf{x})$, $I_1(\mathbf{h}(\mathbf{x}))$ can be interpolated from the template image. $\nu_1(\mathbf{h}(\mathbf{x}))$ can be calculated from the Jacobian $J(\mathbf{x})$ of the deformation as $\nu_1(\mathbf{h}(\mathbf{x})) = J(\mathbf{x})\nu_2(\mathbf{x})$.

Figure 5.2 shows an example of a given cube under deformation $\mathbf{h}$ from template image to target image. The total cube volumes are ν_1 and ν_2. The intensities in of the cube in the template image and the target image are I_1 and I_2. The small white volume inside the cube represents the tissue volume V_1 and V_2. The air volume is represented by V_1' and V_2'. Notice that as the air flows out of cube and the air volume decreases, the intensity increase from a lower value I_1 to a higher value I_2. In Figure 5.2, the dark blue in the template cube represents lower intensity and the light blue in the target cube represents higher intensity. Both tissue volume and the air volume change in this example.

As the blood vessels branch to small diameters, the raw grayscale information from vessel voxels provide almost no contribution to guide the intensity-based registration. To better utilize the information of blood vessel locations, we use the vesselness measure (VM) based on the eigenvalues of the Hessian matrix of image intensity. Frangi's vesselness function [111] is defined as

$$F(\lambda) = \begin{cases} (1 - e^{-\frac{R_A^2}{2\alpha^2}}) \cdot e^{\frac{-R_B^2}{2\beta^2}} \cdot (1 - e^{-\frac{S^2}{2\gamma^2}}) & \text{if } \lambda_2 < 0 \text{ and } \lambda_3 < 0 \\ 0 & \text{otherwise} \end{cases} \tag{5.6}$$

with

$$R_A = \frac{|\lambda_2|}{|\lambda_3|}, \qquad R_B = \frac{|\lambda_1|}{\sqrt{|\lambda_2 \lambda_3|}}, \qquad S = \sqrt{\lambda_1^2 + \lambda_2^2 + \lambda_3^2}, \tag{5.7}$$

where R_A distinguishes between plate-like and tubular structures, R_B accounts for the deviation from a blob-like structure, and S differentiates between tubular structure and noise. The vesselness function has been previously widely used in vessel segmentations in lungs [77, 112] and in retinas [113]. α, β, γ control the sensitivity of the vesselness measure. The vesselness measure is rescaled to [0, 1] and can be considered as a probability-like estimate of vesselness features. For this study, $\alpha = 0.5$, $\beta = 0.5$, and $\gamma = 5$ and the weighting constants in the total cost were set as $\rho = 1$ and $\chi = 0.2$. These parameters are similar to those used in our previous work [110, 54]. The transformation $\mathbf{h}(\mathbf{x})$ is a cubic B-splines transform:

$$\mathbf{h}(\mathbf{x}) = \mathbf{x} + \sum_{i \in G} \phi_i \beta^{(3)}(\mathbf{x} - \mathbf{x}_i), \tag{5.8}$$

where ϕ_i describes the displacements of the control nodes and $\beta^{(3)}(\mathbf{x})$ is a three-dimensional tensor product of basis functions of cubic B-Spline. A spatial multiresolution procedure from coarse to fine is used in the registration in order to improve speed, accuracy and robustness. The total cost in Equation 5.1 is optimized using a limited-memory, quasi-Newton minimization method with bounds (L-BFGS-B) [55] algorithm. Based on the sufficient conditions to guarantee the local injectivity of functions parameterized by uniform cubic B-Splines proposed by Choi and Lee [56], the B-Splines coefficients are constrained so that the transformation maintains the topology of two images.

5.2.4 Regional Ventilation Measures from Image Registration

After we obtain the optimal warping function, we can calculate the regional ventilation, which is equal to the difference in local air volume change per unit time. Therefore, the specific ventilation is equal to specific air volume change per unit time. These three ventilation measures are described below.

Specific air volume change by specific volume change (SAJ): The assumption for regional ventilation measure is that local volume change is only due to air and the regional volume change is only caused by the local air volume change. Or in other words, there is no tissue volume in a given local volume. Figure 5.3 illustrates such assumption. Compared with a general condition in Figure 5.3, the local volume now is purely air volume, or equivalently, $\nu_1 = V_1'$ and $\nu_2 = V_2'$. Then the specific

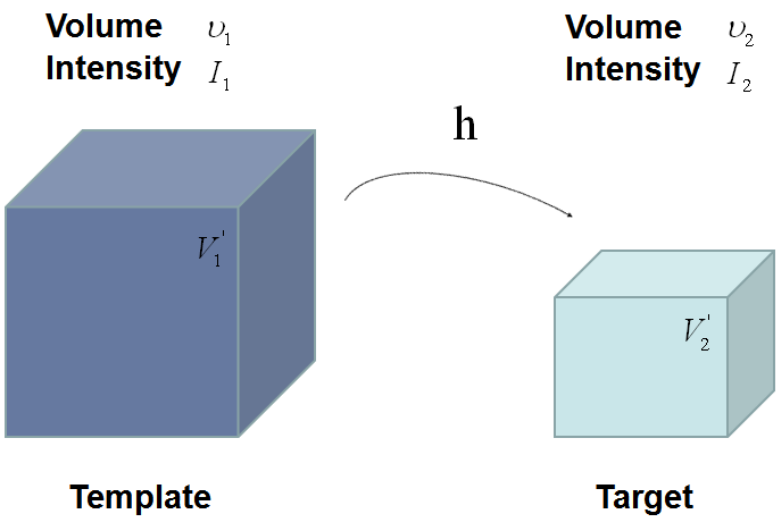

Figure 5.3: Example of a given voxel under deformation $\mathbf{h}(\mathbf{x})$ from template image to target image, with the assumption of no tissue volume. V_1' and V_2' are air volumes.

air volume change is equal to specific volume change. Since the Jacobian tells us the local volume expansion (or contraction), the regional ventilation can be measured by:

$$SAJ = \frac{\nu_1(\mathbf{h}(\mathbf{x})) - \nu_2(\mathbf{x})}{\nu_2(\mathbf{x})} = J(\mathbf{x}) - 1. \tag{5.9}$$

We used this measure as index of the regional function and compared it with the Xe-CT estimate of regional lung function along the lung height direction. Regional lung expansion, as estimated from the Jacobian of the image registration transformations, was well correlated with xenon CT specific ventilation [9, 100] (linear regression, average $r^2 = 0.73$).

Specific air volume change by corrected Jacobian (SACJ): Applying the same assumptions (5.2) and (5.3) used in the SSTVD cost function, we have

$$SACJ = \frac{V_1'(\mathbf{h}(\mathbf{x})) - V_2'(\mathbf{x})}{V_2'(\mathbf{x})} \tag{5.10}$$

$$= \frac{V_1'(\mathbf{h}(\mathbf{x}))}{V_1'(\mathbf{x})} - 1 \tag{5.11}$$

$$= \frac{\nu_1(\mathbf{h}(\mathbf{x}))\alpha(I_1(\mathbf{h}(\mathbf{x})))}{\nu_2(\mathbf{x})\alpha(I_2(\mathbf{x}))} - 1 \tag{5.12}$$

Given a warping function $\mathbf{h}(\mathbf{x})$, $I_1(\mathbf{h}(\mathbf{x}))$ can be interpolated from the template image. $\nu_1(\mathbf{h}(\mathbf{x}))$ can be calculated from the Jacobian $J(\mathbf{x})$ of the deformation as $\nu_1(\mathbf{h}(\mathbf{x})) = J(\mathbf{x})\nu_2(\mathbf{x})$. Therefore, the specific air volume change is then

$$SACJ = J(\mathbf{x})\frac{\alpha(I_1(\mathbf{h}(\mathbf{x})))}{\alpha(I_2(\mathbf{x}))} - 1 \tag{5.13}$$

$$= J(\mathbf{x})\frac{HU_{tissue} - I_1(\mathbf{h}(\mathbf{x}))}{HU_{tissue} - I_2(\mathbf{x})} - 1 \tag{5.14}$$

If we assume that air is -1000 HU and tissue is 0 HU, then specific air volume change is

$$SACJ = J(\mathbf{x})\frac{I_1(\mathbf{h}(\mathbf{x}))}{I_2(\mathbf{x})} - 1. \tag{5.15}$$

Compared to Equation 5.9, the correction factor $\frac{I_1(\mathbf{h}(\mathbf{x}))}{I_2(\mathbf{x})}$ above depends on the voxel intensity. Notice that Figure 5.2 is corresponding SACJ which represents the most general case of volume changes.

Specific air volume change by intensity (SAI): The intensity based measure of regional air volume change SAI can be derived from the SACJ. Now we introduce another assumption that the tissue volume is preserved, or equivalently, that the tissue volume difference $\Delta V(\mathbf{x}) = V_1(\mathbf{h}(\mathbf{x})) - V_2(\mathbf{x}) = 0$. Under this assumption,$V_1(\mathbf{h}(\mathbf{x})) = V_2(\mathbf{x})$ and we have

$$\nu_1(\mathbf{h}(\mathbf{x}))\beta(I_1(\mathbf{h}(\mathbf{x}))) = \nu_2(\mathbf{x})\beta(I_2(\mathbf{x})), \tag{5.16}$$

and

$$\nu_1(\mathbf{h}(\mathbf{x})) = \nu_2(\mathbf{x})\frac{\beta(I_2(\mathbf{x}))}{\beta(I_1(\mathbf{h}(\mathbf{x})))}, \tag{5.17}$$

Since $\nu_1(\mathbf{h}(\mathbf{x})) = J(\mathbf{x})\nu_2(\mathbf{x})$, with above equation, we have

$$\begin{aligned} J(\mathbf{x}) &= \frac{\beta(I_2(\mathbf{x}))}{\beta(I_1(\mathbf{h}(\mathbf{x})))} && (5.18)\\ &= \frac{I_2(\mathbf{x}) - HU_{air}}{I_1(\mathbf{h}(\mathbf{x})) - HU_{air}}. && (5.19) \end{aligned}$$

Substituting the above equation into equation 5.14, yields

$$SAI = \frac{I_2(\mathbf{x}) - HU_{air}}{I_1(\mathbf{h}(\mathbf{x})) - HU_{air}}\frac{HU_{tissue} - I_1(\mathbf{h}(\mathbf{x}))}{HU_{tissue} - I_2(\mathbf{x})} - 1 \tag{5.20}$$

$$= \frac{I_2(\mathbf{x})HU_{tissue} + HU_{air}I_1(\mathbf{h}(\mathbf{x})) - I_1(\mathbf{h}(\mathbf{x}))HU_{tissue} - HU_{air}I_2(\mathbf{x})}{(I_1(\mathbf{h}(\mathbf{x})) - HU_{air})(HU_{tissue} - I_2(\mathbf{x}))} \tag{5.21}$$

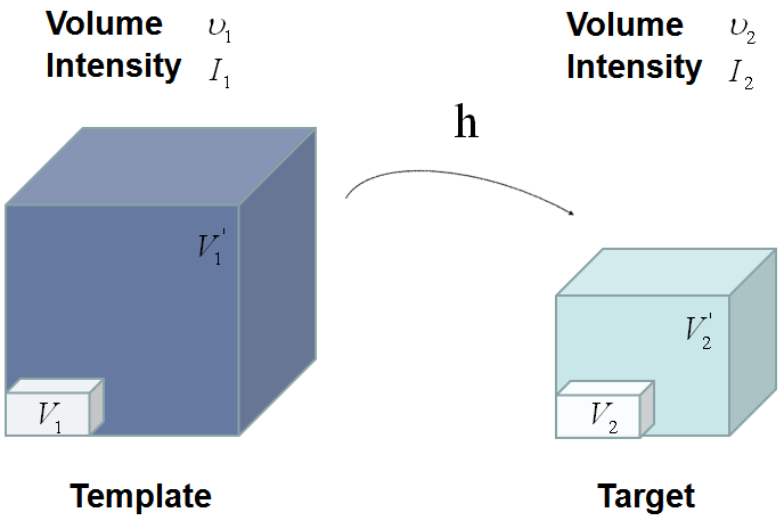

Figure 5.4: Example of a given voxel under deformation $\mathbf{h}(\mathbf{x})$ from template image to target image, with the assumption of no tissue volume change. Notice the tissue volume $V_1 = V_2$ under this assumption. V_1' and V_2' are air volumes.

If we assume that air is -1000 HU and tissue is 0 HU, then

$$SAI = 1000\frac{I_1(\mathbf{h}(\mathbf{x})) - I_2(\mathbf{x})}{I_2(\mathbf{x})(I_1(\mathbf{h}(\mathbf{x})) + 1000)} \tag{5.22}$$

which is exactly the equation as described in Simon [114], Guerrero et al. [25] and Fuld et al. [24].

Figure 5.4 illustrates the assumption with no tissue volume change in SAI. In Figure 5.4, while the whole volume change s from ν_1 to ν_2, the tissue volume inside the cube remains the same ($V_1 = V_2$).

Difference of specific air volume change (DSA) and difference of tissue volume (DT): To investigate the relationship between the measurements of specific

air volume changes and the tissue volume change, we also measure the difference between equation (5.15) and equation (5.22) by comparing the difference of specific air volume change (DSA) between SACJ and SAI, and the difference of tissue volume (DT) as:

$$DSA = SACJ - SAI \tag{5.23}$$

$$\begin{aligned} DT &= V_1(\mathbf{h}(\mathbf{x})) - V_2(\mathbf{x}) && (5.24)\\ &= \nu_1(\mathbf{h}(\mathbf{x}))\beta(I_1(\mathbf{h}(\mathbf{x}))) - \nu_2(\mathbf{x})\beta(I_2(\mathbf{x})) && (5.25)\\ &= J(\mathbf{x})\nu_2(\mathbf{x})\beta(I_1(\mathbf{h}(\mathbf{x}))) - \nu_2(\mathbf{x})\beta(I_2(\mathbf{x})) && (5.26)\\ &= \nu_2(\mathbf{x})\frac{J(\mathbf{x})(I_1(\mathbf{h}(\mathbf{x})) - HU_{air}) - (I_2(\mathbf{x}) - HU_{air})}{HU_{tissue} - HU_{air}} && (5.27) \end{aligned}$$

Again, if we assume that air is -1000 HU and tissue is 0 HU, then the tissue volume difference is:

$$DT = \nu_2(\mathbf{x})\frac{J(\mathbf{x})(I_1(\mathbf{h}(\mathbf{x})) + 1000) - (I_2(\mathbf{x}) + 1000)}{1000} \tag{5.28}$$

In this study, the absolute values of DT and DSA are used in analysis.

5.2.5 Computational Setup

Processing starts by identifying the lung regions in all images using the Pulmonary Workstation 2.0 (VIDA Diagnostics, Inc., Iowa City, IA). The Xe-CT estimate

of SV is computed in the coordinates of the EE_0 using Pulmonary Analysis Software Suite 11.0 (PASS) [108] at the original image size of 0.5 mm $\times$ 0.5 mm $\times$ 2.4 mm voxels. Overlapping 1 $\times$ 8 regions of interest (ROI) are defined in the lung region on each 2D slice. All the images including the EE, EI, EE_0 and their corresponding lung region masks or SV map are then resampled to a voxel size of 1 mm $\times$ 1 mm $\times$ 1 mm. After preprocessing, EI is registered to EE using the TVP for measuring the regional ventilation from these two phases in a 4DCT scan. The resulting transformation is used to estimate the SAJ, SACJ and SAI. Then EE_0 is registered to EE using TVP as well to map the SV to the same coordinate system as that of the SAJ, SACJ and SAI. For the TVP, the multiresolution strategy is used in the processing and it proceeds from low to high image resolution starting at one-eighth the spatial resolution and increases by a factor of two until the full resolution is reached. Meanwhile, a hierarchy of B-spline grid spaces from large to small is used. The finest B-spline grid space used in the experiments is 4 mm. The images and image grid space are refined alternatively.

5.2.6 Assessment of image registration accuracy

A semi-automatic landmark system is used for landmark detection and detection [10]. First, an automatic landmark detection algorithm from the system is applied to find the landmarks in the EE. The algorithm automatically detects "distinctive" points in the target image as the landmarks based on a distinctiveness value $D(p)$. Around each point p, 45 points, q_1, ..., q_{45} are uniformly distributed on a spherical surface. A region of interest $ROI(q_i)$ is compared with the corresponding region

of interest $ROI(p)$ around the original point, and then combined with its gradient value to calculate the the distinctiveness value $D(p)$.

The same system is then applied to guide the observer to find the landmarks in the target image with their corresponding voxels in the template image. Each landmark-pair manually annotated by the observer is added to a thin-plate-spline to warp the template image. The system utilizes the warped image to estimate where the anatomic match will be located for a new landmark point presented to the observer, therefore the observer can start the matching from a system estimated location. Thus, as the warped image becomes more accurate by the new added landmarks, the task of the observer becomes easier.

For each animal, after 200 anatomic landmarks are identified in the EE, the observer marks the locations of the voxels corresponding to the anatomic locations of the landmarks in the EI. For each landmark, the actual landmark position is compared to the registration-derived estimate of landmark position and the error is calculated. With the evaluated accuracy of transformation from the lung image registration algorithm, the resulting regional ventilation measures estimated using the transformation can be then compared to Xe-CT estimated ventilation.

5.2.7 Compare Registration Regional Ventilation Measures to Xe-CT Estimated Ventilation

In our previous work [9, 100], regional lung expansion, as estimated from the Jacobian of the image registration transformations, was compared with Xe-CT based SV. The analysis was conducted by evaluating Jacobian value between a pair

of adjacent lung volumes in PEEP or phase (e.g. PEEP 15 to 20 in static scans or inspiration phase 0% to 25% in dynamic scans), and comparing it in the y (ventral-dorsal) axis. While the correlation between the Jacobian value and SV reflect the fact that regional expansion estimated from image registration can be used as an index as regional lung function, the spatial resolution of the analysis method employed might not be sufficient to distinguish the differences between regional ventilation measures as we have described in Section 5.2.4. Therefore, to better compare the regional ventilation measures, the corresponding region of Xe-CT image EE_0 in the EE is divided into about 100 cubes with size of 20 mm $\times$ 20 mm $\times$ 20 mm. We compare the average regional ventilation measures (SAJ, SACJ and SAI) to the corresponding average SV measurement from Xe-CT images within each cube. The correlation coefficients between any two estimates (SAJ-SV, SACJ-SV or SAI-SV) are calculated by linear regression. To compare two correlation coefficients, the Fisher Z-transform of the r values is used and the level of significance is determined [115]. The relationship between the specific air volume change and difference of tissue volume is also studied in four animals by linear regression analysis.

5.3 Results

5.3.1 Registration Accuracy

Approximately 200 automatic identified landmarks within the lungs are used to compute the registration accuracy. The landmarks are uniformly distributed in the lung regions. Figure 5.5 shows an example of the distribution of the landmarks in animal D for both the EE and EI images. The coordinate of each landmark

location is recorded for each image data set before and after registration for all four animals. Figure 5.6 shows the landmark distance before and after registration for four animals. The grey boxplots show the magnitude of respiratory motion during the tidal breathing. For all four animals, before registration, the average landmark distance is 6.6 mm with minimun 1.0 mm, maximum 14.6 mm and stand deviation 2.42 mm. After registration, the average landmark distance is 0.4 mm with minimum 0.1 mm, maximum 1.6 mm and stand deviation 0.29 mm. The trends for all animals are consistent and the result demonstrate that the registration produced good agreement in landmark locations with the observer.

Figure 5.5(a) shows the location of the EE_0 in EE. Figure 5.7 shows an example of the image registration result from EE_0 to EE. The first row shows the misalignment between the images before image registration. Though the images were acquired without moving the animal between the scans, there is still non-rigid deformation between scans as shown in Fig 5.7(d), as the black and white regions represent the large intensity difference between Fig. 5.7(a) and (b). After image registration, the EE_0image is aligned to the EE allowing us to map the SV to the coordinate system of EE as most of the regions are in grey value indicating near zero intensity difference [Fig. 5.7(e)]. Since the regions outside the lung are not included during the registration, the mediastinum and other body tissues are not aligned. Notice that the dorsal region shows a intensity difference after registration. This is mainly due to the progression of the atelectasis and edema during the experiment.

5.3.2 Registration Estimated Ventilation Compared

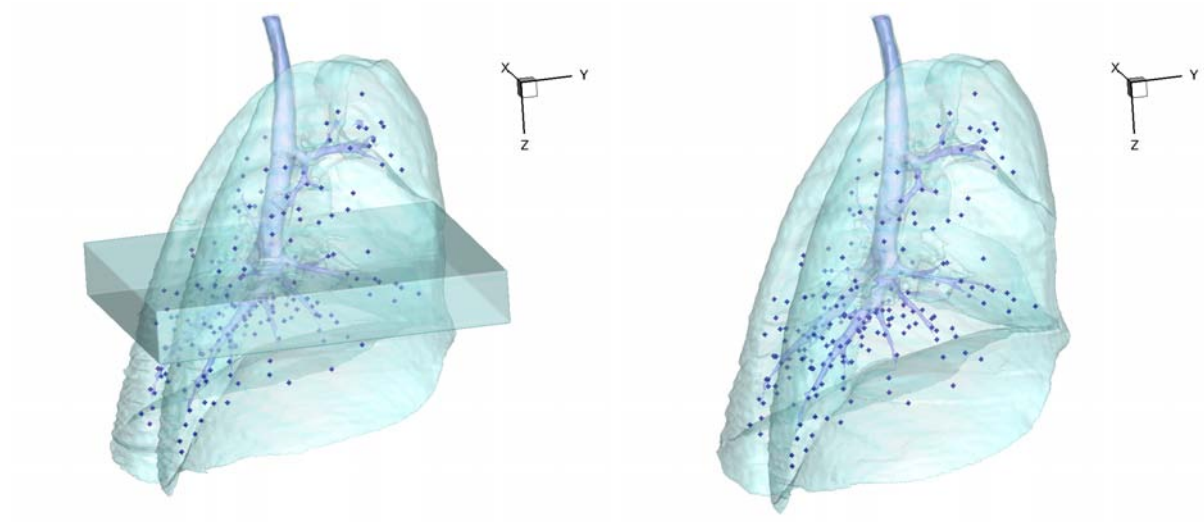

(a) (b)

Figure 5.5: 3D view of the landmarks in: (a) EE with EE_0 and (b) EI. The dark region below the carina in (a) is the EE_0 and the spheres are the automatically defined landmarks.

to Xe-CT Estimated Ventilation

Figure 5.8(a) shows an example of the color-coded cubes of the regions where we average the registration estimated ventilation measures and the Xe-CT estimated SV and compare them. For each animal, the corresponding Xe-CT regions in the EE are divided into about 100 cubes. Figure 5.8(b) is the Xe-CT estimate of SV. Figure 5.8(c), (d), (e) are the corresponding registration ventilation measures SAJ, SACJ amd SAI. The regions with edema are excluded from the comparison. Figure 5.8(b) to (d) all show noticeable similar gradient in the ventral-dorsal direction. Notice that the color scales are different in each map and are set according to their ranges in Fig. 5.9.

Figure 5.9 shows the scatter plots between the registration ventilation mea-

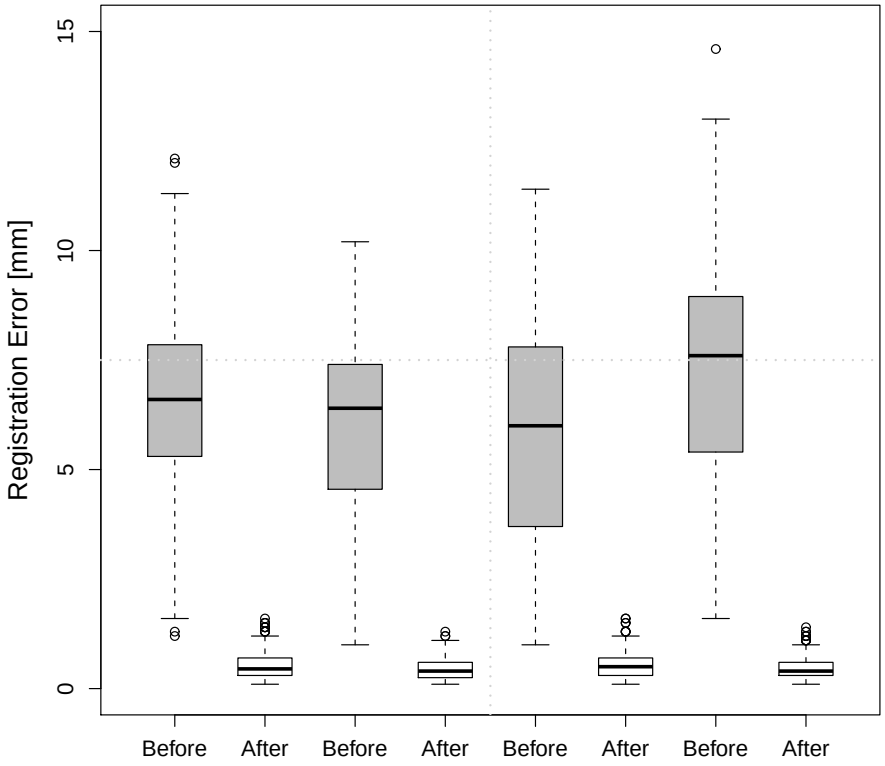

Figure 5.6: Landmarks distances of the registration pair EI to EE for all four animals. Boxplot lower extreme is first quartile, boxplot upper extreme is third quartile. Median is shown with solid horizontal line. Whiskers show either the minimum (maximum) value or extend 1.5 times the first to third quartile range beyond the lower (upper) extreme of the box, whichever is smaller (larger). Outliers are marked with circles.

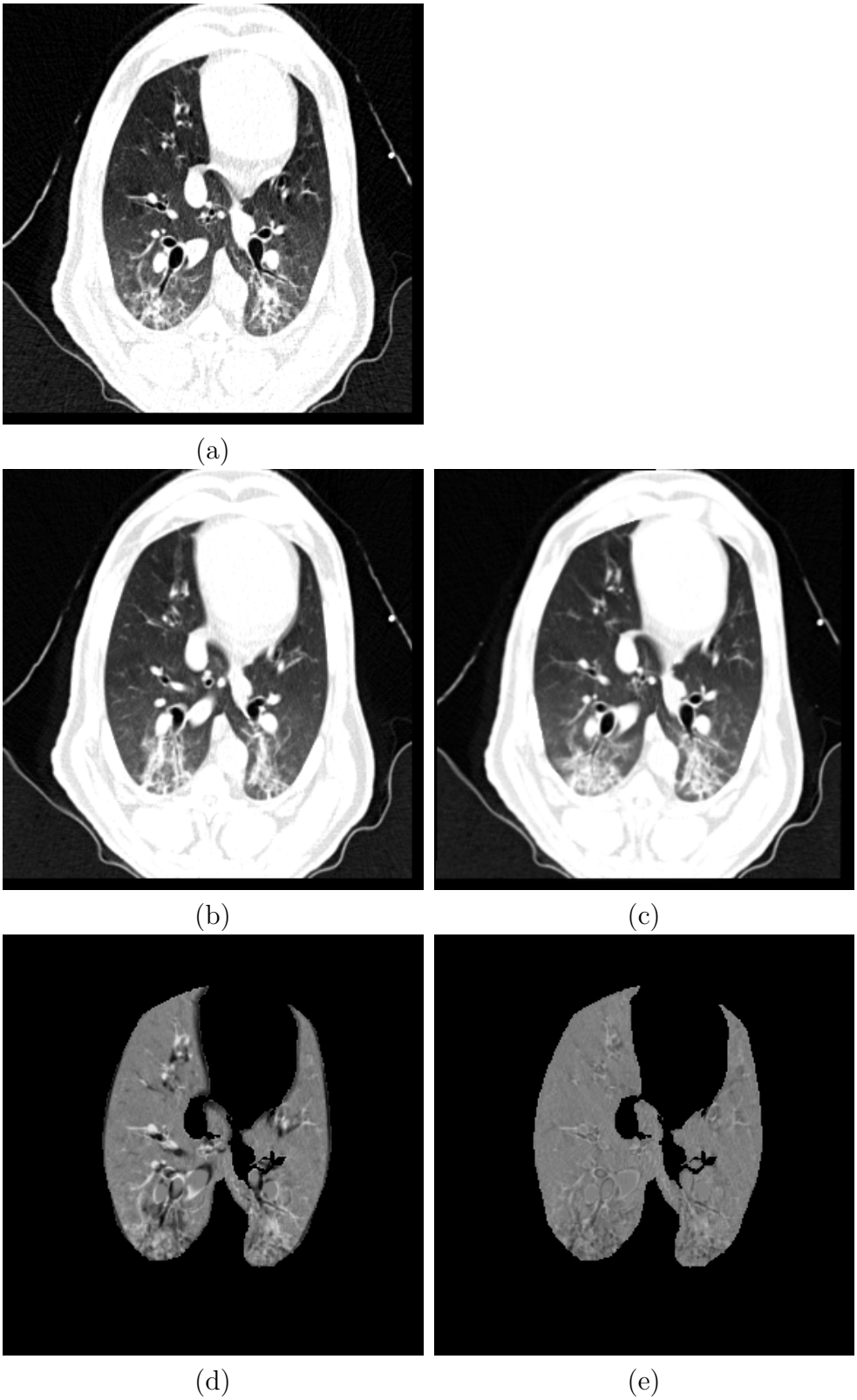

Figure 5.7: Visualization of the result of the transformation that maps the Xe-CT estimated ventilation SV to the EE coordinate system: (a) EE, (b) EE_0, (c) deformed EE_0 after registration, (d) intensity difference between EE and EE_0 before registration, (e) intensity difference between EE and EE_0 after registration.

sures and the Xe-CT ventilation SV with linear regression in all four animals. The SACJ column shows the strongest correlation with the SV (average $r^2 = 0.82$). The SAJ, which is directly related to Jacobian as SAJ = J − 1, also shows good correlation with the SV (average $r^2 = 0.75$). The intensity based measure SAI shows the lowest correlation with the SV (average $r^2 = 0.58$).

Table 5.1 shows the results of comparing the r values from SACJ vs. SV and SAI vs. SV. All four animals show that the correlation coefficient from SACJ vs. SV is significantly stronger than it from SAI vs. SV. Similarly, table 5.2 shows the results of comparing the r values from SAJ vs. SV and SAI vs. SV. The registration ventilation measure SAJ also shows a significantly stronger correlation with SV than SAI.

To analyze the effect of the size of the averaging region, the corresponding region of Xe-CT image EE_0 in the EE is divided into about 30 slabs along the ventral-dorsal direction with size of 150 mm × 8 mm × 40 mm as similarly in our previous work [9, 100]. Figure 5.10 shows the scatter plots between the registration ventilation measures and the Xe-CT ventilation SV similar as Fig. 5.10 but in larger ROIs. The SACJ column shows the strongest correlation with the SV (average $r^2 = 0.92$). Both the SAJ and SAI show good correlation with SV as well (average $r^2 = 0.88$ and $r^2 = 0.87$). However, though the average r^2 value still show the SACJ has the highest correlation with Xe-CT based SV, table 5.3 and table 5.4 show that with larger averaging region as defined slabs, there is no significant difference between the correlation coefficients from SACJ vs. SV and SAI vs. SV, or between SAJ vs. SV

Table 5.1: Comparison of ventilation measures between SACJ and SAI in small cube ROIs with size 20 mm × 20 mm × 20 mm.

Animal	Correlation pair (with SV)	Correlation with SV (r value)	Number of samples	p value
A	SACJ	0.88	83	p<= 0.0001
	SAI	0.65		
B	SACJ	0.93	119	p<= $1.18e^{-6}$
	SAI	0.77		
C	SACJ	0.89	86	p<= 0.015
	SAI	0.78		
D	SACJ	0.92	110	p<= 0.006
	SAI	0.83		

and SAI vs. SV.

Figure 5.11 shows shows the scatter plots between DSA (the absolute difference of the value between the SACJ and SAI) and the DT (the absolute difference of the tissue volume) with linear regression in all four animals (average $r^2 = 0.86$). From the equation (5.14) and (5.21), we know that the SAI takes the assumption about no tissue volume change for a given voxel between the two volumes which may not be valid. Figure 5.11 shows that as the tissue volume change increases, the difference between the measures of regional ventilation from SACJ and SAI increases linearly in all four animals. It indicates that the lower correlation of SAI with SV compared with SACJ with SV may be caused by the tissue volume change between two volumes.

5.4 Discussion

We have described three measures to estimate regional ventilation from tissue volume and vesselness preserving image registration of CT images. The validity and

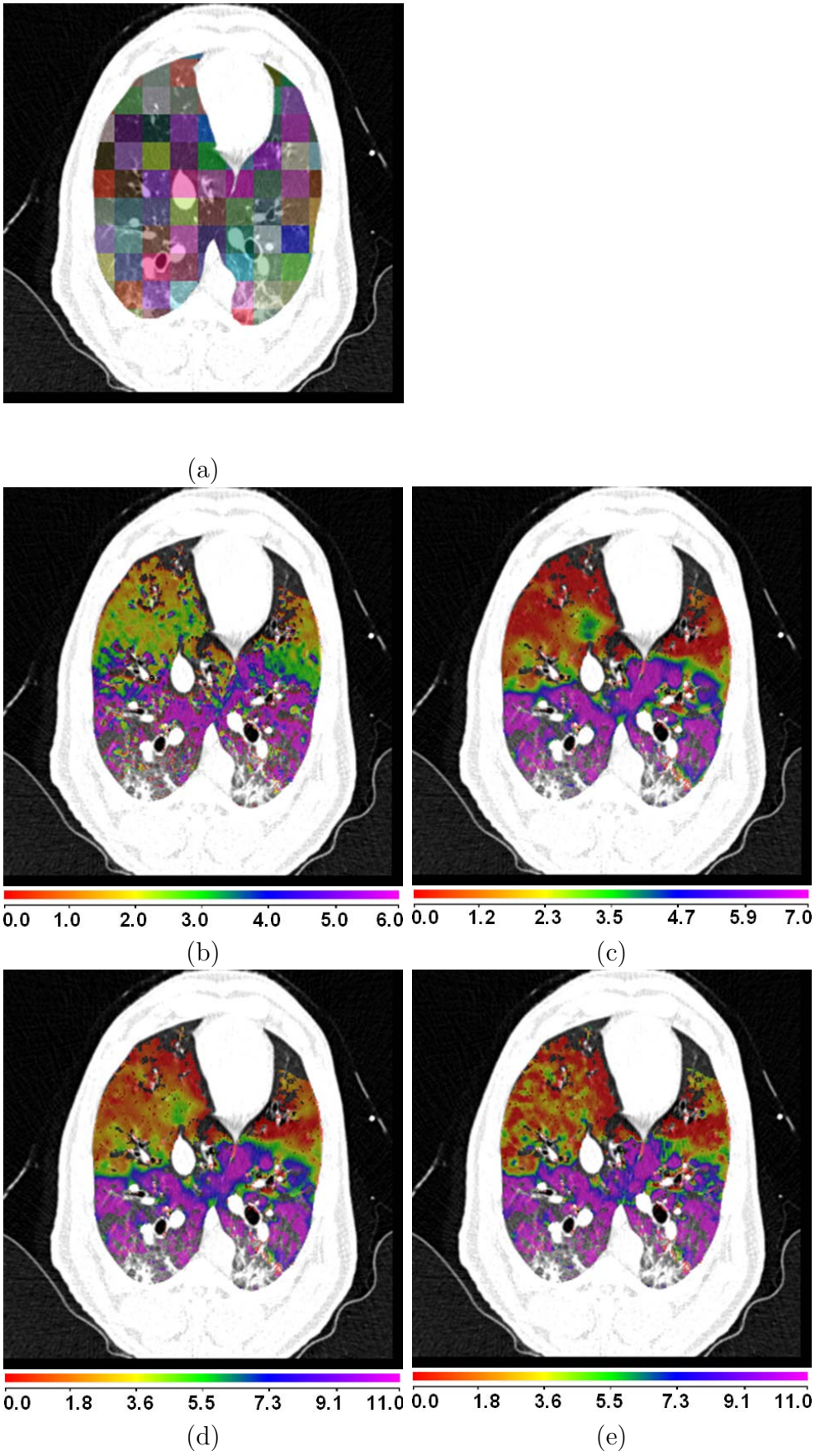

Figure 5.8: Comparison of the regional ventilation measures. (a): EE with color coded cubes showing the sample region. (b), (c), (d) and (e): color map of the SV, SAJ, SACJ and SAI.

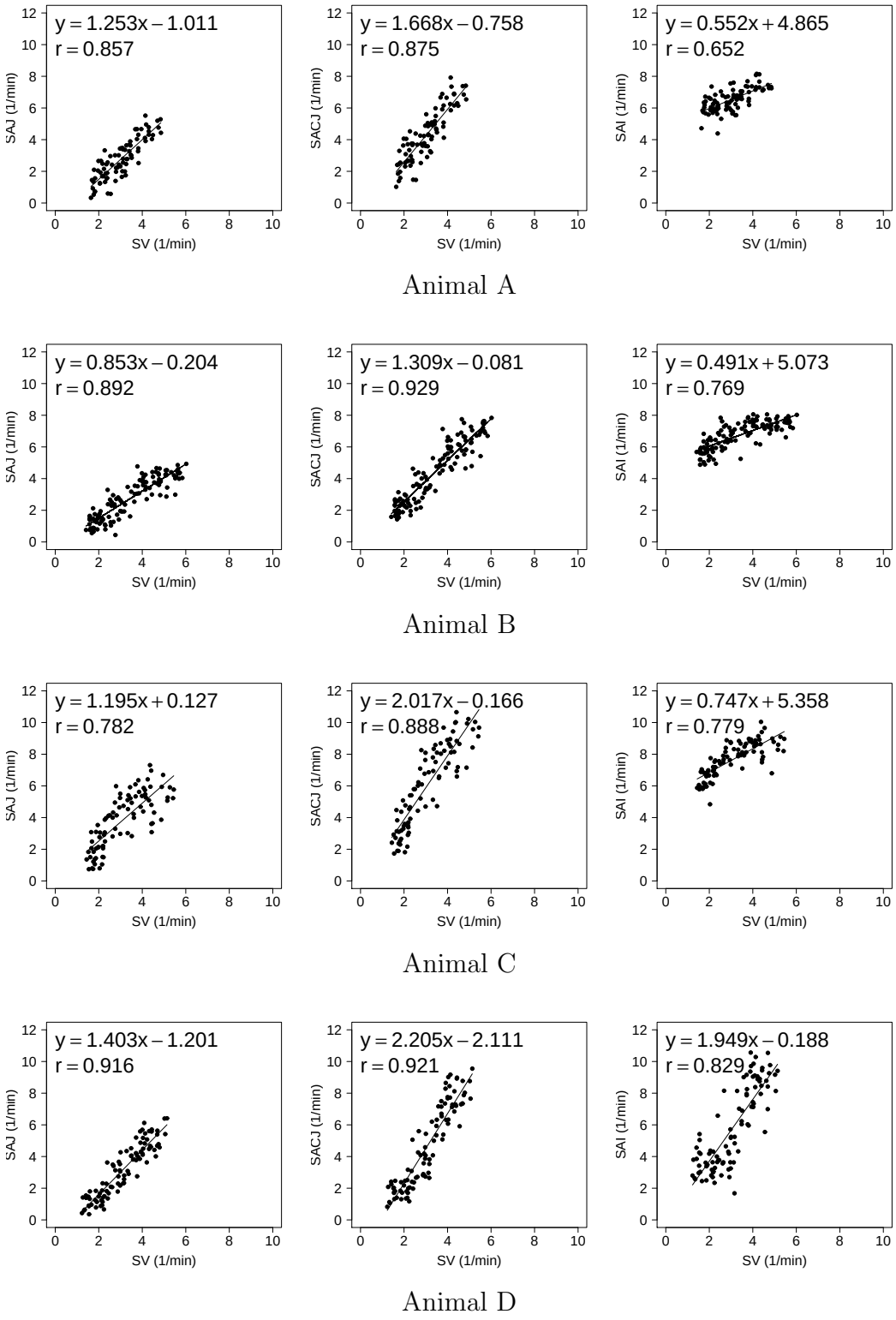

Figure 5.9: Small cube ROIs with size 20 mm × 20 mm × 20 mm results for registration estimated ventilation measures compared to the Xe-CT estimated ventilation SV in scatter plot with linear regression in four animals. The first column is the SAJ vs. SV. The second column is the SACJ vs. SV. The third column is the SAI vs. SV.

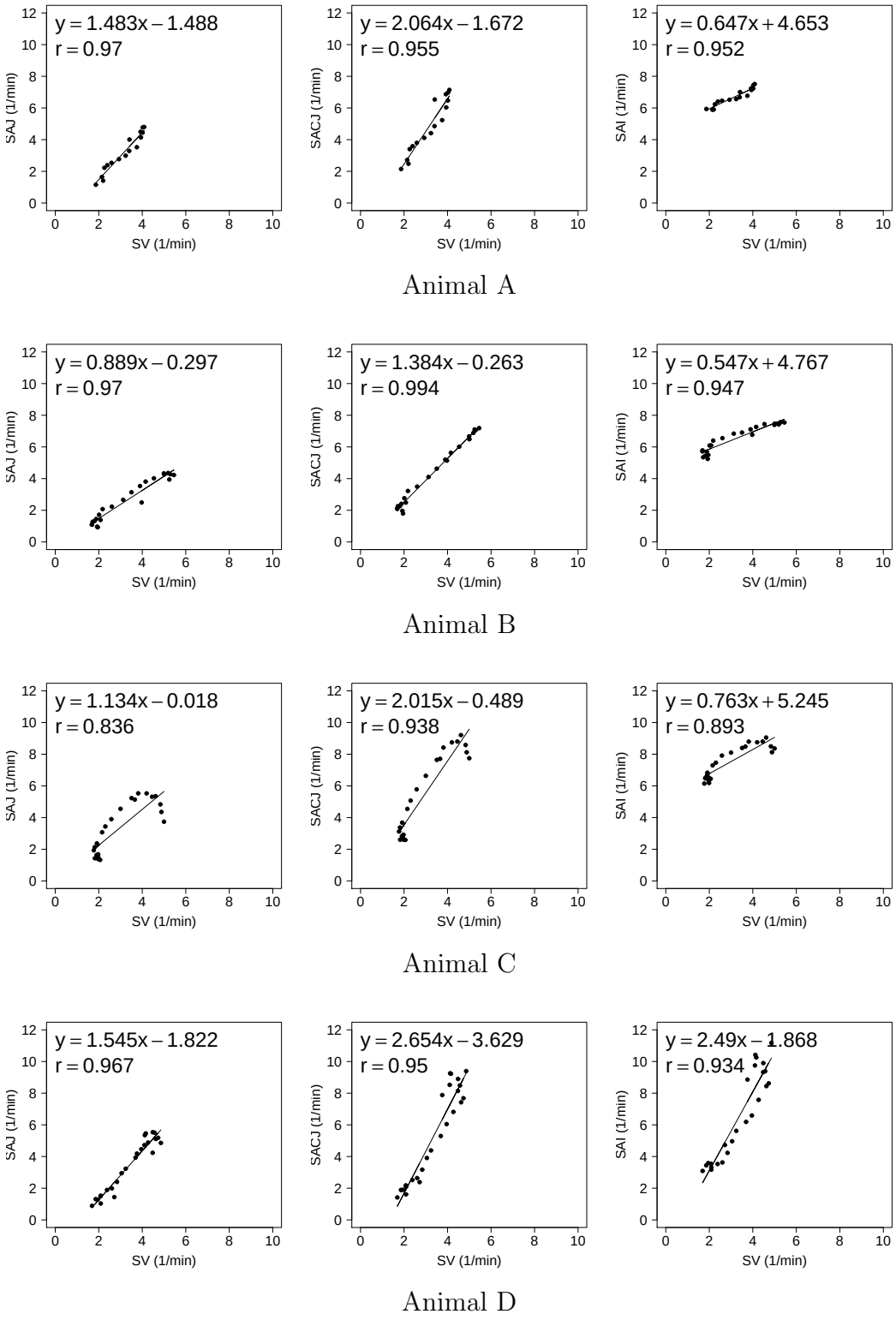

Figure 5.10: Large slab ROIs with size 150 mm × 8 mm × 40 mm results for registration estimated ventilation measures compared to the Xe-CT estimated ventilation SV in scatter plot with linear regression in four animals. The first column is the SAJ vs. SV. The second column is the SACJ vs. SV. The third column is the SAI vs. SV.

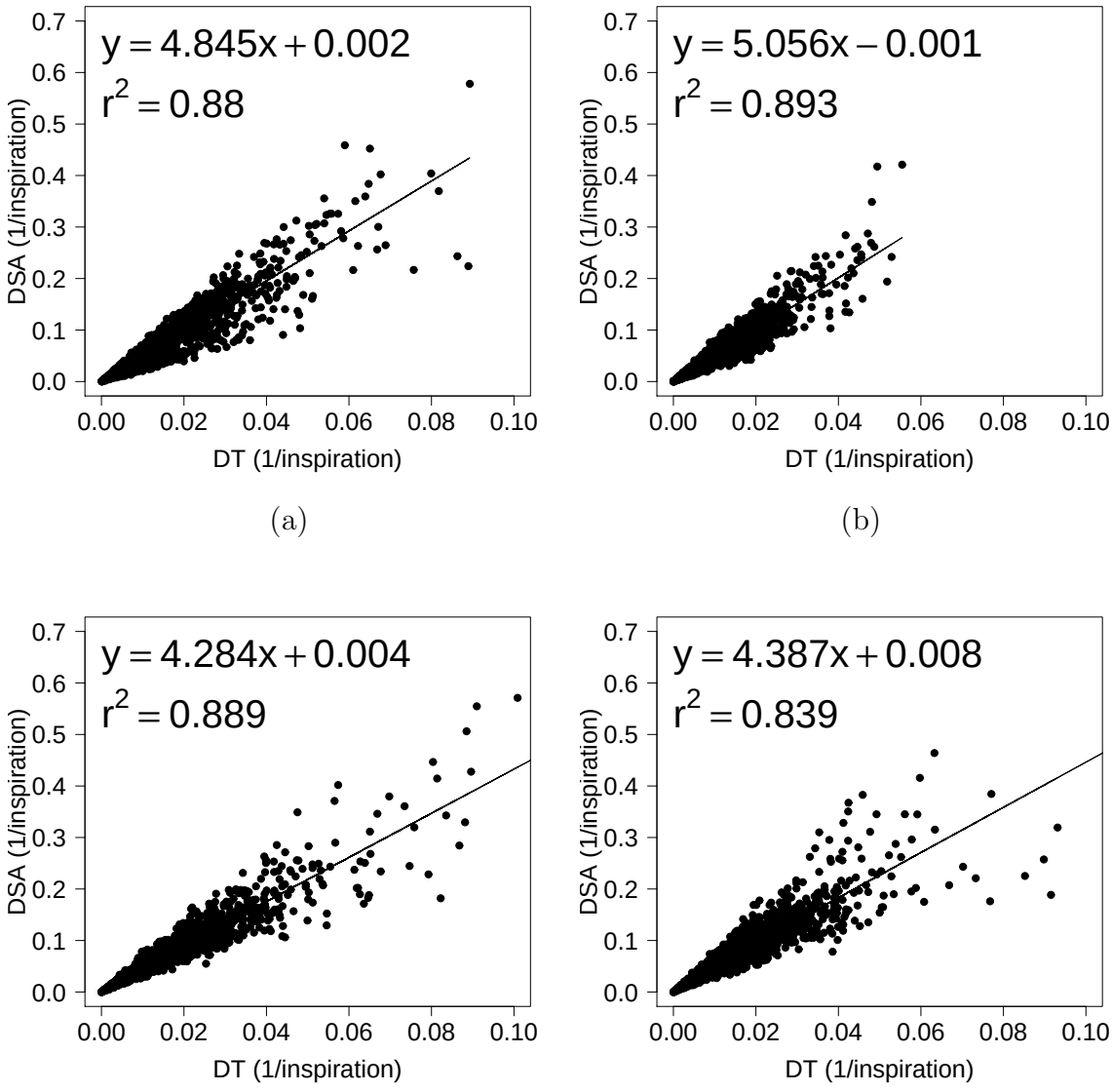

Figure 5.11: Linear regression analysis between DSA and DT. (a) to (d): DSA (the absolute difference of the value between the SACJ and SAI) compared to DT (the absolute difference of the tissue volume) in animals A, B, C and D.

Table 5.2: Comparison of ventilation measures between SAJ and SAI in small cube ROIs with size 20 mm × 20 mm × 20 mm.

Animal	Correlation pair (with SV)	Correlation with SV (r value)	Number of samples	p value
A	SAJ	0.86	83	p<= 0.001
	SAI	0.65		
B	SAJ	0.89	119	p<= 0.002
	SAI	0.77		
C	SAJ	0.78	86	p<= 1
	SAI	0.78		
D	SAJ	0.92	110	p<= 0.006
	SAI	0.83		

Table 5.3: Comparison of ventilation measures between SACJ and SAI in large slab ROIs with size 150 mm × 8 mm × 40 mm.

Animal	Correlation pair (with SV)	Correlation with SV (r value)	Number of samples	p value
A	SACJ	0.95	17	p<= 1
	SAI	0.95		
B	SACJ	0.99	23	p<= 0.01
	SAI	0.95		
C	SACJ	0.94	23	p<= 0.45
	SAI	0.89		
D	SACJ	0.95	25	p<= 0.56
	SAI	0.93		

comparison of different measures for estimates of regional ventilation are evaluated by Xe-CT estimated ventilation. Individual regional ventilation measure is compared to Xe-CT estimated ventilation by transforming them to the same coordinate system. The difference between two registration measures and its relationship with the tissue volume difference is analyzed using linear regression.

The tissue volume and vesselness preserving algorithm is used to register the EI to the EE for estimating ventilation measures. It is also used to register the EE_0

Table 5.4: Comparison of ventilation measures between SAJ and SAI in large slab ROIs with size 150 mm × 8 mm × 40 mm.

Animal	Correlation pair (with SV)	Correlation with SV (r value)	Number of samples	p value
A	SAJ	0.95	17	p<= 0.49
	SAI	0.95		
B	SAJ	0.99	23	p<= 0.41
	SAI	0.95		
C	SAJ	0.94	23	p<= 0.52
	SAI	0.89		
D	SAJ	0.95	25	p<= 0.15
	SAI	0.93		

to the EE for comparing three ventilation measures to the Xe-CT based SV. About 200 anatomical landmarks are identified and annotated to evaluate the registration accuracy. The average landmark error is on the order of 1 mm after registration.

The ventilation measures SAJ, SACJ and SAI are derived and the relationship between them is described. The SAJ which is linear to Jaocobian measures the regional ventilation based on the assumption that the composition of a volume in a voxel is totally air. The SACJ is the most general form in the three measures which is based on the voxel air-tissue fraction theory of HU. Finally, with further assumption about no change in the tissue volume between the corresponding voxels in the template and target images, SAI can be calculated. Compared to SACJ which explicitly combines information both from the Jacobian and the intensity, the SAJ only relies on the Jacobian of the the deformation and SAI only uses the intensity information. SACJ has the most basic form for regional ventilation measure directly from the HU based voxel air-tissue fraction.

The three registration-based ventilation measures as well as the SV from Xe-CT are averaged and compared in predefined cubes. Averaging and comparing by 20 mm $\times$ 20 mm $\times$ 20 mm ROIs, the SACJ shows significantly higher correlation with Xe-CT based SV than the SAI in all four animals. By studying the relationship between the DSA and DT, it is found that the difference between SACJ and SAI may be caused by the no tissue volume change assumption (5.18) used in SAI. As the derivation in equations (5.14) and (5.21), to use SAI, the tissue volume change should be approximately zero. From Fig. 5.11, it is shown that while the tissue volume difference is usually small (less than 5%), regional ventilation measure SAI with the zero tissue volume change may introduce difference of more than 10% unit volume per inspiration comparing with the SACJ measure. For the ventilation measured over a minute, the DSA is about more than 1.7 unit volume per voxel (average $RR = 17.59$ breaths/min). Table 5.1 and Table 5.2 show that the both the SACJ and SAJ have significantly better correlation with SV than the SAI. This is consistent with the findings by Kabus et al. [30] who show that the Jacobian based ventilation has less error than the intensity based ventilation analysis using the segmented total lung volume as a global comparison. Though all the regional ventilation measures and Xe-CT based SV from the linear regression analysis in Fig. 5.10 show high correlations, table 5.3 and table 5.4 show that there is no significant difference in the correlation with SV between the Jacobian based measures and intensity based measure. This result indicates that the validation methods using global comparison such as segmented total volume may not be able to distinguish the Jacobian based measure and the intensity

based measure.

The comparison of the ventilation measures has been limited to the resolution of 20 mm $\times$ 20 mm $\times$ ROIs. As the size of the ROIs decreases, the correlation between the ventilation measures with Xe-CT based SV decreases. This may be due to the underlying noise of the Xe-CT measurement of ventilation. Additional Xe-CT image analysis work including using multi-compartment models and inter-phase registration to improve SV measurement are required to reduce the noise in Xe-CT based SV measurement.

The image registration algorithm used to find the transformation from EI to EE for measurement of regional ventilation produces accurate registrations by minimizing the tissue volume and vesselness measure difference between the template image and the target image. It would be interesting to compare different image registration algorithms and their effects on the registration-based ventilation measures. For example, if two registration algorithms achieve the similar landmark accuracy, the one does not preserve tissue volume change may show even larger difference in the SACJ and SAI measures than the results using TVP as described above.

In conclusion, with the same deformation field by the same image registration algorithm, a significant difference between the Jacobian based ventilation measures and the intensity based ventilation measure is found in a regional level using Xe-CT based ventilation measure SV. The ventilation measure by corrected Jacobian SACJ gives best correlation with Xe-CT based SV and the correlation is significantly higher than from the ventilation by intensity SAI indicating the ventilation measure

by corrected Jacobian SACJ may be a better measure of regional lung ventilation from image registration of 4DCT images.

CHAPTER 6
CONCLUSION

In this chapter, we conclude the thesis and discuss some possible future improvements.

6.1 Summary of Results

In this thesis, we study regional lung mechanics and function using image registration in: estimation of pulmonary function in dynamic and static image sequences, evaluation of lobar biomechanics during respiration, measurement of pulmonary function changes following radiation therapy, and comparison of regional ventilation measures.

6.1.1 Estimation of Pulmonary Function in Dynamic and Static Image Sequences

A technique that uses multiple respiratory-gated CT images and non-rigid 3D image registration to make local estimates of lung tissue expansion is reported. The degree of regional lung expansion is measured using the Jacobian (a function of local partial derivatives) of the registration displacement field. We compare the ventral-dorsal patterns of lung expansion estimated in both retrospectively reconstructed dynamic scans and static breath-hold scans to a xenon CT based measure of specific ventilation and a semi-automatic reference standard in four anesthetized sheep studied in the supine orientation. The regional lung expansion estimated by 3D

image registration of images acquired at 50% and 75% phase points of the inspiratory portion of the respiratory cycle and 20 cm H_2O and 25 cm H_2O airway pressures gave the best match between the average Jacobian and the xenon CT specific ventilation respectively (linear regression, average $r^2 = 0.85$ and $r^2 = 0.84$).

6.1.2 Evaluation of Lobar Biomechanics During Respiration

It is hypothesized that the lobar surfaces slide against each other during respiration. We propose a method to evaluate the sliding motion of the lobar surfaces during respiration using lobe-by-lobe mass-preserving non-rigid image registration. We measure lobar sliding by evaluating the relative displacement on both sides of the fissure. The results show a superior-inferior gradient in the magnitude of lobar sliding. We compare whole-lung-based registration accuracy to lobe-by-lobe registration accuracy using vessel bifurcation landmarks. Both methods yield similar matching results in the center regions of the lobes while a considerable difference is observed in the vicinity of fissure.

6.1.3 Measurement of Pulmonary Function Changes Following Radiation Therapy

We propose a method that quantitatively measures the regional changes in lung tissue function following a course of radiation therapy by using 4DCT and image registration techniques. 4DCT data sets before and after RT from two subjects are used in this study. Nonlinear, 3D image registration is applied to register an image

acquired near end inspiration to an image acquired near end expiration to estimate the pulmonary function. The Jacobian of the image registration transformation, indicating local lung expansion or contraction, serves as an index of regional pulmonary function. Approximately 120 annotated vascular bifurcation points are used as landmarks to evaluate registration accuracy. We compare regional pulmonary function before and after RT with the planned radiation dose at different locations of the lung. In all registration pairs, the average landmark distances after registration are on the order of 1 mm. The pulmonary function change as indicated by the Jacobian change ranges from -0.15 to 0.1 in the contralateral lung and -0.22 to 0.23 in the ipsilateral lung for subject A, and ranges from -0.4 to 0.39 in the contralateral lung and -0.25 to 0.5 in the ipsilateral lung for subject B. Both of the subjects show larger range of the increase of the pulmonary function in the ipsilateral lung than the contralateral lung. For lung tissue regions receiving a radiation dose larger than 24 Gy, a decrease in pulmonary function was observed. For regions receiving radiation dose smaller than 24 Gy, either an increase or a decrease in pulmonary function was observed. The relationship between the pulmonary function change and the radiation dose varies at different locations. With the use of 4DCT and image registration techniques, the pulmonary function prior to and following a course of radiation therapy can be measured. In our preliminary application of this approach for two subjects, changes in pulmonary function were observed with a weak correlation between the dose and pulmonary function change. In certain sections of the lung, detected locally-compromised pulmonary function may have resulted from radiation injury.

6.1.4 Comparison of Regional Ventilation Measures

We compare three different 4DCT based registration derived measures of regional ventilation to xenon-CT (Xe-CT). 4DCT and Xe-CT data sets from four adult sheep are used in this study. Nonlinear, 3D image registration is applied to register an image acquired near end inspiration to an image acquired near end expiration. Three different registration-based measures of regional ventilation are derived and implemented. Individual regional ventilation measure is compared to Xe-CT estimated ventilation by transforming them to the same coordinate system using the resultant transformation from the same image registration applied to align the Xe-CT to the 4DCT. Approximately 200 annotated anatomical points are used as landmarks to evaluate registration accuracy. We compare the registration based measures of regional ventilation with Xe-CT based estimate of regional ventilation in predefined region of interests (ROIs) and study the relationship between their difference and tissue volume. After registration, the landmark error is on the order of 1 mm. For cubical ROIs in cubes with size 20 mm $\times$ 20 mm $\times$ 20 mm, the Jacobian based ventilation measures specific air volume change by specific volume change (SAJ) and specific air volume change by corrected Jacobian (SACJ) show significantly higher correlation (linear regression, average $r^2 = 0.75$ and $r^2 = 0.82$) with the Xe-CT-based measure of specific ventilation (SV) than the specific air volume change by intensity (SAI) (linear regression, average $r^2 = 0.58$). For ROIs in slabs along the ventral-dorsal direction with size of 150 mm $\times$ 8 mm $\times$ 40 mm, the SAJ, SACJ,

and SAI all show high correlation (linear regression, average $r^2 = 0.88$, $r^2 = 0.92$ and $r^2 = 0.87$) with the Xe-CT based SV without significant different between each other. Linear relationship between the difference of specific air volume change (DSA) and difference of tissue volume (DT) is found in all four animals (linear regression, average $r^2 = 0.86$). With the same deformation field by the same image registration algorithm, a significant difference between the Jacobian based ventilation measures and the intensity based ventilation measure is found in a regional level using Xe-CT based ventilation measure SV. The ventilation measure by corrected Jacobian SACJ gives best correlation with Xe-CT based SV and the correlation is significantly higher than from the ventilation by intensity SAI indicating the ventilation measure by corrected Jacobian SACJ is better than SAI as a measure of regional lung ventilation from image registration of 4DCT images.

6.2 Future Work

Here we point out some directions of our future research in studying regional lung function and mechanics.

6.2.1 Classification of the COPD Patients Using Mechanical Parameters

In our study of regional lung function and mechanics, we focused on development of image registration and biomechanics analysis methods. In the future works, we may put more efforts on applying our techniques to data sets from diseased subjects for clinical application.

Establishing the mechanical characteristics of lungs in both smokers and non-smokers from the COPDGene study which is the largest study ever to investigate the underlying genetic factors of COPD, will bring the field one step closer to clinical application. The COPD can be classified with 4 classes of severity using pulmonary function tests. Recently, Murphy et al. [116] applied the image registration of expiration scan to the inspiration scan with features calculation such as percentage of voxels below certain threshold and ventilation and successfully classified COPD subjects (COPD/non-COPD). The result from accurate registration of a pair of scans is a complex displacement field including all the spatial information of the tissue changes. Therefore, with voxel based displacement operator, regional characteristics of tissue changes can be extracted from the displacement filed. As described in Chapter 1, COPD is characterized by loss of elasticity (increased compliance) of the lung tissue, from destruction of structures supporting the alveoli and destruction of capillaries feeding the alveoli [12], so the mechanical changes should be characterized from the COPD patient with different severity. By using features of all the mechanical parameters introduced in previous chapters, the subjects may be classified with different severity regionally.

6.2.2 Sensitivity Analysis

Image registration is an ill-posed problem. Since the functional information is derived directly from the displacement fields, it seems imperative that the displacement field be correct and physiologically meaningful, in addition to assessing spatial registration accuracy. Kabus et al. [31] have recently shown that methods that seem

to have roughly the same mean landmark accuracy may produce very different Jacobian maps. It is our interest to assess the sensitivity of our technique for measuring regional lung mechanics to the registration error, image noise and the image artifacts., thus establishing method reproducibility and measurement confidence interval.

We consider introducing the perturbation to the displacement field and the intensity image with random noise. Of course this may result in inaccurate biomechanical measurement, but it may show the robustness and the detectable resolution of a intrinsic lung tissue function change from our technique.

6.2.3 Anisotropy

In previous chapters, the parameters we applied to measure regional lung mechanics and function are mainly volume changes (Jacobian, SV, SAJ, SACJ, and SAI). It would be interesting to detect the directional changes in the deformation, such as anisotropy. In Chapter 1, we introduce several anisotropy parameters, such as FA, ADI, SRI, ARI and VA. Those parameters can be used to measure the pulmonary function changes introduced by COPD or radiation therapy as discussed in Chapter 4. In this way, we will combine the magnitudinous mechanical parameters with the directional mechanical parameters to represent the regional strain characteristics.

REFERENCES

[1] National Cancer Institute, VisualsOnline. http://visualsonline.cancer.gov (accessed June 14, 2010)

[2] European Lung Foundation, ELF. http://www.european-lung-foundation.org (accessed June 14, 2010)

[3] Bainbridge College, Respiratory Lab. http://fsweb.bainbridge.edu/ (accessed June 14, 2010)

[4] Tapp Medical Clinic, Emphysema. http://www.tappmedical.com/emphysema.htm (accessed June 14, 2010)

[5] Webb, A.: Introduction to Biomedical Imaging. John Wiley and Sons, Inc., Hoboken, New Jersey (2003)

[6] Anaethesia, FRCA. http://www.frca.co.uk/ (accessed June 14, 2010)

[7] Ibanez, L., Schroeder, W., Ng, L., Cates, J.: The ITK Software Guide. Kitware, Inc (2005)

[8] Lubliner, J.: Plasticity Theory. Dover Publication, Mineola, NY (2008)

[9] Reinhardt, J.M., Ding, K., Cao, K., Christensen, G.E., Hoffman, E.A., Bodas, S.V.: Registration-based estimates of local lung tissue expansion compared to xenon CT measures of specific ventilation. Medical Image Analysis **12**(6) (2008) 752 – 763 Special issue on information processing in medical imaging 2007.

[10] Murphy, K., van Ginneken, B., Pluim, J., Klein, S., Staring, M.: Semi-automatic reference standard construction for quantitative evaluation of lung CT registration. In: Proc. of International Conference on Medical Image Computing and Computer-Assisted Intervention 2008. Volume 5242. (2008) 1006–1013

[11] Gray, H., Lewis, W.H.: Anatomy of the Human Body. Lea and Febiger, Philadelphia, Pennsylvania (1918)

[12] Pratt, P. In: Emphysema and chronic airways disease. Springer-Verlag (1998) 654–659 edited by D. Dail and S. Hammar.

[13] Hoffman, E.A., Behrenbeck, T., Chevalier, P.A., Wood, E.H.: Estimation of pleural surface expansile forces in intact dogs. **55**(3) (Sept. 1983) 935–948

[14] Hubmayr, R., Walters, B., Chevalier, P., Rodarte, J., Olson, L.: Topographical distribution of regional lung volume in anesthetized dogs. **54**(4) (1983) 1048–1056

[15] Robertson, H.T., Glenny, R.W., Stanford, D., McInnes, L.M., Luchtel, D.L., Covert, D.: High-resolution maps of regional ventilation utilizing inhaled fluorescent microspheres. **82**(3) (1997) 943–953

[16] Harris, R.S., Schuster, D.P.: Visualizing lung function with positron emission tomography. J Appl Physiol **102**(1) (2007) 448–458

[17] Venegas, J.G., Winkler, T., Musch, G., Melo, M.F.V., Layfield, D., Tgavalekos, N., Fischman, A.J., Callahan, R.J., Bellani, G., Harris, R.S.: Self-organized patchiness in asthma as a prelude to catastrophic shifts. Nature **7034**(2-3) (2005) 777–782

[18] Moller, H.E., Chen, X.J., Saam, B., Hagspiel, K.D., Johnson, G.A., Altes, T.A., de Lange, E.E., Kauczor, H.U.: MRI of the lungs using hyperpolarized noble gases. Magnetic Resonance in Medicine **47**(6) (2002) 1029–1051

[19] van Beek, E.J., Wild, J.M., Kauczor, H.U., Schreiber, W., III, J.P.M., de Lange, E.E.: Functional MRI of the lung using hyperpolarized 3-helium gas. Journal Of Magnetic Resonance Imaging **20**(4) (2004) 550–554

[20] Hoffman, E.A., van Beek, E.: Hyperpolarized media MR imaging - expanding the boundaries? Academic Radiology **13**(8) (2006) 929–931

[21] Marcucci, C., Nyhan, D., Simon, B.A.: Distribution of pulmonary ventilation using Xe-enhanced computed tomography in prone and supine dogs. J Appl Physiol **90**(2) (2001) 421–430

[22] Tajik, J.K., Chon, D., Won, C.H., Tran, B.Q., Hoffman, E.A.: Subsecond multisection CT of regional pulmonary ventilation. Academic Radiology **9** (2002) 130–146

[23] Chon, D., Simon, B.A., Beck, K.C., Shikata, H., Saba, O.I., Won, C., Hoffman, E.A.: Differences in regional wash-in and wash-out time constants for xenon-CT ventilation studies. Respiratory Physiology & Neurobiology **148**(1-2) (2005) 65 – 83

[24] Fuld, M.K., Easley, R.B., Saba, O.I., Chon, D., Reinhardt, J.M., Hoffman, E.A., Simon, B.A.: CT-measured regional specific volume change reflects regional ventilation in supine sheep. J Appl Physiol **104**(4) (2008) 1177–1184

[25] Guerrero, T., Sanders, K., Noyola-Martinez, J., Castillo, E., Zhang, Y., Tapia, R., Guerra, R., Borghero, Y., Komaki, R.: Quantification of regional ventilation from treatment planning CT. International Journal of Radiation Oncology*Biology*Physics **62**(3) (2005) 630 – 634

[26] Guerrero, T., Sanders, K., Castillo, E., Zhang, Y., Bidaut, L., Komaki, T.P.R.: Dynamic ventilation imaging from four-dimensional computed tomography. Phys Med Biol. **51**(4) (Feb. 21 2006) 777–791

[27] Gee, J., Sundaram, T., Hasegawa, I., Uematsu, H., Hatabu, H.: Characterization of regional pulmonary mechanics from serial magnetic resonance imaging data1. Academic Radiology **10**(10) (2003) 1147 – 1152

[28] Sundaram, T.A., Gee, J.C.: Towards a model of lung biomechanics: Pulmonary kinematics via registration of serial lung images. Medical Image Analysis **9**(6) (2005) 524–537

[29] Christensen, G.E., Song, J.H., Lu, W., Naqa, I.E., Low, D.A.: Tracking lung tissue motion and expansion/compression with inverse consistent image registration and spirometry. Med Physics **34**(6) (June 2007) 2155–2165

[30] Kabus, S., von Berg, J., Yamamoto, T., Opfer, R., Keall, P.J.: Lung ventilation estimation based on 4D-CT imaging. In: First International Workshop on Pulmonary Image Analysis, New York (2008) 73–81

[31] Kabus, S., Klinder, T., Murphy, K., van Ginneken, B., Lorenz, C., Pluim, J.P.W.: Evaluation of 4D-CT lung registration. In: MICCAI (1). (2009) 747–754

[32] Ehrhardt, J., Werner, R., Schmidt-Richberg, A., Handels, H.: A statistical shape and motion model for the prediction of respiratory lung motion. Volume 7623., SPIE (2010) 762353

[33] Wang, G., Yu, H., Man, B.D.: An outlook on x-ray CT research and development. Medical Physics **35**(3) (2008) 1051–1064

[34] Ritman, E., Kinsey, J., Robb, R., Gilbert, B., Harris, L., Wood, E.: Three-dimensional imaging of heart, lungs, and circulation. Science **210**(4467) (1980) 273–280

[35] Hoffman, E.A., Sinak, L.J., Robb, R.A., Ritman, E.L.: Noninvasive quantitative imaging of shape and volume of lungs. J Appl Physiol **54**(5) (1983) 1414–1421

[36] Hoffman, E.A., Chon, D.: Computed Tomography Studies of Lung Ventilation and Perfusion. Proc Am Thorac Soc **2**(6) (2005) 492–498

[37] Hoffman, E.A., Reinhardt, J.M., Sonka, M., Simon, B.A., Guo, J., Saba, O., Chon, D., Samrah, S., Shikata, H., Tschirren, J., Palagyi, K., Beck, K.C., McLennan, G.: Characterization of the interstitial lung diseases via density-based and texture-based analysis of computed tomography images of lung structure and function1. Academic Radiology **10**(10) (2003) 1104 – 1118

[38] Hoffman, E.A., Jiang, R., Baumhauer, H., Brooks, M.A., Carr, J.J., Detrano, R., Reinhardt, J., Rodriguez, J., Stukovsky, K., Wong, N.D., Barr, R.G.: Reproducibility and validity of lung density measures from cardiac CT scans–the multi-ethnic study of atherosclerosis MESA lung study1. Academic Radiology **16**(6) (2009) 689 – 699

[39] Saba, O.I., Chon, D., Beck, K., McLennan, G., Sieren, J., Reinhardt, J., Hoffman, E.A.: Static versus prospective gated non-breath hold volumetric mdct imaging of the lungs1. Academic Radiology **12**(11) (2005) 1371 – 1384

[40] Maintz, J., Viergever, M.: A survey of medical image registration. Medical Image Analysis **2**(1) (1998) 1–36

[41] Lester, H., Arridge, S.: A survey of hierarchical non-linear medical image registration. Medical Image Analysis **32**(1) (1999) 129–149

[42] Crum, W.R., Hartkens, T.: Non-rigid image registration: theory and practice. British Journal of Radiology **77**(S) (2004) 140–153

[43] Szeliski, R., Coughlan, J.: Spline-based image registration. Int. J. Comput. Vision **22**(3) (1997) 199–218

[44] Broit, C.: Optimal registration of deformed images. PhD thesis, Philadelphia, PA, USA (1981)

[45] Christensen, G.E.: Deformable Shape Models for Anatomy. PhD thesis, Department of Electrical Engineering, Sever Institute of Technology, Washington University, St. Louis, MO. 63130 (Aug. 1994)

[46] Ferrant, M., Warfield, S.K., Nabavi, A., Jolesz, F.A., Kikinis, R.: Registration of 3d intraoperative mr images of the brain using a finite element biomechanical model. In: MICCAI '00: Proceedings of the Third International Conference on Medical Image Computing and Computer-Assisted Intervention, London, UK, Springer-Verlag (2000) 19–28

[47] Rueckert, D., Sonoda, L., Hayes, C., Hill, D., Leach, M., Hawkes, D.: Non-rigid registration using free-form deformations: application to breast mr images. Medical Imaging, IEEE Transactions on **18**(8) (aug. 1999) 712 –721

[48] Thevenaz, P., Unser, M.: Spline pyramids for inter-modal image registration using mutual information. In: Proc. SPIE. Volume 3169. (1997) 236–247

[49] Mattes, D., Haynor, D., Vesselle, H., Lewellen, T., Eubank, W.: Pet-ct image registration in the chest using free-form deformations. IEEE Transactions on Medical Imaging **22**(1) (Jan. 2003) 120–128

[50] Yin, Y., Hoffman, E.A., Lin, C.L.: Local tissue-weight-based nonrigid registration of lung images with application to regional ventilation. Volume 7262., SPIE (2009) 72620C

[51] Gorbunova, V., Lo, P., Ashraf, H., Dirksen, A., Nielsen, M., de Bruijne, M.: Weight preserving image registration for monitoring disease progression in lung CT. In: MICCAI. Volume 5242. (2008) 863–870

[52] Yin, Y., Hoffman, E.A., Lin, C.L.: Mass preserving nonrigid registration of CT lung images using cubic B-spline. Medical Physics **36**(9) (2009) 4213–4222

[53] Cao, K., Christensen, G.E., Ding, K., Reinhardt, J.M.: Intensity-and-Landmark-Driven, Inverse Consistent, B-Spline Registration and Analysis for Lung Imagery. In Brown, M., de Bruijne, M., van Ginneken, B., Kiraly, A., Kuhnigk, J.M., Lorenz, C., McClelland, J.R., Mori, K., Reeves, A., Reinhardt, J.M., eds.: Second International Workshop on Pulmonary Image Analysis, London, UK (2009) 137

[54] Cao, K., Ding, K., Christensen, G.E., Raghavan, M.L., Amelon, R.E., Reinhardt, J.M.: Unifying Vascular Information in Intensity-Based Nonrigid Lung CT Registration. In , ed.: In Press, - (-) –

[55] Byrd, R.H., Lu, P., Nocedal, J., Zhu, C.: A limited memory algorithm for bound constrained optimization. SIAM J. Sci. Comput. **16**(5) (1995) 1190–1208

[56] Choi, Y., Lee, S.: Injectivity conditions of 2d and 3d uniform cubic b-spline functions. Graphical Models **62**(6) (2000) 411–427

[57] Li, B., Christensen, G.E., McLennan, G., Hoffman, E.A., Reinhardt, J.M.: Establishing a normative atlas of the human lung: Inter-subject warping and registration of volumetric CT. Acad. Radiol. **10**(3) (2003) 255

[58] Basser, P.J., Pierpaoli, C.: Microstructural and physiological features of tissues elucidated by quantitative-diffusion-tensor MRI. Journal of Magnetic Resonance, Series B **111**(3) (1996) 209 – 219

[59] Gough, J.: Discussion on the diagnosis of pulmonary emhysema. Proceedings of the Royal Society of Medicine **45**(9) (1952) 576–586

[60] Mishima, M., Hirai, T., Itoh, H., Nakano, Y., Sakai, H., Muro, S., Nishimura, K., Oku, Y., Chin, K., Ohi, M., Nakamura, T., Bates, J.H.T., Alencar, A.M., Suki, B.: Complexity of terminal airspace geometry assessed by lung computed tomography in normal subjects and patients with chronic obstructive pulmonary disease. Proceedings of the National Academy of Sciences of the United States of America **96**(16) (1999) 8829–8834

[61] Moser, K. In: Pulmonary thromboembolism. McGraw-Hill (1987) 1105–1111 edited by E. Braunwald and K.J. Isselbacher and R. G. Petersdorf.

[62] Kong, F.M., Haken, R.K.T., Schipper, M.J., Sullivan, M.A., Chen, M., Lopez, C., Kalemkerian, G.P., Hayman, J.A.: High-dose radiation improved local tumor control and overall survival in patients with inoperable/unresectable non-small-cell lung cancer: Long-term results of a radiation dose escalation study. International Journal of Radiation Oncology*Biology*Physics **63**(2) (2005) 324 – 333

[63] Yaremko, B.P., Guerrero, T.M., Noyola-Martinez, J., Guerra, R., Lege, D.G., Nguyen, L.T., Balter, P.A., Cox, J.D., Komaki, R.: Reduction of normal lung irradiation in locally advanced non-small-cell lung cancer patients, using ventilation images for functional avoidance. International Journal of Radiation Oncology*Biology*Physics **68**(2) (2007) 562 – 571

[64] Ding, K., Bayouth, J.E., Buatti, J.M., Christensen, G.E., Reinhardt, J.M.: 4DCT-based measurement of changes in pulmonary function following a course of radiation therapy. Medical Physics **37**(3) (2010) 1261–1272

[65] Won, C., Chon, D., Tajik, J., Tran, B.Q., Robinswood, G.B., Beck, K.C.,

Hoffman, E.A.: Ct-based assessment of regional pulmonary microvascular blood flow parameters. Journal of Applied Physiology **94**(6) (2003) 2483–2493

[66] Chon, D., Beck, K.C., Simon, B.A., Shikata, H., Saba, O.I., Hoffman, E.A.: Effect of low-xenon and krypton supplementation on signal/noise of regional CT-based ventilation measurements. **102** (2007) 1535–1544

[67] Christensen, G., Johnson, H.: Consistent image registration. IEEE Trans. Med. Imaging **20**(7) (2001) 568 – 582

[68] Amit, Y.: A non-linear variational problem for image matching. SIAM Journal on Scientific Computation **15**(1) (January 1994) 207–224

[69] Johnson, H.J.: Method for consistent linear-elastic medical image registration. Master's thesis, Department of Electrical and Computer Engineering, The University of Iowa, Iowa City, IA 52242 (May 2000)

[70] Johnson, H., Christensen, G.: Consistent landmark and intensity-based image registration. IEEE Trans. Med. Imaging **21**(5) (2002) 450–461

[71] Simon, B.A., Marcucci, C.: Parameter estimation and confidence intervals for Xe-CT ventilation studies: A Monte Carlo approach. JAP **84**(2) (1998) 709–716

[72] Hu, S., Hoffman, E.A., Reinhardt, J.M.: Automatic lung segmentation for accurate quantitation of volumetric X-ray CT images. IEEE Trans. Medical Imaging **20**(6) (2001) 490–498

[73] Urschler, M., Kluckner, S., Bischof, H.: A framework for comparison and evaluation of nonlinear intra-subject image registration algorithms. In: ISC/NA-MIC Workshop on Open Science at MICCAI 2007. (2007)

[74] Hubmayr, R.D., Rodarte, J.R., Walters, B.J., Tonelli, F.M.: Regional ventilation during spontaneous breathing and mechanical ventilation in dogs. J Appl Physiol **63**(6) (1987) 2467–2475

[75] Ukil, S., Reinhardt, J.M.: Anatomy-guided lung lobar surface detection in X-ray CT images. IEEE Trans. Medical Imaging **28**(2) (Feb. 2009) 202–214

[76] Tschirren, J., McLennan, G., Palágyi, K., Hoffman, E.A., Sonka, M.: Matching and anatomical labeling of human airway tree. **24**(12) (2005) 1540–1547

[77] Shikata, H., Hoffman, E.A., Sonka, M.: Automated segmentation of pulmonary vascular tree from 3D CT images. Volume 5369., SPIE (2004) 107–116

[78] Hoffman, E.A., Ritman, E.L.: Effect of body orientation on regional lung expansion in dog and sloth. J Appl Physiol **59**(2) (1985) 481–491

[79] Cai, J., Sheng, K., Benedict, S.H., Read, P.W., Larner, J.M., III, J.P.M., de Lange, E.E., Jr., G.D.C., Miller, G.W.: Dynamic mri of grid-tagged hyperpolarized helium-3 for the assessment of lung motion during breathing. International Journal of Radiation Oncology*Biology*Physics **75**(1) (2009) 276 – 284

[80] Chang, J.Y., Balter, P.A., Dong, L., Yang, Q., Liao, Z., Jeter, M., Bucci, M.K., McAleer, M.F., Mehran, R.J., Roth, J.A., Komaki, R.: Stereotactic body radiation therapy in centrally and superiorly located stage I or isolated recurrent non-small-cell lung cancer. International Journal of Radiation Oncology*Biology*Physics **72**(4) (2008) 967 – 971

[81] Onimaru, R., Fujino, M., Yamazaki, K., Onodera, Y., Taguchi, H., Katoh, N., Hommura, F., Oizumi, S., Nishimura, M., Shirato, H.: Steep dose-response relationship for stage I non-small-cell lung cancer using hypofractionated high-dose irradiation by real-time tumor-tracking radiotherapy. International Journal of Radiation Oncology*Biology*Physics **70**(2) (2008) 374 – 381

[82] McCammon, R., Schefter, T.E., Gaspar, L.E., Zaemisch, R., Gravdahl, D., Kavanagh, B.: Observation of a dose-control relationship for lung and liver tumors after stereotactic body radiation therapy. International Journal of Radiation Oncology*Biology*Physics **73**(1) (2009) 112 – 118

[83] Xia, T., Li, H., Sun, Q., Wang, Y., Fan, N., Yu, Y., Li, P., Chang, J.Y.: Promising clinical outcome of stereotactic body radiation therapy for patients with inoperable stage I/II non-small-cell lung cancer. International Journal of Radiation Oncology*Biology*Physics **66**(1) (2006) 117 – 125

[84] Graham, M.V., Purdy, J.A., Emami, B., Harms, W., Bosch, W., Lockett, M.A., Perez, C.A.: Clinical dose-volume histogram analysis for pneumonitis after 3D treatment for non-small cell lung cancer (NSCLC). International Journal of Radiation Oncology*Biology*Physics **45**(2) (1999) 323 – 329

[85] Paiman, G., Marks, L.B., Vujaskovic, Z., Kelsey, C.R.: Radiation-induced lung injury. assessment, management, and prevention. Oncology (Williston Park, N.Y.) **22**(1) (2008) 37 – 47

[86] Hernando, M.L., Marks, L.B., Bentel, G.C., Zhou, S.M., Hollis, D., Das, S.K., Fan, M., Munley, M.T., Shafman, T.D., Anscher, M.S., Lind, P.A.: Radiation-induced pulmonary toxicity: A dose-volume histogram analysis in 201 patients with lung cancer. International Journal of Radiation Oncology*Biology*Physics **51**(3) (2001) 650 – 659

[87] Kwa, S.L., Lebesque, J.V., Theuws, J.C., Marks, L.B., Munley, M.T., Bentel, G., Oetzel, D., Spahn, U., Graham, M.V., Drzymala, R.E., Purdy, J.A., Lichter, A.S., Martel, M.K., Haken, R.K.T.: Radiation pneumonitis as a function of mean lung dose: An analysis of pooled data of 540 patients. International Journal of Radiation Oncology*Biology*Physics **42**(1) (1998) 1 – 9

[88] Tsoutsou, P.G., Koukourakis, M.I.: Radiation pneumonitis and fibrosis: Mechanisms underlying its pathogenesis and implications for future research. International Journal of Radiation Oncology*Biology*Physics **66**(5) (2006) 1281 – 1293

[89] Seppenwoolde, Y., Lebesque, J.V., de Jaeger, K., Belderbos, J.A., Boersma, L.J., Schilstra, C., Henning, G.T., Hayman, J.A., Martel, M.K., Haken, R.K.T.: Comparing different NTCP models that predict the incidence of radiation pneumonitis. International Journal of Radiation Oncology*Biology*Physics **55**(3) (2003) 724 – 735

[90] Mehta, V.: Radiation pneumonitis and pulmonary fibrosis in non-small-cell lung cancer: Pulmonary function, prediction, and prevention. International Journal of Radiation Oncology*Biology*Physics **63**(1) (2005) 5 – 24

[91] Yorke, E.D., Jackson, A., Rosenzweig, K.E., Merrick, S.A., Gabrys, D., Venkatraman, E.S., Burman, C.M., Leibel, S.A., Ling, C.C.: Dose-volume factors contributing to the incidence of radiation pneumonitis in non-small-cell lung cancer patients treated with three-dimensional conformal radiation therapy. International Journal of Radiation Oncology*Biology*Physics **54**(2) (2002) 329 – 339

[92] Chapet, O., Fraass, B.A., Haken, R.K.T.: Multiple fields may offer better esophagus sparing without increased probability of lung toxicity in optimized imrt of lung tumors. International Journal of Radiation Oncology*Biology*Physics **65**(1) (2006) 255 – 265

[93] McGuire, S.M., Zhou, S., Marks, L.B., Dewhirst, M., Yin, F.F., Das, S.K.: A methodology for using SPECT to reduce intensity-modulated radiation therapy (IMRT) dose to functioning lung. International Journal of Radiation Oncology*Biology*Physics **66**(5) (2006) 1543 – 1552

[94] Ng, Q.S., Goh, V., Milner, J., Padhani, A.R., Saunders, M.I., Hoskin, P.J.: Acute tumor vascular effects following fractionated radiotherapy in human lung cancer: In vivo whole tumor assessment using volumetric perfusion computed tomography. International Journal of Radiation Oncology*Biology*Physics **67**(2) (2007) 417 – 424

[95] van Luijk, P., Novakova-Jiresova, A., Faber, H., Steneker, M.N., Kampinga, H.H., Meertens, H., Coppes, R.P.: Relation between radiation-induced whole lung functional loss and regional structural changes in partial irradiated rat lung. International Journal of Radiation Oncology*Biology*Physics **64**(5) (2006) 1495 – 1502

[96] van Luijk, P., Faber, H., Meertens, H., Schippers, J.M., Langendijk, J.A., Brandenburg, S., Kampinga, H.H., Coppes, R.P.: The impact of heart irradiation on dose-volume effects in the rat lung. International Journal of Radiation Oncology*Biology*Physics **69**(2) (2007) 552 – 559

[97] Novakova-Jiresova, A., van Luijk, P., van Goor, H., Kampinga, H.H., Coppes, R.P.: Changes in expression of injury after irradiation of increasing volumes in rat lung. International Journal of Radiation Oncology*Biology*Physics **67**(5) (2007) 1510 – 1518

[98] Semenenko, V.A., Molthen, R.C., Li, C., Morrow, N.V., Li, R., Ghosh, S.N., Medhora, M.M., Li, X.A.: Irradiation of varying volumes of rat lung to same mean lung dose: A little to a lot or a lot to a little? International Journal of Radiation Oncology*Biology*Physics **71**(3) (2008) 838 – 847

[99] Suga, K.: Technical and analytical advances in pulmonary ventilation SPECT with xenon-133 gas and tc-99m-technegas. Annals of Nuclear Medicine **16**(5) (2002) 303 – 310

[100] Ding, K., Cao, K., Christensen, G.E., Hoffman, E.A., Reinhardt, J.M.: Registration-based regional lung mechanical analysis: Retrospectively reconstructed dynamic imaging versus static breath-hold image acquisition. Volume 7262., SPIE (2009) 72620D

[101] Staring, M., Klein, S., Pluim, J.P.W.: A rigidity penalty term for nonrigid registration. Medical Physics **34**(11) (2007) 4098–4108

[102] Waldron, T., Bayouth, J., Bhatia, S., Buatti, J.: Use of music-based breathing training to stabilize breathing motion in respiration correlated imaging and radiation delivery. International Journal of Radiation Oncology*Biology*Physics **72**(1, Supplement 1) (2008) S659 – S659

[103] Keall, P.J., Kini, V.R., Vedam, S.S., Mohan, R.: Potential radiotherapy improvements with respiratory gating. Australasian physical & engineering sciences in medicine **25**(1) (2002) 1 – 6

[104] Low, D.A., Nystrom, M., Kalinin, E., Parikh, P., Dempsey, J.F., Bradley, J.D., Mutic, S., Wahab, S.H., Islam, T., Christensen, G., Politte, D.G., Whiting, B.R.: A method for the reconstruction of four-dimensional synchronized CT scans acquired during free breathing. Medical Physics **30**(6) (2003) 1254–1263

[105] Pan, T.: Comparison of helical and cine acquisitions for 4D-CT imaging with multislice ct. Medical Physics **32**(2) (2005) 627–634

[106] Ding, K., Cao, K., Christensen, G.E., Raghavan, M.L., Hoffman, E.A., Reinhardt, J.M.: Registration-based lung tissue mechanics assessment during tidal breathing. In Brown, M., de Bruijne, M., van Ginneken, B., Kiraly, A., Kuhnigk, J.M., Lorenz, C., Mori, K., Reinhardt, J.M., eds.: First International Workshop on Pulmonary Image Analysis, New York (2008) 63

[107] Ding, K., Yin, Y., Cao, K., Christensen, G.E., Lin, C.L., Hoffman, E.A., Reinhardt, J.M.: Evaluation of lobar biomechanics during respiration using image registration. In: Proc. of International Conference on Medical Image Computing and Computer-Assisted Intervention 2009. Volume 5761. (2009) 739–746

[108] Guo, J., Fuld, M.K., Alford, S.K., Reinhardt, J.M., Hoffman, E.A.: Pulmonary analysis software suite 9.0: Integrating quantitative measures of function with structural analyses. In: First International Workshop on Pulmonary Image Analysis, New York (2008) 283–292

[109] Yin, Y., Choi, J., Hoffman, E.A., Tawhai, M.H., Lin, C.L.: Simulation of pulmonary air flow with a subject-specific boundary condition. Journal of Biomechanics (2010) in press.

[110] Cao, K., Ding, K., Christensen, G.E., Reinhardt, J.M.: Tissue volume and vesselness measure preserving nonrigid registration of lung ct images. Volume 7623., SPIE (2010) 762309

[111] Frangi, A.F., Niessen, W.J., Vincken, K.L., Viergever, M.A.: Multiscale vessel enhancement filtering. In: MICCAI. Volume 1496. (1998) 130–137

[112] Shikata, H., McLennan, G., Hoffman, E.A., Sonka, M.: Segmentation of pulmonary vascular trees from thoracic 3d ct images. International Journal of Biomedical Imaging **2009**(1) 36240

[113] Joshi, V., Reinhardt, J.M., Abramoff, M.D.: Automated measurement of retinal blood vessel tortuosity. In Karssemeijer, N., Summers, R.M., eds.: Proc. SPIE Conf. Medical Imaging. Volume 7624. (2010) 76243

[114] Simon, B.A.: Non-invasive imaging of regional lung function using X-Ray computed tomography. Journal of Clinical Monitoring and Computing **16**(5) (2000) 433 – 442

[115] Papoulis, A., ed.: Probability and Statistics. Prentence Hall, Englewood Cliffs, NJ (1990)

[116] Murphy, K., van Ginneken, B., van Rikxoort, E., de Hooop, B., Prokop, M., Lo, P., de Bruijne, M., Pluim, J.: Obstructive pulmonary function: Patient classification using 3D registration of inspiration and expiration CT images. (2009) 37–47